Doctoral Dissertation

博士論文

Chiral cyanido-bridged Mn–Nb magnets composed of achiral building blocks and their non-linear optical effect

(アキラルな構築素子から成るキラルなシアノ架橋型 Mn–Nb 磁性体及びその非線形光学効果)

A Dissertation Submitted for the Degree of Doctor of Philosophy

December 2019

令和元年 12 月博士(理学)申請

Department of Chemistry, Graduate School of Science,

The University of Tokyo

東京大学理学系研究科化学専攻

Ohno Takuro

大野 拓郎

Abstract

1. Introduction

Molecule-based magnets are good candidates for functional magnets because their functionalities can be designed by selecting appropriate components from a large number of building blocks such as metal cations and organic ligands. Compounds which show both chirality and long range magnetic ordering are called chiral magnets. Chiral magnets attract strong attention as functional magnets because they exhibit a cross linking effect between optical and magnetic properties, such as magnetization induced second harmonic generation. There is a considerable number of reports of chiral molecule-based magnets by introducing enantiopure building blocks. However, reports of chiral magnets composed of achiral building blocks by the spontaneous chiral resolution are relatively rare. In 2014, our laboratory reported a chiral photomagnet synthesized from achiral building blocks, $[Fe(4\text{-bromopyridine})_4]_2[Nb(CN)_8]\cdot 2H_2O$. I studied analogues of this compound to obtain new chiral magnets. In my master course study, I prepared metal substituted compounds, $[M(4\text{-bromopyridine})_4]_2[Nb(CN)_8]\cdot nH_2O$ (M = Mn, Ni, Zn), and analyzed their crystal structures and magnetic properties. In this work, I will report the synthetic method, crystal structure, magnetic properties and second harmonic generation (SHG) phenomena of octacyanidoniobate-based metal assemblies synthesized from achiral building blocks, namely, $[Mn(4\text{-iodopyridine})_4]_2[Nb(CN)_8]$ (**MnNbIpy**), $[Mn(4\text{-bromopyridine})_4]_2[Nb(CN)_8]\cdot 0.5H_2O$ (**MnNbBrpy**), and $[Mn(4\text{-chloropyridine})_4]_2[Nb(CN)_8]\cdot 0.5H_2O$ (**MnNbClpy**). All three compounds show ferrimagnetism. **MnNbIpy** and **MnNbBrpy**, which have chiral structures, show SHG phenomena.

2. Materials

The powder samples of target compounds were synthesized by reacting aqueous solutions of $K_4[Nb(CN)_8]\cdot 2H_2O$ to mixed water–ethanol or aqueous solutions of 4-halopyridine, manganese chloride, and sodium L-ascorbate. Crystalline samples were prepared by using the slow diffusion method. Spectroscopic studies revealed that **MnNbIpy**,

MnNbBrpy, and **MnNbClpy** contain 4-halopyridine ligands and that the Mn ions are divalent. Elemental analysis show that formulae are $[Mn(4\text{-iodopyridine})_4]_2[Nb(CN)_8]$ (for **MnNbIpy**), $[Mn(4\text{-bromopyridine})_4]_2[Nb(CN)_8]\cdot 0.5H_2O$ (for **MnNbBrpy**), and $[Mn(4\text{-chloropyridine})_4]_2[Nb(CN)_8]\cdot 0.5H_2O$ (for **MnNbClpy**).

Single crystal X-ray structural analysis showed that **MnNbIpy** has a chiral tetragonal structure ($a = b = 20.8730(7)$ Å, $c = 14.2157(4)$ Å) with a space group $I4_1$ and **MnNbBrpy** also has a chiral tetragonal structure ($a = b = 20.6168(12)$ Å, $c = 14.0220(4)$ Å) with a space group $I4_122$. This space group $I4_122$ is one of the supergroup of the space group $I4_1$. On the other hand, **MnNbClpy** shows an achiral orthorhombic structure ($a = 13.9379(3)$ Å, $b = 26.6853(5)$ Å, $c = 31.5931(6)$ Å) with a space group *Fddd*.

MnNbIpy, **MnNbBrpy**, and **MnNbClpy** have similar coordination geometries. The Mn^{2+} ions adopt distorted octahedral geometries where four equatorial 4-halopyridine and two axial cyanido N atoms are coordinated and the Nb^{4+} ions adopt distorted square antiprism geometries, where eight cyanido C atoms are coordinated. Among the eight cyanido ligands coordinated to one Nb^{4+} ion, four are bridging ligands to Mn^{2+} ions and the other four are terminal ligands. These compounds show three-dimensional (3-D) cyanido-bridged coordination networks. One Nb^{4+} ion connects to four Nb^{4+} ions via –CN–Mn–NC– moieties.

In these 3-D coordination networks, there are helical structures along the *c*-axis (for **MnNbIpy** and **MnNbBrpy**) or the *a*-axis (for **MnNbClpy**). There are two types of helical structures in **MnNbIpy** and **MnNbBrpy**, while only one type is founded in **MnNbClpy**. This differences in the two helical structures are the reasons for chiral structures of **MnNbIpy** and **MnNbBrpy**. There are halogen bondings along the direction of the coordination helices between the halogen atom of the 4-halopyridine ligands and the N atom of the terminal cyanido ligands. Halogen bonding in **MnNbIpy** and **MnNbBrpy** is stronger than that of **MnNbClpy**. In **MnNbIpy** and **MnNbBrpy**, the coordination geometries around the Mn^{2+} ions are distorted by halogen bonding, forming the two types of helical structures that lead to the chiral structure.

3. Magnetic Properties

Magnetic measurements were conducted on the powder samples. The product ($\chi_M T$) of magnetic susceptibility (χ_M) and temperature (T) vs temperature (T) plots ($\chi_M T$–T plots) show that the $\chi_M T$ values at room temperature are 8.7 $K \cdot cm^3 \cdot mol^{-1}$ (for **MnNbIpy**), 8.4 $K \cdot cm^3 \cdot mol^{-1}$ (for **MnNbBrpy**), and 8.5 $K \cdot cm^3 \cdot mol^{-1}$ (for **MnNbClpy**). These values are similar to the calculated spin only $\chi_M T$ value (9.1 $K \cdot cm^3 \cdot mol^{-1}$) assuming two Mn^{2+} (S = 5/2) and one Nb^{4+} (S = 1/2) ions per formula. The field cooled magnetization curves revealed that these three compounds show long range magnetic ordering with the Curie temperatures (T_C) of 22 K, 28 K, and 28 K for **MnNbIpy**, **MnNbBrpy**, and **MnNbClpy**, respectively. Magnetic property measurements show that these three compounds are ferrimagnetic. Magnetization vs. external magnetic field plots show that the saturation magnetization values are close to 9 μ_B for all three compounds, which is the calculated value assuming ferrimagnetism with a $\{Mn^{II}_2Nb^{IV}_1\}$ unit per formula. Therefore, these compounds are ferrimagnetic, where the magnetic moments of Mn^{2+} and Nb^{4+} ions order antiparallelly under the T_C.

4. Second Harmonic Generation Measurement

SHG measurements for **MnNbIpy** and **MnNbBrpy** were conducted because these compounds have chiral structures. The form of SH susceptibility tensors from point group of **MnNbIpy** and **MnNbBrpy** are depicted below.

$$\chi = \begin{pmatrix} 0 & 0 & 0 & \chi_{14} & \chi_{15} & 0 \\ 0 & 0 & 0 & \chi_{15} & -\chi_{14} & 0 \\ \chi_{31} & \chi_{31} & \chi_{33} & 0 & 0 & 0 \end{pmatrix} \quad \text{(for } \mathbf{MnNbIpy}\text{)}$$

$$\chi = \begin{pmatrix} 0 & 0 & 0 & \chi_{14} & 0 & 0 \\ 0 & 0 & 0 & 0 & -\chi_{14} & 0 \\ 0 & 0 & 0 & 0 & 0 & 0 \end{pmatrix} \quad \text{(for } \mathbf{MnNbBrpy}\text{)}$$

A 775 nm laser light, derived from a frequency doubled Ti:sapphire laser passed through filters, was focused and irradiated on the samples. The reflected light was passed through filters to remove the fundamental light and focused into a photomultiplier tube equipped with a band pass filter. The power of the 775 nm irradiated laser light was altered by changing neutral density filters. The observed light is monochromatic at 388 nm, and represent

quadratic function of the power of the fundamental light well. These characteristics show the observed lights are SH light. **MnNbIpy** shows stronger SH light than that of **MnNbBrpy**, probably due to the difference of the number of non-zero elements of the SH susceptibility tensor resulting from the space group difference.

5. Conclusion

I synthesized three cyanido-bridged magnetic materials from achiral building blocks. **MnNbIpy** and **MnNbBrpy** are chiral compounds and **MnNbClpy** is an achiral compound. These three compounds have three dimensional coordination networks and similar coordination geometries. Magnetic property measurements revealed that these three compounds are ferrimagnetic where magnetic moments on Mn^{II} and Nb^{IV} order antiparallelly and the T_C values are 22 K, 28 K, and 28 K for **MnNbIpy**, **MnNbBrpy**, and **MnNbClpy**, respectively. Additionally, thanks to the chiral structures, **MnNbIpy** and **MnNbBrpy** exhibit SHG phenomena. The results suggest that halogen bondings are worth considering as fine tuning to make a chiral structure in molecule-based magnets.

Contents

Chapter 1: Introduction

1.1 Molecule-Based Magnet

Magnetic materials based on metals, alloys, metal oxides, or metal salts are well known for a long time. Recently molecule-based magnets, which are composed of metal ions, organic ligands, and/or organic radicals, attract strong attentions. Magnetisms of molecule-based magnets are derived from spins of unpaired electrons on metal ions or organic radicals. There are several types of molecule-based magnets such as magnets in which paramagnetic metal ions are coordinated by organic ligands or all organic magnets based on organic radicals. In molecule-based magnets, building blocks are assembled by coordination bonding, hydrogen bonding, and/or van der Waals force.

In 1967, H. H. Wickman et al.[1] reported a molecule based magnet, $[Fe^{III}$(N,N-dimethyldithiocarbamato)$_2]$Cl which shows the Curie temperature (T_C) of 2.5 K. This is an early example of molecule-based magnets based on metal complex (Figure. 1-1a). About organic ferromagnet, Kinoshita et al.[2] reported γ-phase of p-nitrophenylnironylnitroxide which show T_C of 0.65 K in 1991 (Figure. 1-1b).

Magnets showing functionality in addition to magnetism are interesting as functional magnets. Molecule-based magnets are good candidates for functional magnets because they have good designability of functionality from their large number of choice of building blocks. This is because number of organic ligands and metal ions are large, additionally organic ligands can be changed to new functional ligands by chemical modifications.

1.2 Cyanido-Bridged Metal Assemblies

Metal assemblies in which metal ions are bridged by cyanido ligands (CN^-) are called cyanido-bridged metal assemblies (*M*–CN–*M*'). Most of cyanido-bridged metal assemblies consist of polycyanidometalate ions ($[M^{m+}(CN)_n]^{-n+m}$) and other metal ions (*M*') which are coordinated by N atoms of cyanido ligands. In polycyanidometalate ions, C atoms of cyanido ions are coordinated to metal ions (*M*). Some of cyanido-bridged metal assemblies consist of

polycyanidometalate with blocking ligands ($[M^{m+}(L)(CN)_n]^{-l}$) where a metal ion is coordinated by cyanido ligands and other organic ligands like 2,2'-bipyridine.[3,4]

Cyanido-bridged metal assemblies attract attentions as a kind of molecule-based magnets. There are various choices of cyanidometalate ions, such as $[M^{m+}(CN)_4]$, $[M^{m+}(CN)_6]$, $[M^{m+}(CN)_7]$, and $[M^{m+}(CN)_8]$ (Figure 1-2). Some of cyanidometalate ions have paramagnetic metal centers. Additionally there are diverse choices of the other metal ions (*M*').

Cyanido-bridged metal assemblies are extensively studied as functional magnets. Various organic ligands can be introduced to the cyanido-bridged metal assemblies resulting in structural variety and flexibility. Cyanido-bridging provides strong magnetic superexchange interaction between spins on a magnetic metal center and the adjacent magnetic metal center bridged by cyanido ligand because cyanido ligands are small and have diffuse molecular orbital. Because distances between second nearest neighbor magnetic metal centers are long enough (~ 10 Å), the magnetic interaction between second nearest neighbor magnetic metal centers are small and negligible. Thus the calculation of the magnetic model of the cyanido-bridged metal assemblies becomes simple.[5,6]

Prussian blue ($Fe^{III}_4[Fe^{II}(CN)_6]_3 \cdot zH_2O$) is the earliest example of cyanido-bridged metal assemblies. Prussian blue has cubic and face-centered crystal structure where iron ions are bridged by cyanido ligands. Prussian blue has been studied as a magnetic material since 1950s and Prussian blue was revealed to a be ferromagnet.[7]

Metal substituted compounds of Prussian blue ($AM_{1x}[M_2(CN)_6]_y \cdot nH_2O$, $M_{1x}[M_2(CN)_6]_y \cdot nH_2O$, Figure 1-3)[43] are called Prussian blue analogues (PBA). There are numerous reports of PBAs as functional magnets, such as absorption materials of Cs ion or gases,[8–14] magnets with T_C values higher than room temperature,[15–22] compounds showing second harmonic generation (SHG) phenomena or magnetization-induced SHG (MSHG),[23–29] compounds with two or more compensation temperature,[30] a ferroelectric ferromagnet,[31] a magnet exhibiting a humidity-induced magnetization,[32] photomagnets based on charge transfer or spincrossover,[33–41] and a proton conducting magnet.[42]

Among cyanidometalates mentioned above, octacyanidometalates ($[M^{m+}(CN)_8]$: M = Mo, W, Nb, Re; m = 4, 5) are intensively studied as building blocks. Octacyanidometalates are expected to show strong magnetic superexchange interaction because metal centers of them, which are 4d or 5d metal ions, have diffuse d orbitals and because they have many magnetic superexchange pathways from their high coordination number. Therefore, cyanido-bridged metal assemblies based on octacyanidometalates are expected to show high T_C values. In addition, they are expected to show various structures, because octacyanidometalate ions have some coordination geometries (i.e. dodecahedron (D_{2d}), square antiprism (D_{4d}), and bicapped trigonal prism (C_{2v}), Figure 1-2) with similar energies.[152]

There are many reports of molecule-based magnets based on $[Mo^{IV/V}(CN)_8]$ or $[W^{IV/V}(CN)_8]$ but those of $[Nb^{IV}(CN)_8]$ are few because synthesis of $[Nb^{IV}(CN)_8]$ is relatively difficult[44,88,89] rather than that of $[Mo^{IV/V}(CN)_8]$/$[W^{IV/V}(CN)_8]$. Tetravalent Mo or W ions are d^2 transition metals and diamagnetic but tetravalent Nb ion is a d^1 transition metal and paramagnetic. Because metal substituted congeners of octacyanidometalate based compounds often show similar structures, Nb^{IV} congeners of Mo^{IV} or W^{IV} compounds tend to have similar structures but show different magnetic properties.

Cyanido-bridged metal assemblies using the octacyanidometalates have been synthesized[74] with various dimensionalities of the coordination networks,[45–54,88] resulting in luminescent magnets,[55–59] photomagnets,[61–64] porous magnets,[65,66] magnets with high thermal durability,[67,68] and single chain magnets or single molecule magnets which show the slow magnetic relaxation[69–73] (Figure 1-4). In octacyanidoniobate-based magnets, temperature- or pressure-induced iron (II) spin-crossover compounds,[75–77] photomagnets,[78–80] a humidity responsible magnet,[81] a magnet showing ion-conductivity,[82] a chiral magnet,[83] and magnets showing MSHG effects[84–87] have been reported (Figure 1-5).

In 2014, Ohkoshi et al.[90] reported an octacyanidoniobate-based chiral photomagnet, $[Fe^{II}(4\text{-bromopyridine})_4]_2[Nb^{IV}(CN)_8]\cdot 2H_2O$ (Figure 1-6). Although this compound was synthesized from achiral building blocks, this compound has a chiral structure and showing

SHG and MSHG effects. This compound shows iron(II) spin crossover phenomenon and becomes low-spin state in low temperature. Additionally, this compound exhibits photomagnetism with light induced excited spin-state trapping and its reverse effect, and therefore has two light induced states. Structural symmetries of the light induced states are different. Because of this symmetry difference, the polarization plane of MSHG lights were altered by light excitation.

1.3 Chiral Magnet

Compounds which cannot superimpose their mirror images are called chiral compounds. Chiral compounds are optically active and they rotate the polarization plane of a light. Crystals of chiral compounds don't have inversion center as symmetry operation. In chiral compounds except for compounds belonging to a point group 432, a polar tensor with odd rank describing the chiral compounds' physical properties have non-zero elements. This fact enables chiral compounds to show unique properties, which are not observed in most of achiral compounds. Among them, second order non-linear optical activities are famous. Second order non-linear optical activities are second harmonic generation, sum frequency generation, etc.

Magnetic materials possessing chirality are called chiral magnets. Chiral magnets attract attentions as functional magnets because they show cross linking effects of magnetic properties and properties unique to chiral compounds such as magnetization induced SHG, magneto-chiral dichroism,[91,92] and magneto-chiral birefringence[93–95] (Figure 1-7).

There are mainly two methods to synthesize chiral magnets. One is introduction of the chiral ligands or counter ions to molecule-based magnets.[96–104] Many chiral magnets made by this synthetic approach have been reported. On the other hand, reports of chiral molecule-based magnets synthesized only from achiral building blocks are relatively rare.[84–87,105–108]

1.4 Non-Linear Optical Effect

Assuming the Lorentz model, when a light is irradiated to a compound, electrons of the compound are oscillated by the electric field of the light and a polarization is generated. Then

the polarization generates a new light and this light interacts with the initial light. Generally, this process is linear and the polarization and the electric field of the initial light show the same frequency. However, when a strong light is irradiated to a compound, the compound can show a polarization with different frequency and generate a light with different frequency. This effect is called the non-linear optical effect.

To make a discussion easier, response speeds of materials to electric fields are ignored (in actual materials, they cannot be ignored). When an electric field of a light (E) is applied to a material (for simplicity, this material is an insulator), an induced electric dipole moment P of the material is expressed as a function of E like below.

$$P_i = \varepsilon_0 \chi^{(1)}_{ij} E_j + \varepsilon_0 \chi^{(2)}_{ijk} E_j E_k + \varepsilon_0 \chi^{(3)}_{ijkl} E_j E_k E_l + \cdots \quad (1\text{-}1)$$

In this eq 1-1, $ijk\ldots$ means Cartesian coordinates xyz, $\chi^{(n)}$ (n: integer) means the n-th order susceptibility tensor of the material. $\chi^{(n)}$ is polar tensor of rank $(n + 1)$ because P and E are polar tensor of rank 1. When the electric field E is weak, the second term and higher terms can be ignored. When the electric field E is strong, phenomena derived from second and higher terms appears. These terms are sources of non-linear optical effects.

Assuming the electric field of the light E oscillates with a frequency ω, P can be calculated by eq 1-1. When the electric field E is weak, only first term is considered and P oscillates with the same frequency ω. Because P generates electric field E, this is linear response to light. When the electric field E is strong, phenomena derived from second and higher terms appears. These components of P have different frequency to ω and these terms are the origin of non-linear optical activities.

As non-linear optical effects, second harmonic generation, which will be discussed in the next section, is famous. Also third order non-linear effect, non-linear Raman scattering, or X-ray generation from high-order ($n \approx$ dozens) harmonic generation from infrared light are known.[109–111]

Phenomena derived from the second term of above eq 1-1, $\varepsilon_0 \chi^{(2)}_{ijk} E_j E_k$, are called second order non-linear optical effects. This effect is composed of second harmonic generation (SHG),

sum frequency generation, difference frequency generation, and so on. Second order non-linear optical effect is used to laser wavelength conversion by optical parametric amplifier or optical parametric oscillator and generation of white light.

Second order non-linear optical effect only appears in surface, interface, or chiral materials and is prohibited in materials with the center of inversion symmetry because $\chi^{(2)}$ is property tensor and polar tensor of rank 3 (odd). With a property and polar tensor of rank n, $d_{ij\cdots m}$, and a symmetry operation l of a material, the relation between the tensors d and the tensor d after the symmetry operation l are applied is depicted like below because of Neuman principle.

$$d_{ij\cdots m} = l_{ii'}l_{jj'}\cdots l_{mm'}d_{i'j'\cdots m'} \tag{1-2}$$

Assuming the symmetry operation l is inversion, this becomes

$$d_{ij\cdots m} = (-1)^n d_{ij\cdots m} \tag{1-3}$$

If n is odd, then this becomes

$$d_{ij\cdots m} = -d_{ij\cdots m}$$

$$d_{ij\cdots m} = 0 \tag{1-4}$$

When this is applied to $\chi^{(2)}$, this means that in materials with the inversion symmetry, $\chi^{(2)}$ becomes 0 and that only in non-centrosymmetric compound, surface or interface, $\chi^{(2)}$ becomes non zero.

Because there is no influence from substituting j and k in second term of eq 1-1, $\chi^{(2)}_{ijk}$ and $\chi^{(2)}_{ikj}$ have same value ($\chi^{(2)}_{ijk} = \chi^{(2)}_{ikj}$). Therefore $\chi^{(2)}_{ijk}$ have 18 independent component not 27.

Second harmonic generation is a phenomenon where a half wavelength light is emitted when a strong light is irradiated to non-centrosymmetric materials. SHG was first observed in 1961 by using laser as strong light source.[112] SHG are applied to wavelength conversion of laser, surface observation, and interface observation.

1.5 Magneto-Optical Effect

When a light passed through a magnetic material, the magnetic property of the material affect the optical property of the light. This effect is called magneto-optical effect. The Faraday

effect which means the rotation of the polarized plane in the magnetic material or the magneto-optical Kerr effect are well known as examples of the magneto-optical effect.

When a SHG effect is observed in a magnetic material, optical properties of SHG lights are influenced by magnetization. This effect is called magnetization induced SHG (MSHG). MSHG effect was first observed by Aktsipetrov on 1990 at a surface of $Y_{2.5}Bi_{0.5}Fe_5O_{12}$ (which is centrosymmetric compound in bulk) thin film.[113] Then MSHG was observed on surface of iron.[114] In chromium(III) oxide which is antiferromagnetic material, MSHG effect is observed below Néel temperature because the symmetry is lowered with magnetic ordering.[115] In the early stage, MSHG effects were observed as change of polarization plane of SHG light by magnetic field (NOMOKE: nonlinear magneto-optical Kerr effect)[113,114,116] and later MSHG effects in surface of magnetic materials have been observed.[117,118]

MSHG effect is applied to interface observations, magnetic domain observations, or observations of magnetic ordering of antiferromagnetic materials.[119–122]

1.6 Objective of This Work

As mentioned above, materials showing non-linear optical and non-linear magneto-optical effects are important for developing laser systems and measurement techniques. Design of noncentrosymmetric magnets is a fundamental task leading to new non-linear magneto-optical materials.

In this work, I synthesized new cyanido-bridged bimetal assemblies $[Mn^{II}(\textit{4-halopyridine})_4]_2[Nb^{IV}(CN)_8]\cdot n H_2O$ (**MnNbIpy**: *4-halopyridine* = 4-iodopyridine, n = 0; **MnNbBrpy**: *4-halopyridine* = 4-bromopyridine, n = 0.5 ;**MnNbClpy**: *4-halopyridine* = 4-chloropyridine, n = 0.5) from achiral building blocks, i.e., octacyanidoniobate (IV) ion, 3d transition metal ions, and 4-halopyridines. **MnNbIpy** and **MnNbBrpy** have chiral structures, and the **MnNbClpy** has an achiral structure. I discussed magnetic properties of them, and observed second harmonic generation phenomena.

(a)

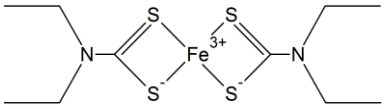

(b)

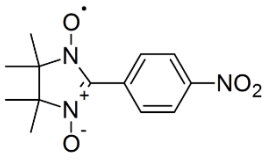

Figure 1-1. Structural formula of molecule-based magnets in the early period: (a) $[Fe^{III}(N,N\text{-dimethyldithiocarbamato})_2]Cl$,[1] (b) p-nitrophenylnironylnitroxide.[2]

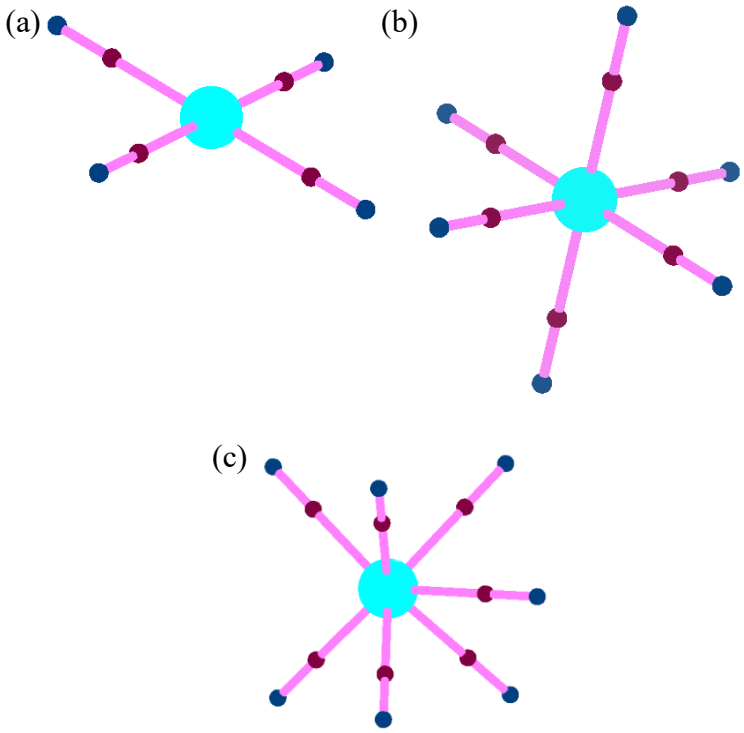

Figure 1-2. Examples of building blocks of cyanido bridged metal assemblies: (a) tetracyanidometalate, (b) hexacyanidometalate, and (c) heptacyanidometalate.

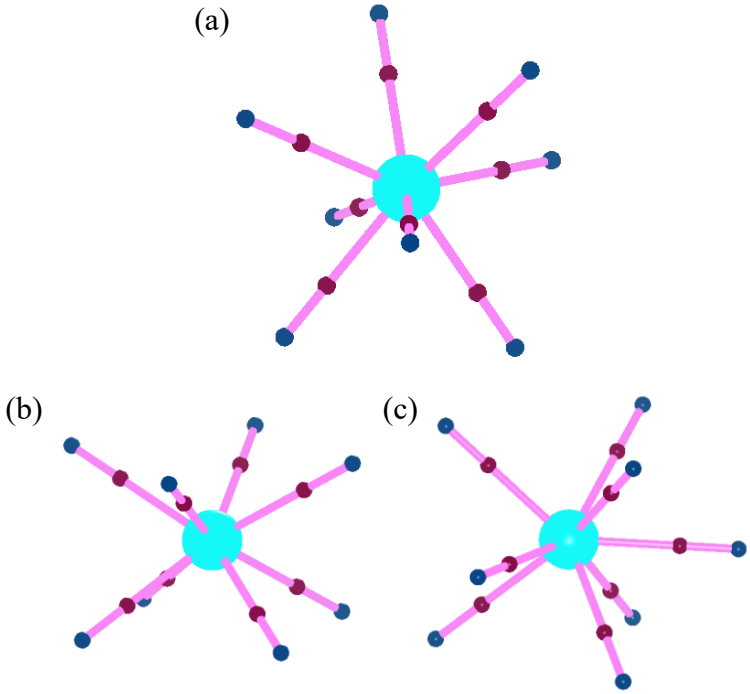

Figure 1-3. Examples of coordination geometries of octacyanidometalate: (a) dodecahedron antiprism geometry, (b) square antiprism geometry, and (c) bicapped trigonal prism geometry.

(a)

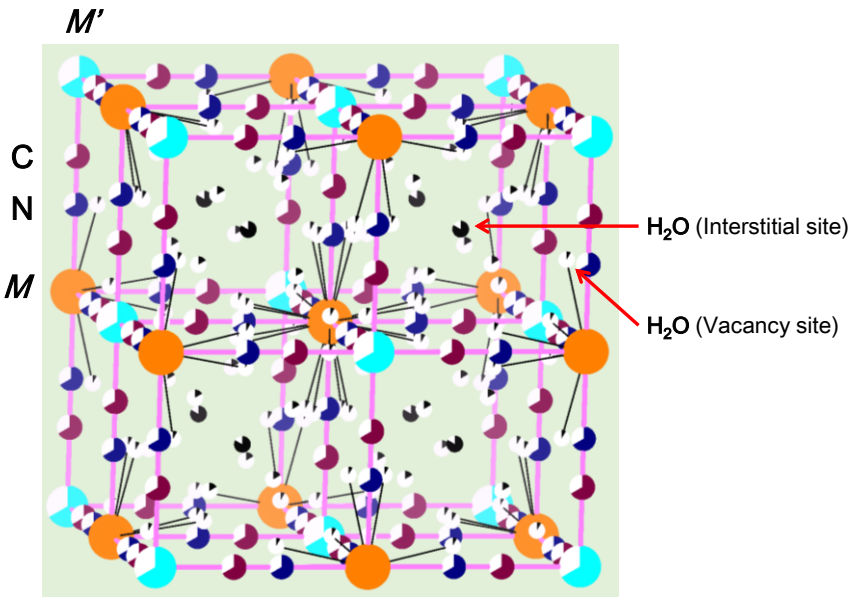

(b)

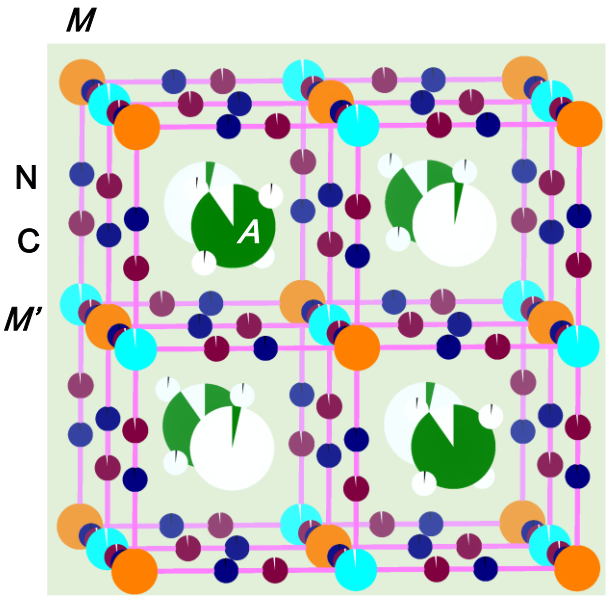

Figure 1-4. Crystal Structures of Prussian blue analogues. (a) $M'[M(CN)_6]_{2/3}\cdot zH_2O$,[43] (b) $A_xM'[M(CN)_6]_{(x+2)/3}\cdot zH_2O$.[25]

(a) Reproduced with permission of the International Union of Crystallography.

(b) Adapted with permission from S. Ohkoshi, S. Saito, T. Matsuda, T. Nuida, H. Tokoro, *J. Phys. Chem. C*, 2008, **112**, 13095. Copyright 2008 American Chemical Society.

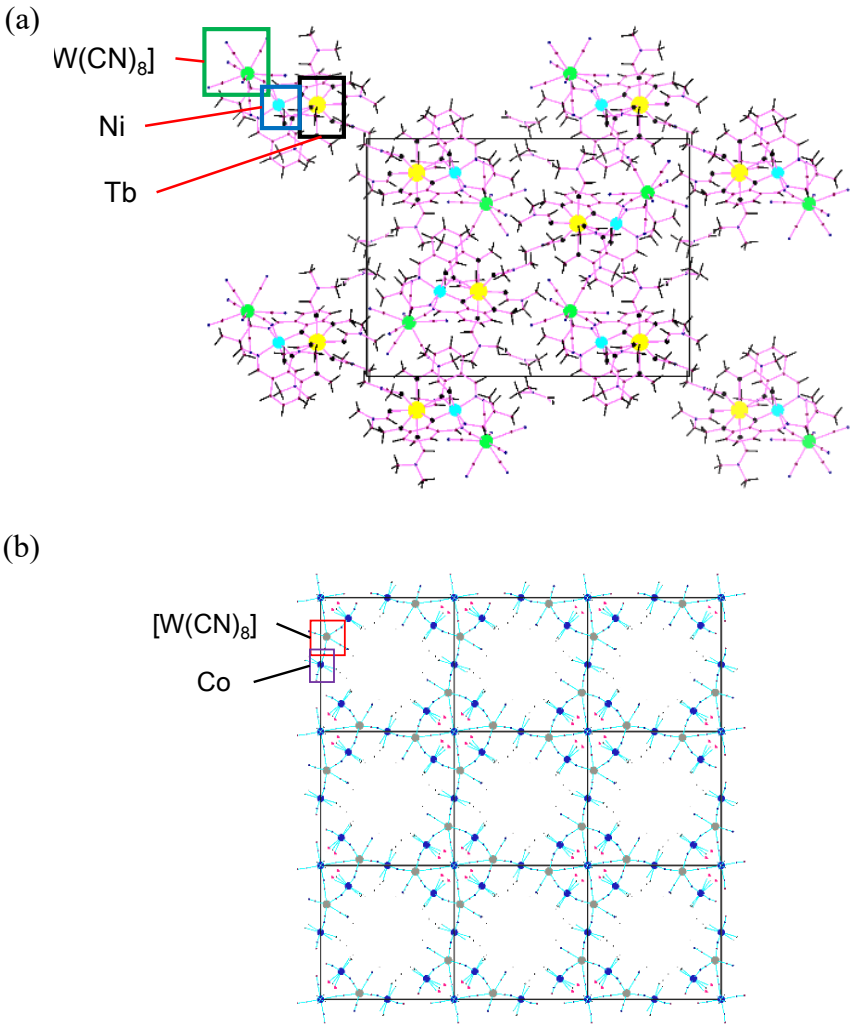

Figure 1-5. Examples of octacyanidometalate-based assemblies. (a) .a single molecule magnet $[L^{Me2}Ni(dmf)Tb(dmf)_4\{W(CN)_8\}]\cdot H2O$,[72] and (b) a porous magnet $Co_7[W(CN)_8]Cl_2\cdot 29H_2O$.[66]

(a) Adapted with permission from J.-P. Sutter, S. Dhers, R. Rajamani, S. Ramasesha, J.-P. Costes, C. Duhayon, L. Vendier, *Inorg. Chem.*, 2009, **48**, 5820. Copyright (2009) American Chemical Society.

(b) Adapted with permission from K. Nakabayashi, S. Chorazy, M. Komine, Y. Miyamoto, D. Takahashi, B. Sieklucka, S. Ohkoshi, *Cryst. Growth Des.*, 2017, **17**, 9, 4511. Copyright (2017) American Chemical Society.

(a)

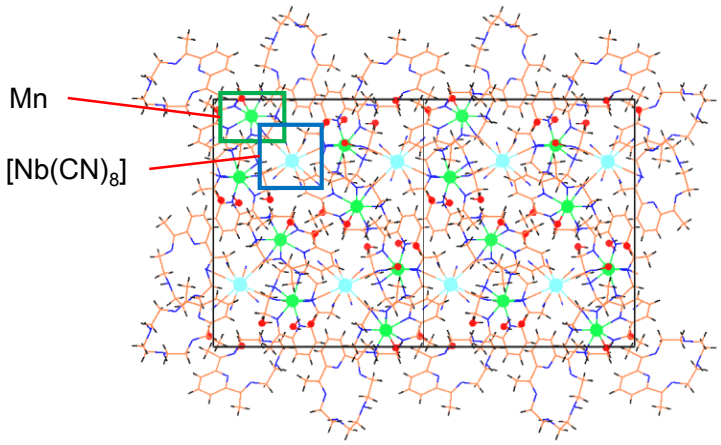

(b)

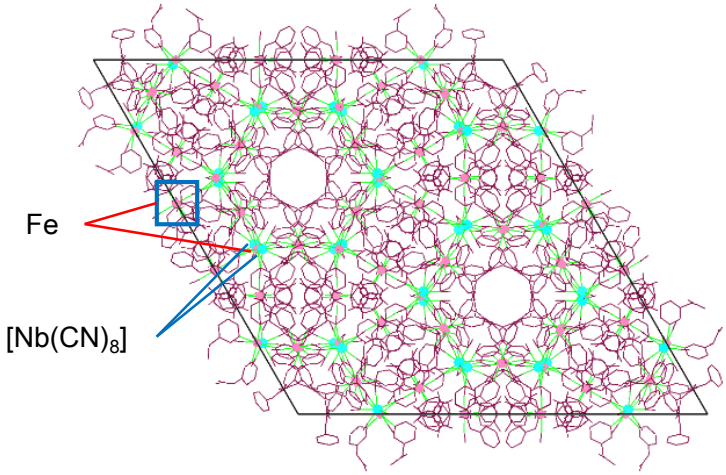

Figure 1-6. Examples of octacyanidoniobate-based molecule-based magnet. (a) a one-dimensional magnet $[MnL_1]_2[Nb(CN)_8]\cdot H_2O$,[89] and (b) a two steps spin-crossover compound $\{Fe^{II}_2(3\text{-}OAcpy)_5(3\text{-}OHpy)_3[Nb^{IV}(CN)_8]\}\cdot H_2O$.[76]

(a) Adapted with permission from R. Pradhan, C. Desplanches, P. Guionneau, J.-P. Sutter, *Inorg. Chem.*, 2003, **42**, 6607. Copyright (2003) American Chemical Society.

(b) Adapted with permission from S. Kawabata, S. Chorazy, J. J. Zakrzewski, K. Imoto, T. Fujimoto, K. Nakabayashi, J. Stanek, B. Sieklucka, S. Ohkoshi, *Inorg. Chem.*, 2019, **58**, 6052. Copyright (2019) American Chemical Society.

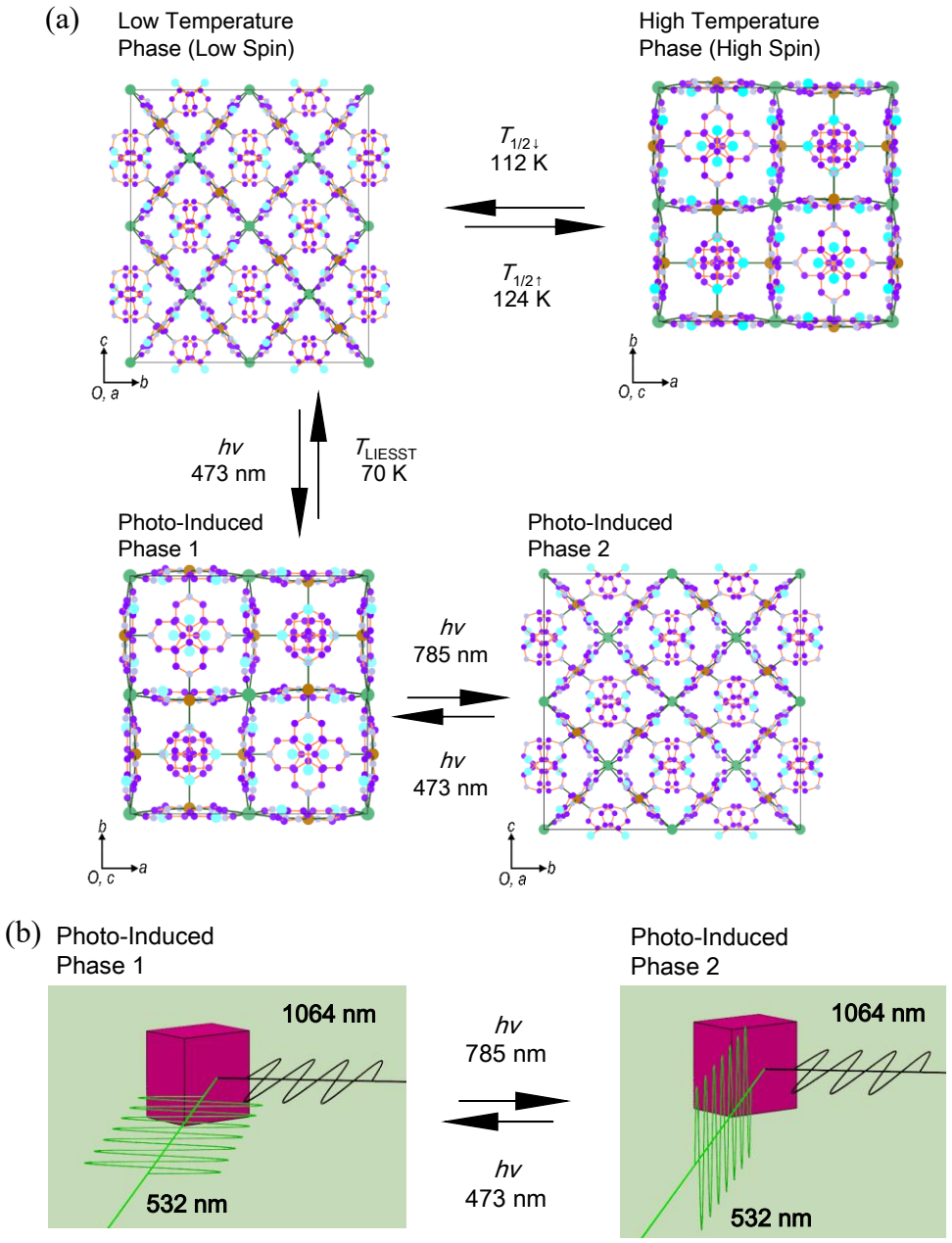

Figure 1-7. Visual description of chiral photomagnet, $[Fe^{II}(4\text{-bromopyridine})_4]_2[Nb^{IV}(CN)_8]\cdot 2H_2O$.[90] (a) Schematic illustrations of phase transitions. (b) Schematic illustrations of 90 degree optical switching MSHG light.

(a)

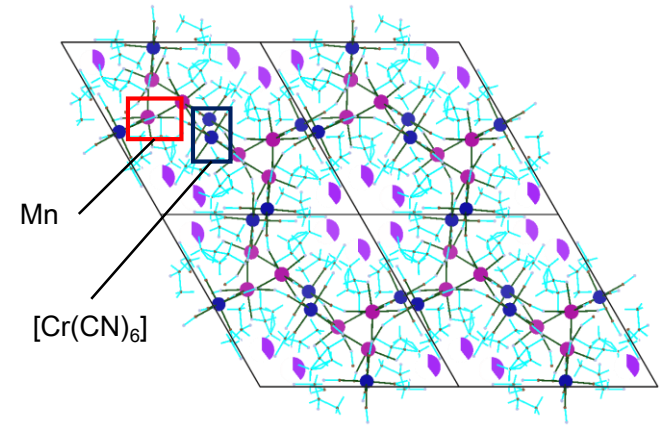

(b)

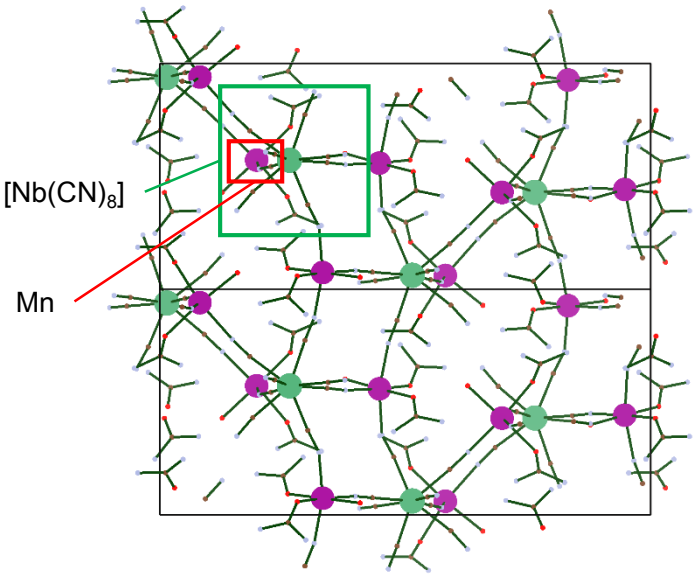

Figure 1-8. Views of examples of chiral magnets, (a) $K_{0.4}[Cr(CN)_6][Mn((S)\text{-}1,2\text{-diaminopropane})]((S)\text{-}1,2\text{-diaminopropane})_{0.6}$,[102] and (b) $[Mn(H2O)(urea)_2]_2[Nb(CN)_8]$.[87]

(a) Adapted with permission from K. Inoue, H. Imai, P. S. Ghalsasi, K. Kikuchi, M. Ohba, H. Okawa, J. V. Yakhmi, *Angew. Chem., Int. Ed.*, 2001, **40**, 4242. Copyright 2001. John Wiley & Sons, Inc.

(b) Adapted with permission from D. Pinkowicz, R. Podgajny, W. Nitek, M. Rams, A. M. Majcher, T. Nuida, S. Ohkoshi, B. Sieklucka, *Chem. Mater.*, 2011, **23**, 21. Copyright (2011) American Chemical Society.

Chapter 2: Synthesis and Crystal Structure of Mn^{II}–Nb^{IV} Cyanido Bridged Bimetal Assemblies

2.1 Introduction

Chiral structures of cyanido-bridged metal assemblies are obtained by using chiral building blocks such as chiral organic ligands. However, a small number of chiral cyanido-bridged metal assemblies can be built from achiral building blocks as a result of natural resolution. In 2014, Ohkoshi et al.[90] have reported chiral cyanido-bridged metal assembly, $[Fe(4\text{-bromopyridine})_4]_2[Nb(CN)_8]\cdot 2H_2O$, constructed from achiral building blocks (Fe^{2+}, $[Nb(CN)_8]^{4-}$, 4-bromopyridine). Various factors (coordination geometry, coordination bond, ionic radii of metal ion, hydrogen bond, π-π interaction, van der Waals force, steric hindrance, etc.) affect the formation of chiral structure when building blocks are assembled. Based on this Fe–Nb–4-bromopyridine compound, I tried to build new chiral magnets using 4-halopyridines which expects formation of halogen bonds as well as different steric hindrance depending on the halogen atoms.

In this chapter, I discuss the syntheses and the crystal structures of $[Mn(4\text{-iodopyridine})_4]_2[Nb(CN)_8]$ (**MnNbIpy**), $[Mn(4\text{-bromopyridine})_4]_2[Nb(CN)_8]\cdot 0.5H_2O$ (**MnNbBrpy**), and $[Mn(4\text{-chloropyridine})_4]_2[Nb(CN)_8]\cdot 0.5H_2O$ (**MnNbClpy**).

2.2 Experimental Details

2.2.1 Synthesis

All reagents used were purchased from commercial sources (Sigma-Aldrich, Wako Pure Chemical Industries, Ltd.) and used without further purification. $[Mn(4\text{-iodopyridine})_4]_2[Nb(CN)_8]$ (**MnNbIpy**), $[Mn(4\text{-bromopyridine})_4]_2[Nb(CN)_8]\cdot 0.5H_2O$ (**MnNbBrpy**), and $[Mn(4\text{-chloropyridine})_4]_2[Nb(CN)_8]\cdot 0.5H_2O$ (**MnNbClpy**) were synthesized according to previous report.[150,151]

2.2.1.1 $K_4[Nb(CN)_8]\cdot 2H_2O$

Firstly, $K^{I}_4[Nb^{IV}(CN)_8]\cdot 2H_2O$, the precursor of the title compounds, was synthesized according to literature method.[123] This synthesis contains three steps: (1) Electric reduction of $Nb^{V}Cl_5$ under methanol solvent, (2) Complexation reaction of Nb^{3+} and CN^- (3) Oxidation of $[Nb^{III}(CN)_8]^{5-}$ to $[Nb^{IV}(CN)_8]^{4-}$.

(1) A 50 mL three necked flask was equipped with a three-way stopcock on a side neck and a septum cap on the other side neck. $NbCl_5$ (10 g) was weighed to the 50 mL three necked flask. The central neck of the three necked flask was sealed using a septum cap penetrated by two glassy carbon electrodes. By using an Ar/vacuum line connected to the stopcock, the atmosphere of the three necked flask was replaced to Ar gas. Degassed superdehydrated methanol (40 mL) was added to the flask and the $NbCl_5$ was dissolved to the methanol. The redox reaction of the solution was conducted by 1 A constant-current electrolysis with the glassy carbon electrodes over four hours. The resulted solution became dark purple color.

(2) In a 200 mL three necked flask under Ar atmosphere being sealed, potassium cyanide (KCN, 50 g) was dissolved to degassed water (74 mL). This aqueous solution of KCN was shaded and cooled by an ice-salt bath. Into this aqueous solution of KCN, the niobium solution prepared on the step (1) was dropped slowly over one hour. The resulted red solution was stirred one hour on the ice–salt-bath, and then stirred overnight on room temperature while light shielded.

(3) The resulted red suspension of the step (2) was centrifuged (5 min. 3500 rpm) under Ar atmosphere. The precipitate was suspended on 50 mL distilled water and oxidized by hydrogen peroxide (3 mL of 10 % aqueous solution). The oxidized suspension was filtered to remove impurities and, by adding an excess amount of methanol, a crude product of $K_4[Nb(CN)_8]\cdot 2H_2O$ was obtained. Into the supernatant of the centrifuge, an excess amount of methanol was added to obtain an another crude product of $K_4[Nb(CN)_8]\cdot 2H_2O$. Two crude products were combined and were recrystallized from water/methanol. Yield 2.32 g (13 % based on Nb atom).

2.2.1.2 [Mn(4-Iodopyridine)$_4$]$_2$[Nb(CN)$_8$] (MnNbIpy)

The powder sample of the title compound was synthesized by adding an 8 mL aqueous solution of $K_4[Nb(CN)_8]\cdot 2H_2O$ (0.2 mmol) into a mixed solution of water (20 mL), ethanol (24 mL), $MnCl_2\cdot 4H_2O$ (0.4 mmol), 4-iodopyridine (2 mmol), and sodium L-ascorbate (1.0 mmol). After one hour stirring, the resulted yellow precipitate was filtered and dried overnight under air. Yield 350.1 mg (80% based on Nb atom).

The single crystal samples were synthesized by using slow diffusion method. On the bottom of a test tube, a 3 mL aqueous solution of $K_4[Nb(CN)_8]\cdot 2H_2O$ (0.05 mmol) was laid. Then water (6 mL) and a 3 mL mixed water–ethanol (1:1) solution of $MnCl_2\cdot 4H_2O$ (0.1 mmol), 4-iodopyridine (0.5 mmol), and sodium L-ascorbate (0.25 mmol) was added carefully in this order to form three layer. The test tube was kept one week on dark and yellow crystals was formed on the wall of the tube. Yield 5 mg (10 % based on Nb atom).

2.2.1.3 [Mn(4-Bromopyridine)$_4$]$_2$[Nb(CN)$_8$]·0.5H$_2$O (MnNbBrpy)

The powder sample of the title compound was synthesized by adding a 5 mL aqueous solution of $K_4[Nb(CN)_8]\cdot 2H_2O$ (0.2 mmol) into an 145 mL mixed aqueous solution of $MnCl_2\cdot 4H_2O$ (0.42 mmol), 4-bromopyridine hydrochloride (4 mmol), potassium hydroxide (4 mmol), and L-ascorbic acid (1.0 mmol). After one hour stirring, the resulted yellow precipitate was filtered and dried overnight on dried air. Yield 210 mg (61% based on Nb atom).

The single crystal samples were synthesized by using slow diffusion method. On the bottom of a test tube, a 3 mL aqueous solution of $MnCl_2\cdot 4H_2O$ (0.11 mmol), 4-bromopyridine hydrochloride (0.5 mmol), potassium hydroxide (0.5 mmol), and L-ascorbic acid (0.25 mmol) was laid. Then water (7 mL) and a 3 mL mixed water–ethanol (1:1) solution of $K_4[Nb(CN)_8]\cdot 2H_2O$ (0.05 mmol) was added carefully in this order to form three layer. The test tube was kept one week on dark and yellow crystals was formed on the wall of the tube. Yield 30 mg (40 % based on Nb atom).

2.2.1.4 [Mn(4-Chloropyridine)$_4$]$_2$[Nb(CN)$_8$]·0.5H$_2$O (MnNbClpy)

The powder sample of the title compound was synthesized using glovebox to prevent a dissociation of the compounds by humidity. Into a 32 mL aqueous solution of $MnCl_2 \cdot 4H_2O$ (0.4 mmol), 4-chloropyridine hydrochloride (4 mmol), and potassium hydroxide (4 mmol), a 8 mL aqueous solution of $K_4[Nb(CN)_8] \cdot 2H_2O$ (0.2 mmol) was added. After one hour stirring, the resulted yellow precipitate was filtered and dried overnight. Yield 190 mg (72% based on Nb atom).

The single crystal samples were synthesized by using slow diffusion method. On the bottom of a test tube, a 3 mL aqueous solution of $MnCl_2 \cdot 4H_2O$ (0.1 mmol), 4-chloropyridine hydrochloride (0.5 mmol), potassium hydroxide (0.5 mmol), and sodium L-ascorbate (0.25 mmol) was laid. Then a 7 mL water and a 3 mL mixed water–ethanol (1:1) solution of $K_4[Nb(CN)_8] \cdot 2H_2O$ (0.05 mmol) was added carefully in this order to form three layer. The test tube was kept one week on dark and yellow crystals was formed on the wall of the tube. Yield 5 mg (8 % based on Nb atom).

2.2.2 Characterization

Elemental analysis was conducted by the standard microanalytical method (for C, H, N) and by using Agilent 7700 ICP-MS (for Mn, Nb). The sample solutions used for ICP-MS were treated using aqueous solutions of ethylenediaminetetraacetic acid disodium salt (EDTA2Na).

Thermogravimetric analysis for samples was conducted with Rigaku Thermo Plus TG8120 in 27–450 °C range at a heating rate of 2 $K \cdot min^{-1}$.

UV-Vis-NIR spectra of samples were measured by using Shimadzu UV-3100PC spectrometer or Shimadzu UV-3600 PLUS employing diffuse reflectance method on samples mixed in $BaSO_4$. The reflection spectra of UV-Vis-NIR were transformed to absorption spectra by using Kubelka–Munk equation. IR absorption spectra of samples were obtained by using JASCO FT/IR-4100 spectrometer with samples shaped to KBr pellets.

2.2.3 Single Crystal X-ray Diffraction Studies

Single crystal samples suitable for X-ray crystal structural analysis were coated with Paratone-N oil, picked on pen tips, and mounted onto a goniometer. The measurements were conducted on room temperature and on 90 K under N_2 flow with Rigaku RAXIS RAPID imaging plate area detector, equipped with graphite monochromated MoKα radiation.

The initial structures were solved by using SHELXS-2013, SHELXT-2013, or Sir2014; refined by full-matrix least-squares methods based on F^2 using SHELXL-2013; and these analyses were conducted on Rigaku Crystal Structure software and WinGX (ver. 1.80.05) software.[124–126]

For **MnNbIpy**, a twinning with a 2-fold rotation along [0 1 0] as twin element were assumed because a preliminary analysis where twinning was not assumed showed an irrational structural model. Because of structural chirality of **MnNbIpy**, the analyses were conducted with four domains model.

All non-hydrogen atoms except solvent waters suggested by elemental analyses were found independently and refined with anisotropic temperature factor. On the refinement of **MnNbIpy**, temperature factors of several C and N atomic sites were restricted to avoid the non-positive definite because sometimes the twin refinements produce a difficult situation where atomic sites are close after moved by the twin operation and the temperature factors of them are strongly related. Hydrogen atoms belonging to 4-halopyridine ligands were introduced by the idealized positons with the riding model. The solvent molecules could not be determined for the possible structural disorders. The continuous shape measures of metal ion sites were conducted by SHAPE software ver. 2.1.[128] Structural figures were created by VESTA software.[127]

The results is corresponding to CCDC-1854369, -1854370, -1854373, and -1854374 for **MnNbIpy**; CCDC-1472543 and -1472546 for **MnNbBrpy**; and CCDC-1854371 and -1854372 for **MnNbClpy**.[150,151]

2.2.4 The powder X-ray Diffraction Patterns

The powder X-ray diffraction (PXRD) patterns in the 2θ range of 5–70° were obtained with Rigaku Ultima IV diffractometer or Rigaku MiniFlex equipped with the CuKα radiation (1.5419 Å). Obtained patterns were processed with Rigaku PDXL software by using Rietveld analysis where the initial structures were taken from the results of the single crystal XRD analyses of the corresponding single crystal samples.

The PXRD pattern of **MnNbClpy** shows considerable amount of peaks from an impurity. This impurity are identified as $Mn_2[Nb(CN)_8]\cdot 8H_2O$ compound by the analysis of patterns.[129] It is estimated that dozens per cent of **MnNbClpy** is decomposed to $Mn_2[Nb(CN)_8]\cdot 8H_2O$ under air within 4–6 hours because the peaks of the impurity became stronger with repeating measurement for **MnNbClpy**.

2.3 Results and Discussion

2.3.1 Elemental Analysis

The results of elemental analyses for **MnNbIpy**, **MnNbBrpy**, and **MnNbClpy** (Table 2-1) suggest that the compositional formulae of **MnNbIpy**, **MnNbBrpy**, and **MnNbClpy** are $C_{48}H_{32}I_8Mn_2N_{16}Nb_1$, $C_{48}H_{33}Br_8Mn_2N_{16}Nb_1O_{0.5}$, and $C_{48}H_{33}Cl_8Mn_2N_{16}Nb_1O_{0.5}$, respectively. The rational formulae of **MnNbIpy**, **MnNbBrpy**, and **MnNbClpy** are $[Mn(4\text{-iodopyridine})_4]_2[Nb(CN)_8]$, $[Mn(4\text{-bromopyridine})_4]_2[Nb(CN)_8]\cdot 0.5H_2O$, and $[Mn(4\text{-chloropyridine})_4]_2[Nb(CN)_8]\cdot 0.5H_2O$, respectively. Each samples contains eight 4-halopyridine, two Mn ions, and no or less than one water molecule, per one $[Nb(CN)_8]$ moiety.

2.3.2 Thermogravimetric Measurements

The results of thermogravimetric measurements are depicted as Figure 2-1. In **MnNbIpy**, the results show that there are no significant change until around 345 K, then the mass become decreasing. During 410 K to 467 K, a substantial mass decrease to 22 % of that of 300 K which should represent decomposition of **MnNbIpy** compound was observed.

This outline is similar to **MnNbBrpy** and **MnNbClpy**. In **MnNbBrpy**, the result shows that, there are no significant change until around 372 K, then the mass become decreasing. During 383 K to 500 K, a substantial mass decrease to 76 % of that of 300 K which should represent decomposition of **MnNbBrpy** was observed.

In **MnNbClpy**, there are no significant change until around 355 K, then the mass become decreasing. During 405 K to 453 K the weight decreased to 34 % of that of 300 K, which should represent decomposition of **MnNbClpy**.

2.3.3 Crystal Structures

The results of the single crystal X-ray diffraction analyses for **MnNbIpy**, **MnNbBrpy**, and **MnNbClpy** are shown in Table 2-2, 2-3, and 2-4.

2.3.3.1 MnNbIpy

The crystallographic parameters of the single crystal measurements are depicted on Table 2-2, and structural parameters are shown in Table 2-3. Because **MnNbIpy** are a chiral compound, there exist two enantiomers named **MnNbIpy(+)** and **MnNbIpy(−)**. They belongs to different enantiomers each other. The description below are mostly based on the crystal structure of **MnNbIpy(+)** at 90 K.

MnNbIpy(+) belongs to a tetragonal non-centrosymmetric space group $I4_1$ (Figure 2-2). The asymmetric unit contains a half of $[Nb^{IV}(CN)_8]$, one Mn^{2+} ion and four 4-iodopyridine ligands (Figure 2-5a). Distorted octahedral Mn^{2+} ions and distorted square antiprism $[Nb^{IV}(CN)_8]$ moieties form a three-dimensional (3-D) cyanido-bridged coordination network. This 3-D network shows diamond-like topology where a Nb^{4+} ion is connected to four Nb^{4+} ions via –CN–Mn–NC– moieties. Four equatorial sites of the Mn^{2+} ion are occupied by four N atoms of 4-iodopyridine and two axial sites are occupied by the N atoms of the cyanido ligands (Figure 2-6a, Table 2-4). Among eight cyanido ligands of $[Nb^{IV}(CN)_8]$, four cyanido ligands are bridging to the Mn^{2+} ions and the other four cyanido ligands are terminal ligands. Among four 4-iodopyridine ligands, which are coordinated to one Mn^{2+} ion, two are almost

parallel to the *ab*-plane and the other two are aligned to the *c*-axis. This compound contains two types of bridging cyanido ligands. The two angles ∠Mn–N–C are slightly different in 90 K (174.1(7)° and 164.5(6)°) and similar in room temperature (169.8(13)° and 170.6(12)°).

In this crystal structure, there are halogen bondings between the iodine atoms of 4-iodopyridine aligned to the *c*-axis and the nitrogen atoms of the terminal cyanido ligands (Figure 2-7a). The distance between the iodine atoms from the 4-iodopyridine ligands and the nitrogen atoms of terminal cyanido (CN) ligands (3.044(8) Å, and 3.107(8) Å) are smaller than the sum of van der Waals (vdW) radii (3.53 Å), and the angles ∠C–I···N (176.5(3)° and 166.0(3)°) are close to 180°. These two characteristics confirm that there are halogen bonding between the iodine atoms and the nitrogen atoms.

The 3-D coordination network of **MnNbIpy** is diamond type and the ···Nb^{IV}–CN–Mn^{II}–Nb^{IV}··· coordination chain forms helical structures (Figure 2-8a, 2-9a). The helical structures show pseudo-square shape from the view of the *c*-axis. The lattice *ab*-plane contains four such helices. The halogen bondings, which aligned to the *c*-axis, are exist on side surface of the coordination helix. Because the neighboring helices have opposite handedness and different shape (narrow type and thick type), there are narrow right-handed helices and thick left-handed helices in **MnNbIpy(+)** and this cause chirality. **MnNbIpy(−)** contains narrow left-handed helices and thick right-handed helices. Maybe, these halogen bondings distort the helical structure and cause two types of them and chirality.

2.3.3.2 MnNbBrpy

The crystallographic parameters of the single crystal measurements for **MnNbBrpy** are depicted on Table 2-2, and structural parameters are shown in Table 2-3.

The crystal structure of **MnNbBrpy** belongs to a non-centrosymmetric space group $I4_122$. This space group is tetragonal (Figure 2-3) and the supergroup of the space group $I4_1$ which **MnNbIpy** belongs to. The asymmetric unit contains a quarter of $[Nb^{IV}(CN)_8]$, a half of Mn^{II}, and one complete and two half 4-bromopyridine (Figure 2-5b). This compound have a diamond type 3-D cyanido-bridged coordination network, composed of distorted square

antiprism $[Nb^{IV}(\mu\text{-}CN)_4(CN)_4]$ and distorted octahedral $[Mn^{II}(4\text{-bromopyridine})_4(\mu\text{–}NC)_2]$ moieties. This network is similar to that of **MnNbIpy**. In this network a Nb^{4+} ion are bridging to four Nb^{4+} ions via –CN–Mn–NC– moieties. Four equatorial sites of a Mn^{2+} ion are occupied by four nitrogen atoms of 4-bromopyridine ligands and two axial sites are occupied by two nitrogen atoms of the bridging cyanido ligands (Figure 2-6b, Table 2-4). Among four 4-bromopyridine ligands coordinated to one Mn^{2+} ions, two 4-bromopyridine form halogen bonding between the Br atoms and the N atoms of terminal cyanido ligands (∠C–Br···N = 170.83°, Br···N = 3.084 Å, sum of vdW radii = 3.40 Å, Figure 2-7b). This compound has helical structures aligned to the *c*-axis and the lattice *ab*-plane contains four such helices (Figure 2-8b, 2-9b). The helical structures show pseudo-square shape from the view of the *c*-axis. There are narrow right-handed helices and thick left-handed helices in **MnNbBrpy(+)** and this causes chirality. **MnNbBrpy(−)** contains narrow left-handed helices and thick right-handed helices.

2.3.3.3 MnNbClpy

The crystallographic parameters of the single crystal measurements for **MnNbClpy** are depicted on Table 2-2, and structural parameters are shown in Table 2-3.

This compound belongs to a centrosymmetric space group *Fddd*, which belongs to the orthorhombic system (Figure 2-4). The asymmetric unit contains a quarter of $[Nb^{IV}(CN)_8]$, a half of Mn^{II} and two complete 4-chloropyridine (Figure 2-5c). This compound have a 3-D cyanido-bridged coordination network, composed of distorted square antiprism $[Nb^{IV}(\mu\text{-}CN)_4(CN)_4]$ and distorted octahedral $[Mn^{II}(4\text{-chloropyridine})_4(\mu\text{-}NC)_2]$ moieties (Figure 2-6c, Table 2-4). This network is diamond-type network and is similar to that of **MnNbIpy**. In this network a Nb^{4+} ion are bridging to four Nb^{4+} ions via –CN–Mn–NC– moieties. Four equatorial sites of the Mn^{2+} ion are occupied by four 4-chloropyridine ligands and two axial sites are occupied by two bridging cyanido ligands. Among four 4-chloropyridine ligands coordinated to one Mn^{2+} ion, two 4-chloropyridine form halogen bondings between the Cl

atoms and the N atoms of terminal cyanido ligands (∠C–Cl···N = 166.79°, Cl···N = 3.183 Å, sum of vdW radii = 3.30 Å, Figure 2-7c).

MnNbClpy has the diamond-type 3-D coordination network and there are helices with the Nb^{IV}–CN–Mn^{II}–Nb^{IV}··· coordination chain. The helical structures show pseudo-lozenge shape from the view of the *a*-axis. The lattice *bc*-plane contains eight helical structures aligned to the *a*-axis. Unlike **MnNbIpy** and **MnNbBrpy**, the neighboring helices are related by the inversion operation and have the same shape and the different handedness, and then this compound is achiral (Figure 2-8c, 2-9c). The structure of **MnNbClpy** is very similar to that of the reported $[Ni^{II}(4\text{-bromopyridine})_4]_2[Nb^{IV}(CN)_8]\cdot 2H_2O$ congener.[150]

2.3.3.5 Comparison of Structures of Compounds

MnNbIpy, **MnNbBrpy**, and **MnNbClpy** have similar several structural characteristics. the $[Nb^{IV}(CN)]$ moieties adopt distorted square antiprism geometry and among eight cyanido ligands, four ligands are terminal ones and the other four are bridging to Mn^{2+} ions. The Mn^{2+} ions are six-coordinated in the distorted octahedral geometries with two axial N atoms of cyanido ligands and four equatorial N atoms of 4-halopyridine ligands. They have 3-D cyanido-bridged coordination networks of diamond-type, where Nb^{4+} ions in compounds are comparable to C atoms in diamond-type network. These networks show channels and coordination helices around the channels. There are halogen bondings between halogens of 4-halopyridine and N atoms of terminal cyanido ligands of the $[Nb^{IV}(CN)]$ moiety. All four terminal cyanido ligands of the $[Nb^{IV}(CN)]$ moiety participate in these halogen bondings. These halogen bondings exist on the side surfaces of the coordination helices.

Although **MnNbIpy**, **MnNbBrpy**, and **MnNbClpy** have similar structures as seen above, they shows significant difference on the symmetries and other features. Despite having same bonding geometry, the shapes of the coordination helices differs significantly i.e., pseudo-lozenge shape for achiral **MnNbClpy** from the view of the *a*-axis and pseudo-square shape for **MnNbIpy** and **MnNbBrpy** from the view of the *c*-axis. Also **MnNbIpy** and **MnNbBrpy** consist of two types of the coordination helices (narrow and thick helices) and

this make these compounds chiral. Other difference is dihedral angles of two cyanido ligands coordinated to one Mn^{2+} ion. This dihedral angle show 180 degree for achiral **MnNbClpy** but tens of degrees for **MnNbIpy** and **MnNbBrpy**, and the directions of 4-halopyridine ligands around Mn^{2+} ions are different.

2.3.4 PXRD Patterns

The result of powder X-ray diffraction measurements are shown in Figure 2-10. These results are analyzed well to show powder samples have the same structure to the corresponding single crystal samples.

2.3.5 Optical Spectra

The results of UV-Vis-NIR spectroscopic study (200–1500 nm) are shown in Figure 2-11, and that of IR spectroscopy are shown in Figure 2-12.

The result of UV-Vis-NIR spectroscopic study (200–1500 nm) is written below. In long wave length region (800–1500 nm), no peaks are detected. This suits well to spin forbidden character of d–d transitions from d^5 Mn^{II}_{HS} ions. In short wave length region (<800 nm), there are several peaks. Peaks around 400–500 nm region should be assigned to d–d transitions of Nb^{4+} ions of $[Nb^{IV}(CN)_8]^{4-}$ moieties and peaks around 200–400 nm region should be assigned to ligand-to-metal charge transfer (LMCT) transitions of $[Nb^{IV}(CN)_8]^{4-}$ moieties[87,98] or peaks from 4-halopyridine ligands. Very weak peaks around 600–700 nm should be assigned to poly(1,4-pyridinium) salts impurity.[130–133]

The result of IR spectroscopic study is written below. In lower frequency region (2000–400 cm^{-1}), peaks from 4-halopyridine ligands are detected. These peaks are assigned to stretching peaks of pyridine rings, bending vibration of C–H bond, and vending peaks of pyridine rings.

The stretching peaks of cyanido ligands are discovered in 2100–2200 cm^{-1} region. For all compounds, there exist two stretching peaks of cyanido ligands, which consist of a weaker lower-wave-number one and a stronger higher-wave-number one. The weaker lower-wave-

number peaks are assigned to terminal cyanido ligand and the stronger higher-wave-number ones are bridging one. When cyanido ligands coordinated to a Mn^{2+} ion, electrons in an antibonding σ orbital of the cyanido ligand is donated to the Mn^{2+} ion and the C≡N bonding becomes stronger. Then the higher-wave-number peaks were assigned to the bridging ligands. In **MnNbIpy** compound, the bonding between the Mn^{2+} ion and cyanido ligands are relatively weak compared to **MnNbBrpy** and **MnNbClpy** (the Mn–N(CN) distances are 2.168(15) and 2.192(13) Å in **MnNbIpy(+)**, 2.125(4) in **MnNbBrpy(+)**, 2.115(3) Å in **MnNbClpy** at room temperature). For this reason, the peak of **MnNbIpy** shows lower wave number.

Broad peaks assigned to water molecule are placed in over 3000 cm^{-1} region. These peaks are weaker than that of reported $[Fe(4\text{-bromopyridine})_4]_2[Nb(CN)_8]\cdot 2H_2O$ congener, which should mean the amounts of the crystalline waters of the compounds are smaller than that.[90]

2.4 Conclusion

Three cyanido-bridged bimetal assemblies, $[Mn(4\text{-iodopyridine})_4]_2[Nb(CN)_8]$ (**MnNbIpy**), $[Mn(4\text{-bromopyridine})_4]_2[Nb(CN)_8]\cdot 0.5H_2O$ (**MnNbBrpy**), and $[Mn(4\text{-chloropyridine})_4]_2[Nb(CN)_8]\cdot 0.5H_2O$ (**MnNbClpy**) have been synthesized in both sample states of single crystal and powder.

Single crystal X-ray structural analysis showed that **MnNbIpy** has the chiral tetragonal structure with the space group $I4_1$ and **MnNbBrpy** also has the chiral tetragonal structure with the space group $I4_122$. This space group $I4_122$ is one of the supergroup of the space group $I4_1$. On the other hand, **MnNbClpy** shows the achiral orthorhombic structure with the space group *Fddd*. These three compounds contain the 3-D coordination networks. In these 3-D coordination networks, there are the helical structures along the *c*-axis for **MnNbIpy** and **MnNbBrpy** or the *a*-axis for **MnNbClpy**. There are two types of helical structures in **MnNbIpy** and **MnNbBrpy**, while only one type is founded in **MnNbClpy**. This differences in the two helical structures are the reasons for chiral structures of **MnNbIpy** and **MnNbBrpy**. There are halogen bondings along the direction of the coordination helices between the halogen atom of the 4-halopyridine

ligands and the N atom of the terminal cyanido ligands. The halogen bonding in **MnNbIpy** and **MnNbBrpy** is stronger than that of **MnNbClpy**. In **MnNbIpy** and **MnNbBrpy**, the coordination geometries around the Mn^{2+} ions are distorted by the halogen bonding, forming the two types of helical structures that lead to the chiral structure.

Table 2-1. Results of Elemental Analysis.

MnNbIpy	$[Mn(4\text{-iodopyridine})_4]_2[Nb(CN)_8]$ $C_{48}H_{32}I_8Mn_2N_{16}Nb_1$				
	C	H	N	Mn	Nb
Calcd.	28.11	1.57	10.93	5.36	4.53
Found.	28.26	1.97	10.90	5.52	4.56
MnNbBrpy	$[Mn(4\text{-bromopyridine})_4]_2[Nb(CN)_8]\cdot 0.5H_2O$ $C_{48}H_{33}Br_8Mn_2N_{16}Nb_1O_{0.5}$				
	C	H	N	Mn	Nb
Calcd.	34.24	1.98	13.31	6.53	5.52
Found.	34.26	1.97	13.28	6.56	5.31
MnNbClpy	$[Mn(4\text{-chloropyridine})_4]_2[Nb(CN)_8]\cdot 0.5H_2O$ $C_{48}H_{33}Cl_8Mn_2N_{16}Nb_1O_{0.5}$				
	C	H	N	Mn	Nb
Calcd.	43.39	2.50	16.87	8.27	7.00
Found.	43.41	2.45	16.88	7.97	7.21

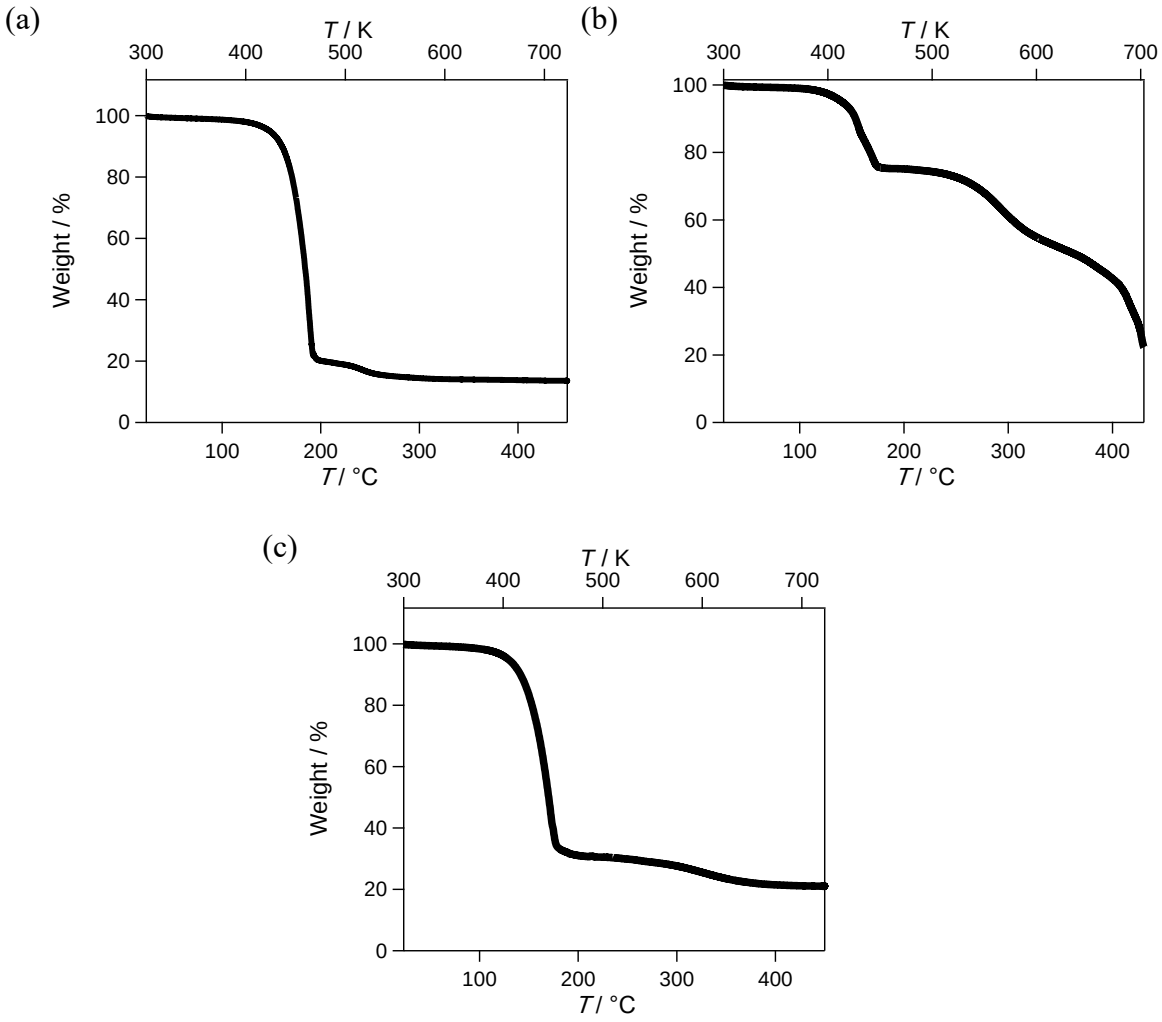

Figure 2-1. Results of thermogravimetric measurements for (a) MnNbIpy, (b) MnNbBrpy, and (c) MnNbClpy in the 27–450 °C range under a scan rate of 2 K·min^{-1}.

Adapted from Ref. [151] with permission from the Royal Society of Chemistry.

Table 2-2. Crystal Data and Structural Refinements.

compound	**MnNbIpy(+)**		**MnNbIpy(−)**	
formula	$C_{48}H_{32}I_8Mn_2N_{16}Nb_1$	$C_{48}H_{32}I_8Mn_2N_{16}Nb_1$	$C_{48}H_{32}I_8Mn_2N_{16}Nb_1$	$C_{48}H_{32}I_8Mn_2N_{16}Nb_1$
formula weight [g·mol^{-1}]	2050.89	2050.89	2050.89	2050.89
crystal size [mm × mm × mm]	0.23×0.21×0.21	0.23×0.21×0.21	0.23×0.20×0.20	0.17×0.15×0.10
T [K]	300	90	295	90
crystal system	tetragonal	tetragonal	tetragonal	tetragonal
space group	$I4_1$	$I4_1$	$I4_1$	$I4_1$
a [Å] b [Å] c [Å]	20.8730(7) 20.8730(7) 14.2157(4)	20.7954(7) 20.7954(7) 14.1103(5)	20.8811(9) 20.8811(9) 14.2190(4)	20.792(2) 20.792(2) 14.1122(7)
V [Å^3]	6193.5(5)	6102.0(5)	6199.8(6)	6100.8(12)
Z	4	4	4	4
calculated density [g·cm^{-3}]	2.199	2.232	2.197	2.233
absorption coefficient [mm^{-1}]	4.617	4.687	4.613	4.688
F(000)	3788.0	3788.0	3788.0	3788.0
θ range [deg.]	3.086–27.460	3.098–27.472	3.085–27.471	3.098–27.483
hkl indices	−24<h<27 −27<k<27 −18<l<18	−23<h<26 −26<k<24 −18<l<18	−27<h<25 −26<k<27 −18<l<18	−26<h<26 −26<k<26 −18<l<18
observed reflections	43746	48185	43344	46794
symmetry–independent reflections	7084	6988	6964	6889
R_{int}	0.038	0.032	0.0421	0.064
completeness	0.995	0.997	0.997	0.997
data/restraints/parameters	7084/33/342	6988/7/342	6964/5/342	6889/29/342
GOF on F^2	1.142	1.062	1.087	1.090
$R[F^2 > 2\sigma(F^2)]$	0.0458	0.0217	0.0455	0.0270
$wR(F^2)$	0.1144	0.0526	1.088	0.0652
largest diff peak/hole [e·Å^{-3}]	2.131/−1.657	1.571/−0.834	2.008/−1.416	0.964/−0.891

Adapted from Ref. [151] with permission from the Royal Society of Chemistry.

Table 2-2. Crystal Data and Structural Refinements. (Continued)

compound	**MnNbBrpy(+)**		**MnNbBrpy(−)**		**MnNbClpy**	
formula	$C_{48}H_{33}Br_8Mn_2N_{16}Nb_1O_{0.5}$	$C_{48}H_{33}Br_8Mn_2N_{16}Nb_1O_{0.5}$	$C_{48}H_{33}Br_8Mn_2N_{16}Nb_1O_{0.5}$	$C_{48}H_{33}Br_8Mn_2N_{16}Nb_1O_{0.5}$	$C_{48}H_{32}Cl_8Mn_2N_{16}Nb_1O_{0.5}$	$C_{48}H_{32}Cl_8Mn_2N_{16}Nb_1O_{0.5}$
formula weight [g·mol^{-1}]	1674.89	1674.89	1674.89	1674.89	1328.73	1328.73
crystal size [mm×mm×mm]	0.33×0.29×0.18	0.33×0.29×0.18	0.40×0.37×0.34	0.26×0.10×0.09	0.18×0.11×0.11	0.18×0.11×0.11
T [K]	293	90	293	90	296	90
crystal system	tetragonal	tetragonal	tetragonal	tetragonal	orthorhombic	orthorhombic
space group	$I4_122$	$I4_122$	$I4_122$	$I4_122$	*Fddd*	*Fddd*
a [Å]	20.6168(12)	20.5345(12)	20.599(2)	20.5122(11)	13.9379(3)	13.7697(5)
b [Å]	20.6168(12)	20.5345(12)	20.599(2)	20.5122(11)	26.6853(5)	26.2046(9)
c [Å]	14.0220(4)	13.8992(4)	14.0190(8)	13.9053(4)	31.5931(6)	31.9937(12)
V [Å^3]	5960.1(7)	5860.8(7)	5948.4(14)	5850.7(6)	11750.6(4)	11544.3(7)
Z	4	4	4	4	8	8
calculated density [g·cm^{-3}]	1.867	1.898	1.870	1.901	1.491	1.518
absorption coefficient [mm^{-1}]	6.017	6.119	6.029	6.130	1.027	1.045
F(000)	3212	3212.0	3212	3212.0	5272.0	5272
θ range [deg.]	3.125–27.471	3.137–27.479	3.127–23.241	3.141–27.477	3.053–27.479	3.110–27.480
hkl indices	$-26<h<26$ $-26<k<25$ $-18<l<17$	$-26<h<26$ $-26<k<26$ $-18<l<18$	$-22<h<22$ $-22<k<22$ $-15<l<15$	$-26<h<26$ $-26<k<26$ $-18<l<18$	$-18<h<17$ $-34<k<34$ $-40<l<40$	$-17<h<17$ $-34<k<33$ $-41<l<41$
observed reflections	27757	45398	19190	47004	37235	44534
symmetry–independent reflections	3405	3347	2138	3353	3378	3310
R_{int}	0.0933	0.0699	0.1086	0.0885	0.044	0.034
completeness	0.997	0.997	0.996	0.996	0.999	0.999
data/restraints/parameters	27757/0/175	3347/0/174	19190/0/174	3357/7/174	3378/0/172	44534/0/172
GOF on F^2	1.056	1.571	1.070	0.954	1.368	1.481
$R[F^2 > 2\sigma(F^2)]$	0.0415	0.0202	0.0392	0.0420	0.0589	0.0453
$wR(F^2)$	0.0728	0.423	0.0578	0.0485	0.1080	0.0702
largest diff peak/hole [e·Å^{-3}]	0.544/−0.480	0.310/−0.510	0.558/−0.511	1.045/−0.656	0.487/−0.692	0.476/−0.443
Flack x parameter	0.132(6)	0.109(3)	0.047(8)	0.077(4)	–	–

Modified and reproduced with permission from T. Ohno, S. Chorazy, K. Imoto, S. Ohkoshi, *Cryst. Growth Des.*, 2016, **16**, 4119. Copyright 2016 American Chemical Society.

Adapted from Ref. [151] with permission from the Royal Society of Chemistry.

Table 2-3. Detailed Structural Parameters.

compound	**MnNbIpy(+)**	**MnNbIpy(−)**
Temperature (K)	90	90
Halogen Bonding		
N3···I17 [Å]	3.107(8)	3.106(9)
∠N3···I17–C14 [°]	166.0(3)	166.5(3)
N4···I27	3.044(7)	3.061(8)
∠N4···I27–C24	176.5(3)	176.5(3)
$[Nb^{IV}(CN)_8]$ moiety		
Nb1–C1	2.227(7)	2.246(9)
Nb1–C2	2.238(8)	2.223(8)
Nb1–C3	2.287(9)	2.287(9)
Nb1–C4	2.269(8)	2.287(9)
C–N (bonding)	1.154(10), 1.152(11)	1.146(11), 1.146(11)
C–N (terminal)	1.111(12), 1.157(11)	1.122(12), 1.118(12)
∠Nb1–C1–N1	178.4(7)	179.4(8)
∠Nb1–C2–N2	179.8(8)	179.0(8)
∠Nb1–C3–N3	175.8(7)	179.0(8)
∠Nb1–C4–N4	179.8(8)	174.8(8)
$[Mn^{II}(4\text{-Ipy})_4(NC)_2]$ moiety		
Mn1–N1 (CN)	2.153(7)	2.156(7)
Mn1–N2 (CN)	2.160(7)	2.167(8)
Mn1–N11 (Ipy)	2.298(7)	2.301(8)
Mn1–N21 (Ipy)	2.307(7)	2.311(8)
Mn1–N31 (Ipy)	2.308(7)	2.310(8)
Mn1–N41 (Ipy)	2.313(6)	2.301(7)
∠Mn1–N1–C1	174.1(7)	164.6(7)
∠Mn1–N2–C2	164.5(6)	173.4(7)
∠N1–Mn1–N2	177.4(3)	177.1(3)
∠N11(Ipy)–Mn–N21(Ipy)	172.6(2)	173.1(3)
∠N11(Ipy)–Mn–N31(Ipy)	94.3(3)	92.6(3)
∠N11(Ipy)–Mn–N41(Ipy)	85.0(3)	88.2(3)
∠N21(Ipy)–Mn–N31(Ipy)	93.1(3)	94.3(3)
∠N21(Ipy)–Mn–N41(Ipy)	87.6(3)	85.0(3)
∠N31(Ipy)–Mn–N41(Ipy)	178.6(3)	178.2(3)
∠N(Ipy)–Mn–N(CN)	87.3(3)–91.6(3)	86.9(3)–91.5(3)

Adapted from Ref. [151] with permission from the Royal Society of Chemistry.

Table 2-3. Detailed Structural Parameters. (Continued)

compound	**MnNbIpy(+)**	**MnNbIpy(−)**
Temperature (K)	300	295
Halogen Bonding		
N3···I17	3.086(14)	3.090(15)
∠N3···I17–C14	177.3(6)	176.9(6)
N4···I27	3.199(16)	3.189(15)
∠N4···I27–C24	166.7(7)	166.4(7)
$[Nb^{IV}(CN)_8]$ moiety		
Nb1–C1	2.208(17)	2.230(19)
Nb1–C2	2.289(12)	2.266(12)
Nb1–C3	2.258(13)	2.295(16)
Nb1–C4	2.25(2)	2.245(16)
C–N (bonding)	1.18(2), 1.069(17)	1.17(2), 1.094(19)
C–N (terminal)	1.18(2), 1.13(3)	1.14(2), 1.14(2)
∠Nb1–C1–N1	172.2(15)	173.1(15)
∠Nb1–C2–N2	176.2(11)	177.0(11)
∠Nb1–C3–N3	177.1(13)	178.0(15)
∠Nb1–C4–N4	173(2)	174.7(17)
$[Mn^{II}(4\text{-Ipy})_4(NC)_2]$ moiety		
Mn1–N1 (CN)	2.168(15)	2.154(12)
Mn1–N2 (CN)	2.192(13)	2.195(15)
Mn1–N11 (Ipy)	2.328(14)	2.321(15)
Mn1–N21 (Ipy)	2.297(15)	2.316(12)
Mn1–N31 (Ipy)	2.313(14)	2.307(14)
Mn1–N41 (Ipy)	2.324(10)	2.323(10)
∠Mn1–N1–C1	169.8(13)	171.5(12)
∠Mn1–N2–C2	170.6(12)	170.8(12)
∠N1–Mn1–N2	177.2(4)	177.6(4)
∠N11(Ipy)–Mn–N21(Ipy)	173.9(4)	173.3(5)
∠N11(Ipy)–Mn–N31(Ipy)	92.6(6)	91.4(6)
∠N11(Ipy)–Mn–N41(Ipy)	87.1(6)	86.5(7)
∠N21(Ipy)–Mn–N31(Ipy)	93.3(7)	94.6(6)
∠N21(Ipy)–Mn–N41(Ipy)	87.0(7)	87.5(7)
∠N31(Ipy)–Mn–N41(Ipy)	179.7(9)	177.2(7)
∠N(Ipy)–Mn–N(CN)	87.8(6)–92.0(6)	86.4(6)–91.9(5)

Adapted from Ref. [151] with permission from the Royal Society of Chemistry.

Table 2-3. Detailed Structural Parameters. (Continued)

compound	**MnNbBrpy(+)**	**MnNbBrpy(+)**	**MnNbBrpy(–)**	**MnNbBrpy(–)**
Temperature (K)	90	293	90	293
Halogen Bonding				
N2···Br1	3.087(3)	3.156(5)	3.078(4)	3.161(9)
∠N2···Br1–C5	170.78(11)	171.7(2)	170.96(19)	171.8(4)
$[Nb^{IV}(CN)_8]$ moiety				
Nb1–C1 (bonding)	2.220(3)	2.225(4)	2.214(5)	2.229(7)
Nb1–C2 (terminal)	2.262(3)	2.256(5)	2.270(5)	2.260(7)
C1–N1 (bonding)	1.153(4)	1.140(6)	1.153(6)	1.141(8)
C2–N2 (terminal)	1.143(4)	1.141(6)	1.145(6)	1.131(8)
∠Nb1–C1–N1	178.5(3)	179.6(5)	178.9(5)	179.9(8)
∠Nb1–C2–N2	178.8(3)	179.5(5)	178.6(5)	179.6(8)
$[Mn^{II}(4\text{-Brpy})_4(NC)_2]$ moiety				
Mn1–N1 (CN)	2.111(3)	2.125(4)	2.109(4)	2.115(6)
Mn1–N3 (Brpy)	2.317(4)	2.323(4)	2.321(4)	2.331(6)
Mn1–N4 (Brpy)	2.356(4)	2.336(6)	2.352(6)	2.324(9)
Mn1–N5 (Brpy)	2.317(4)	2.352(6)	2.321(7)	2.333(10)
∠Mn1–N1–C1	166.4(3)	168.9(4)	166.8(5)	168.9(6)
∠N3(Brpy)–Mn–N3(Brpy)	171.60(14)	172.8(2)	171.7(2)	173.4(3)
∠N3(Brpy)–Mn–N4(Brpy)	94.20(7)	93.63(10)	94.14(12)	93.30(16)
∠N3(Brpy)–Mn–N5(Brpy)	85.80(7)	86.37(10)	85.86(12)	86.70(16)
∠N4(Brpy)–Mn–N5(Brpy)	180	180	180	180
∠N(CN)–Mn–N(CN)	176.32(15)	176.9(2)	176.6(3)	176.8(4)
∠N(Brpy)–Mn–N(CN)	88.16(7)–91.84(7)	88.45(12)–91.55(12)	88.30(13)–91.70(13)	88.40(18)–90.9(20)

Modified and reproduced with permission from T. Ohno, S. Chorazy, K. Imoto, S. Ohkoshi, *Cryst. Growth Des.*, 2016, **16**, 4119. Copyright 2016 American Chemical Society.

Adapted from Ref. [151] with permission from the Royal Society of Chemistry.

Table 2-3. Detailed Structural Parameters. (Continued)

compound	**MnNbClpy**	**MnNbClpy**
Temperature (K)	296	90
Halogen Bonding		
N2···Cl3	3.281(4)	3.183(2)
∠N2···Cl3–C10	168.98(18)	166.79(10)
$[Nb^{IV}(CN)_8]$ moiety		
Nb1–C1 (bonding)	2.222(3)	2.216(2)
Nb1–C2 (terminal)	2.264(3)	2.266(2)
C1–N1 (bonding)	1.139(4)	1.150(3)
C2–N2 (terminal)	1.140(4)	1.149(3)
∠Nb1–C1–N1	178.6(3)	178.7(2)
∠Nb1–C2–N2	178.3(4)	177.8(2)
$[Mn^{II}(4\text{-Clpy})_4(NC)_2]$ moiety		
Mn1–N1 (CN)	2.115(3)	2.107(2)
Mn1–N3 (Clpy)	2.343(3)	2.315(2)
Mn1–N4 (Clpy)	2.326(3)	2.332(2)
∠Mn1–N1–C1	170.5(3)	169.1(2)
∠N3(Clpy)–Mn–N3(Clpy)	180	180
∠N4(Clpy)–Mn–N4(Clpy)	180	180
∠N3(Clpy)–Mn–N4(Clpy)	89.32(11), 90.67(11)	89.04(7), 90.96(7)
∠N(Clpy)–Mn–N(CN)	89.13(11)–90.87(11)	88.91(8) – 91.09(8)

Adapted from Ref. [151] with permission from the Royal Society of Chemistry.

Table 2-4. Results of Continuous Shape Measure of Metal Ions in Compounds.

(a) Nb^{4+} ions. (b) Mn^{2+} Ions.

(a)

Nb^{4+} ion		CShM parameters			Geometry
		BTP-8	SAPR-8	DD-8	
MnNbIpy(+)	RT	1.934	0.183	2.052	SAPR-8
	90 K	2.191	0.118	2.500	SAPR-8
MnNbIpy(−)	RT	1.955	0.170	2.117	SAPR-8
	90 K	2.183	0.115	2.497	SAPR-8
MnNbBrpy(+)	RT	2.052	0.106	2.301	SAPR-8
	90 K	2.302	0.077	2.547	SAPR-8
MnNbBrpy(−)	RT	2.042	0.118	2.265	SAPR-8
	90 K	2.303	0.081	2.539	SAPR-8
MnNbClpy	RT	2.007	0.155	2.115	SAPR-8
	90 K	2.221	0.120	2.576	SAPR-8

CShM parameters.

BTP-8 = the parameter related to the bicapped trigonal prism geometry (C2v symmetry)

SAPR-8 = the parameter related to the square antiprism (D4d symmetry)

DD-8 = the parameter related to the dodecahedron (D2d symmetry)

CShM parameter is 0 for the ideal geometry and increases when distortion from the ideal polyhedron increase.

Table 2-4. Results of Continuous Shape Measure of Metal Ions in Compounds.

(a) Nb^{4+} ions. (b) Mn^{2+} Ions (Continued).

(b)

Mn^{2+} ions		CShM parameters		Geometry
		OC-6	TPR-6	
MnNbIpy(+)	RT	0.193	15.409	OC-6
	90 K	0.254	15.252	OC-6
MnNbIpy(−)	RT	0.242	14.843	OC-6
	90 K	0.241	15.252	OC-6
MnNbBrpy(+)	RT	0.368	15.430	OC-6
	90 K	0.401	15.242	OC-6
MnNbBrpy(−)	RT	0.328	15.535	OC-6
	90 K	0.409	15.294	OC-6
MnNbClpy	RT	0.216	16.681	OC-6
	90 K	0.218	16.643	OC-6

CShM parameters.

OC-6 = the parameter related to the octahedron (Oh symmetry)

TPR-6 = the parameter related to the trigonal prism (D3h symmetry)

CShM parameter is 0 for the ideal geometry and increases when distortion from the ideal polyhedron increase.

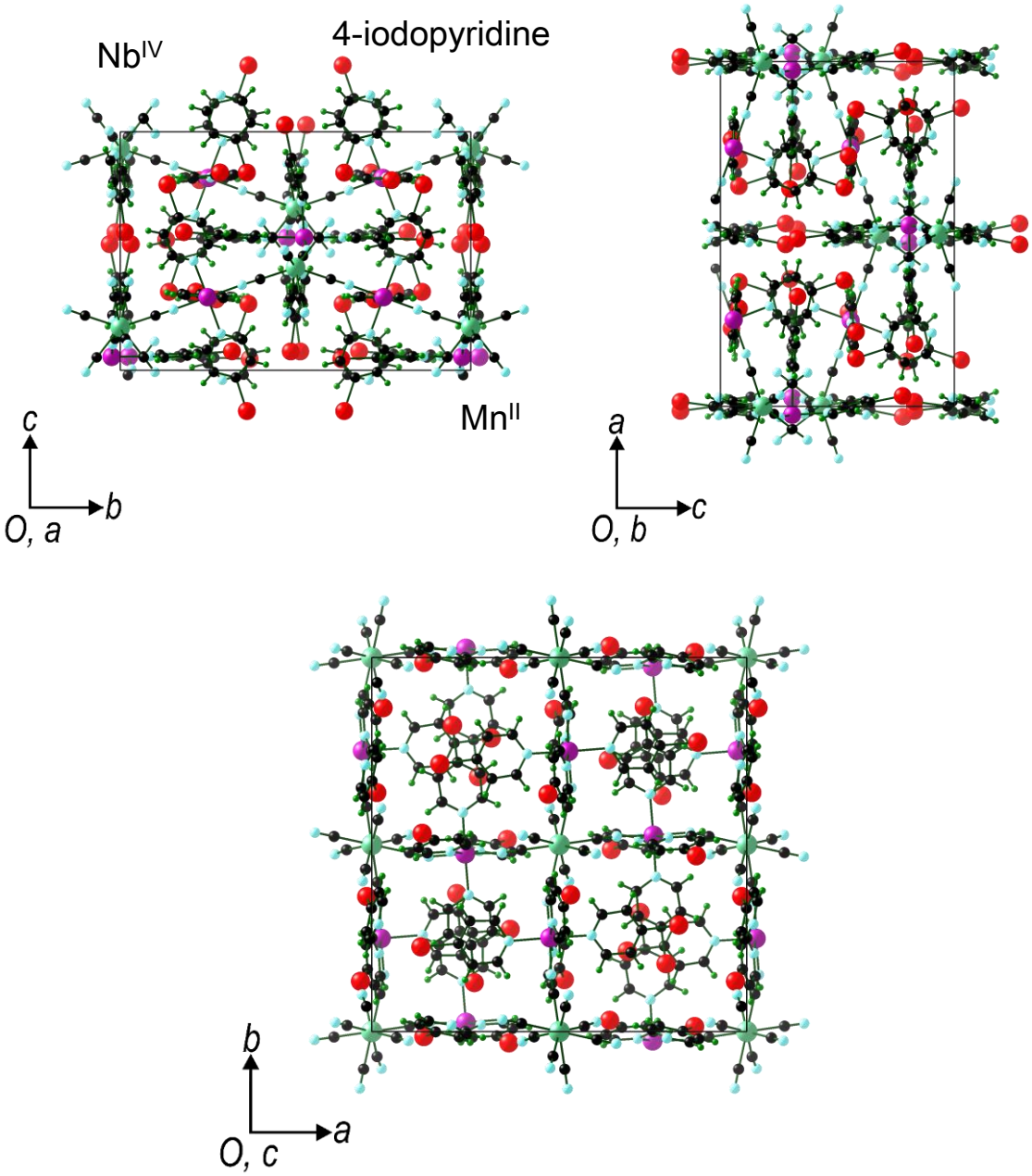

Figure 2-2. Views of crystal structure (measured on 90 K) of $[Mn(4\text{-iodopyridine})_4]_2[Nb(CN)_8]$ (**MnNbIpy**). Black, dark green, blue, green, red, purple, light blue, and turquoise green spheres represent C, H, Br, Cl, I, Mn, and N atoms respectively.

Adapted from Ref. [151] with permission from the Royal Society of Chemistry.

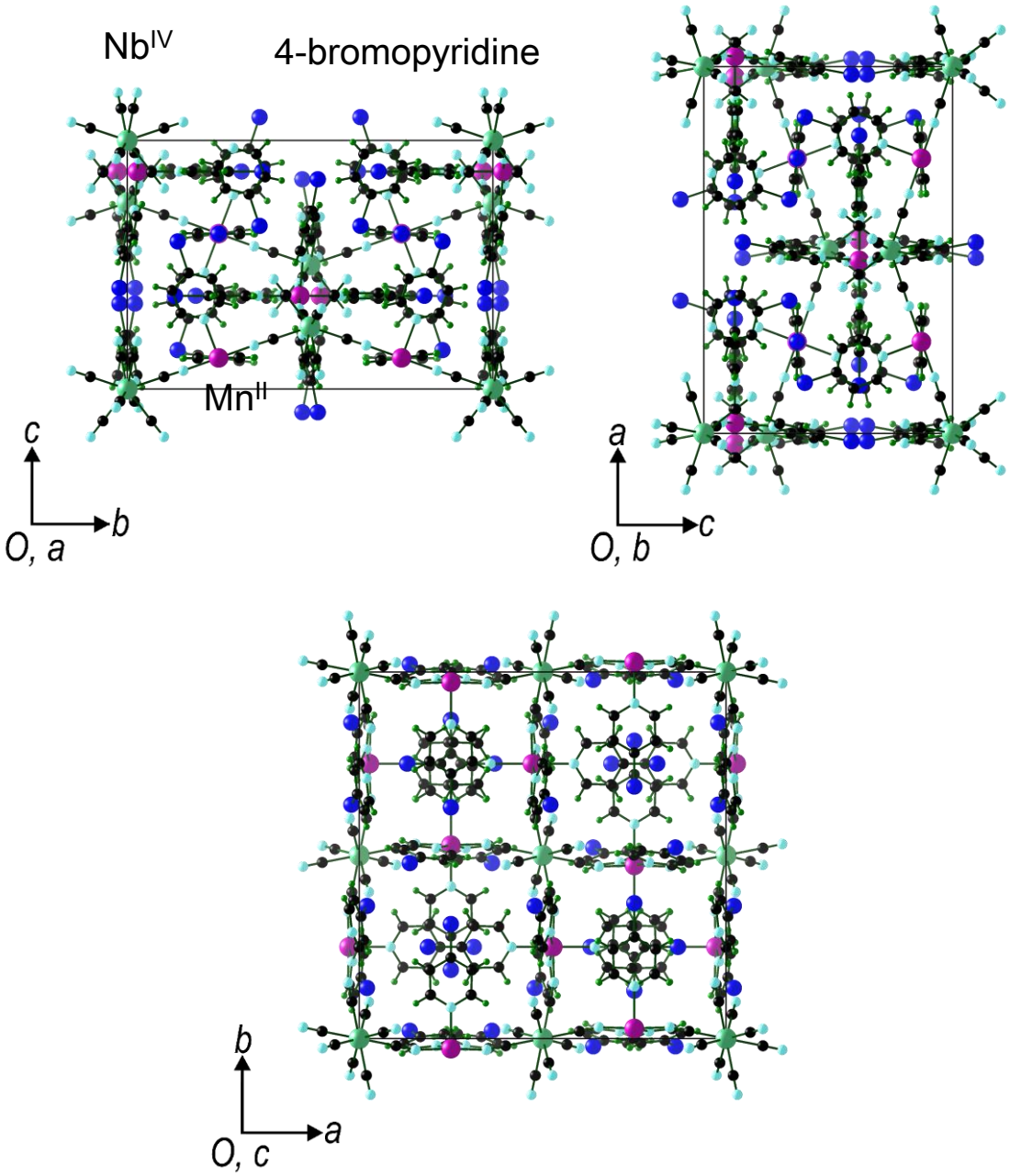

Figure 2-3. Views of crystal structure (measured on 90 K) of $[Mn(4\text{-bromopyridine})_4]_2[Nb(CN)_8]\cdot 0.5H_2O$ (**MnNbBrpy**). Black, dark green, blue, green, red, purple, light blue, and turquoise green spheres represent C, H, Br, Cl, I, Mn, and N atoms respectively.

Modified and reprinted with permission from T. Ohno, S. Chorazy, K. Imoto, S. Ohkoshi, *Cryst. Growth Des.*, 2016, **16**, 4119. Copyright 2016 American Chemical Society.

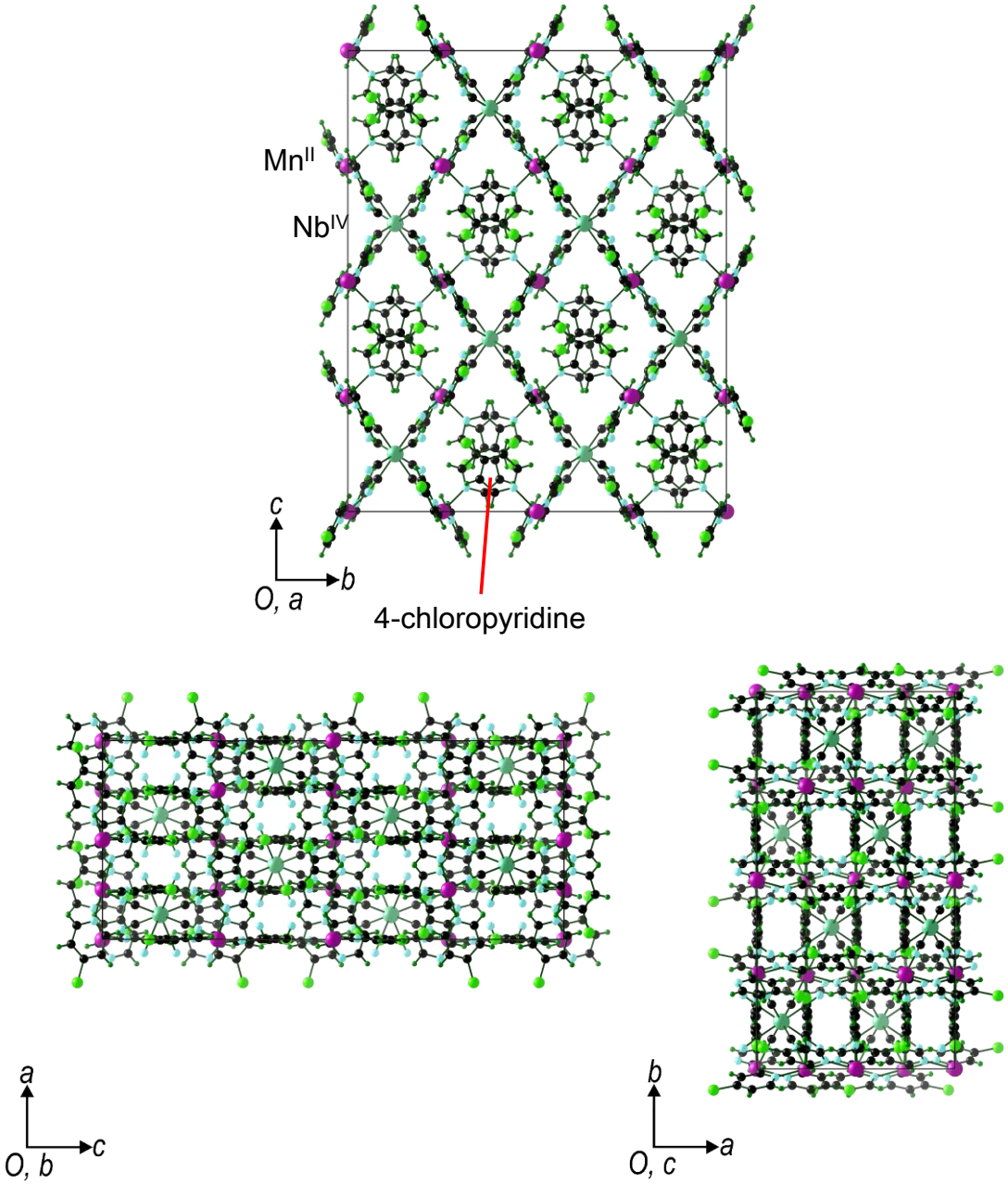

Figure 2-4. Views of crystal structure (measured on 90 K) of $[Mn(4\text{-chloropyridine})_4]_2[Nb(CN)_8]\cdot 0.5H_2O$ (**MnNbClpy**). Black, dark green, blue, green, red, purple, light blue, and turquoise green spheres represent C, H, Br, Cl, I, Mn, and N atoms respectively.

Adapted from Ref. [151] with permission from the Royal Society of Chemistry.

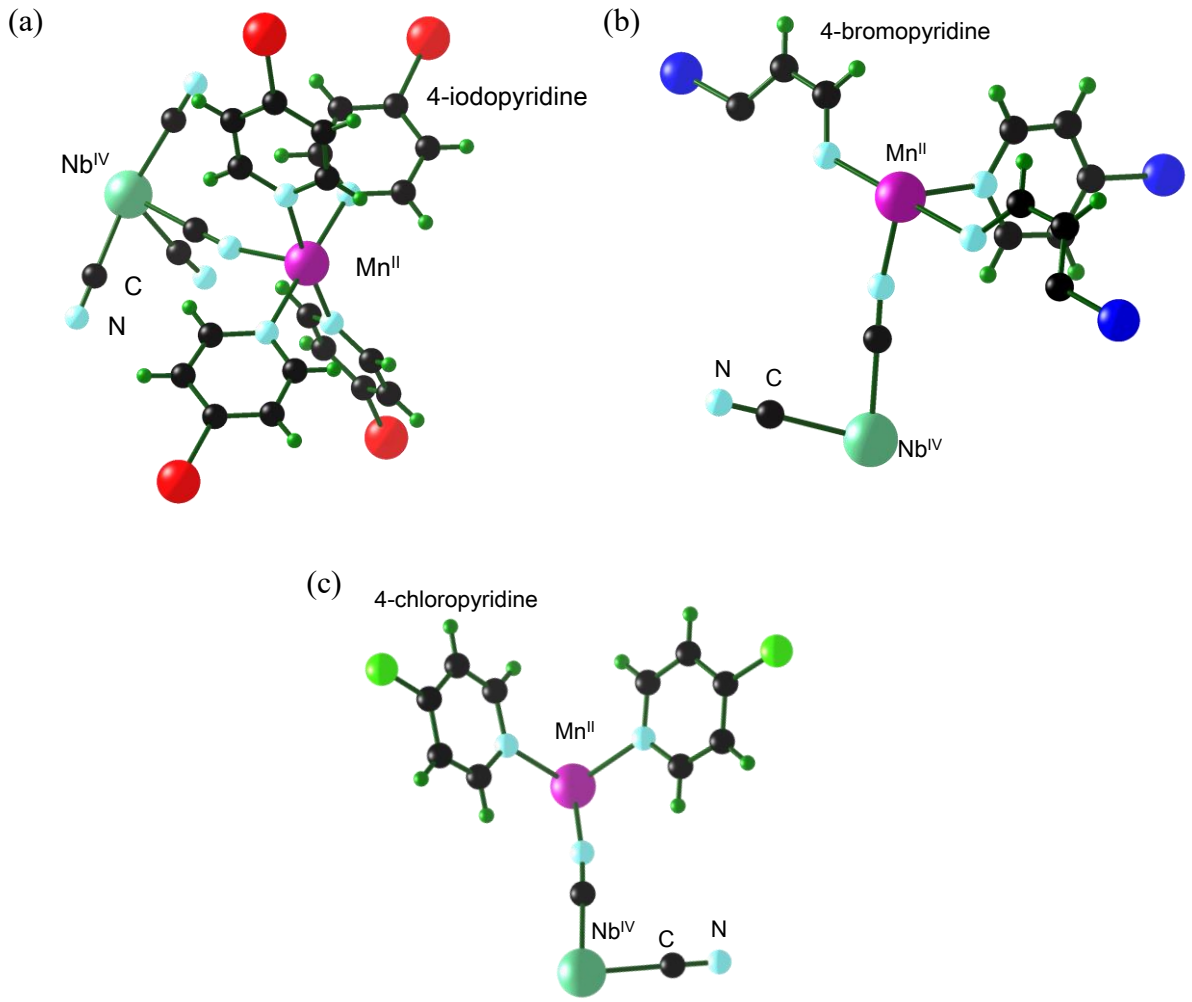

Figure 2-5. Views of asymmetric unit (measured on 90 K) of (a) $[Mn(4\text{-iodopyridine})_4]_2[Nb(CN)_8]$, (b) $[Mn(4\text{-bromopyridine})_4]_2[Nb(CN)_8]\cdot 0.5H_2O$, and (c) $[Mn(4\text{-chloropyridine})_4]_2[Nb(CN)_8]\cdot 0.5H_2O$. Black, dark green, blue, green, red, purple, light blue, and turquoise green spheres represent C, H, Br, Cl, I, Mn, and N atoms respectively.

Adapted from Ref. [151] with permission from the Royal Society of Chemistry.

Modified and reprinted with permission from T. Ohno, S. Chorazy, K. Imoto, S. Ohkoshi, *Cryst. Growth Des.*, 2016, **16**, 4119. Copyright 2016 American Chemical Society.

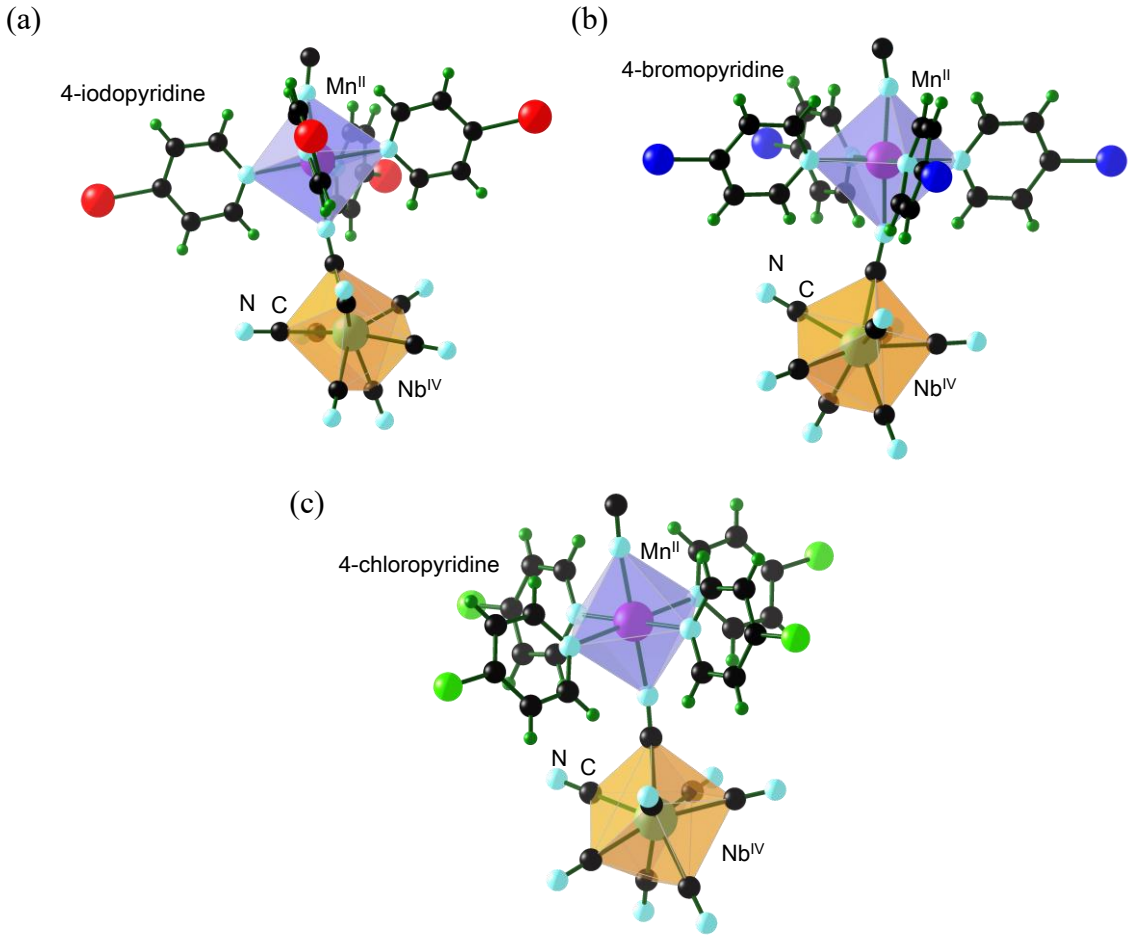

Figure 2-6. Views of coordination geometry (measured on 90 K) of (a) $[Mn(4\text{-iodopyridine})_4]_2[Nb(CN)_8]$, (b) $[Mn(4\text{-bromopyridine})_4]_2[Nb(CN)_8]\cdot 0.5H_2O$, and (c) $[Mn(4\text{-chloropyridine})_4]_2[Nb(CN)_8]\cdot 0.5H_2O$. Black, dark green, blue, green, red, purple, light blue, and turquoise green spheres represent C, H, Br, Cl, I, Mn, and N atoms respectively.

Adapted from Ref. [151] with permission from the Royal Society of Chemistry.

Modified and reprinted with permission from T. Ohno, S. Chorazy, K. Imoto, S. Ohkoshi, *Cryst. Growth Des.*, 2016, **16**, 4119. Copyright 2016 American Chemical Society.

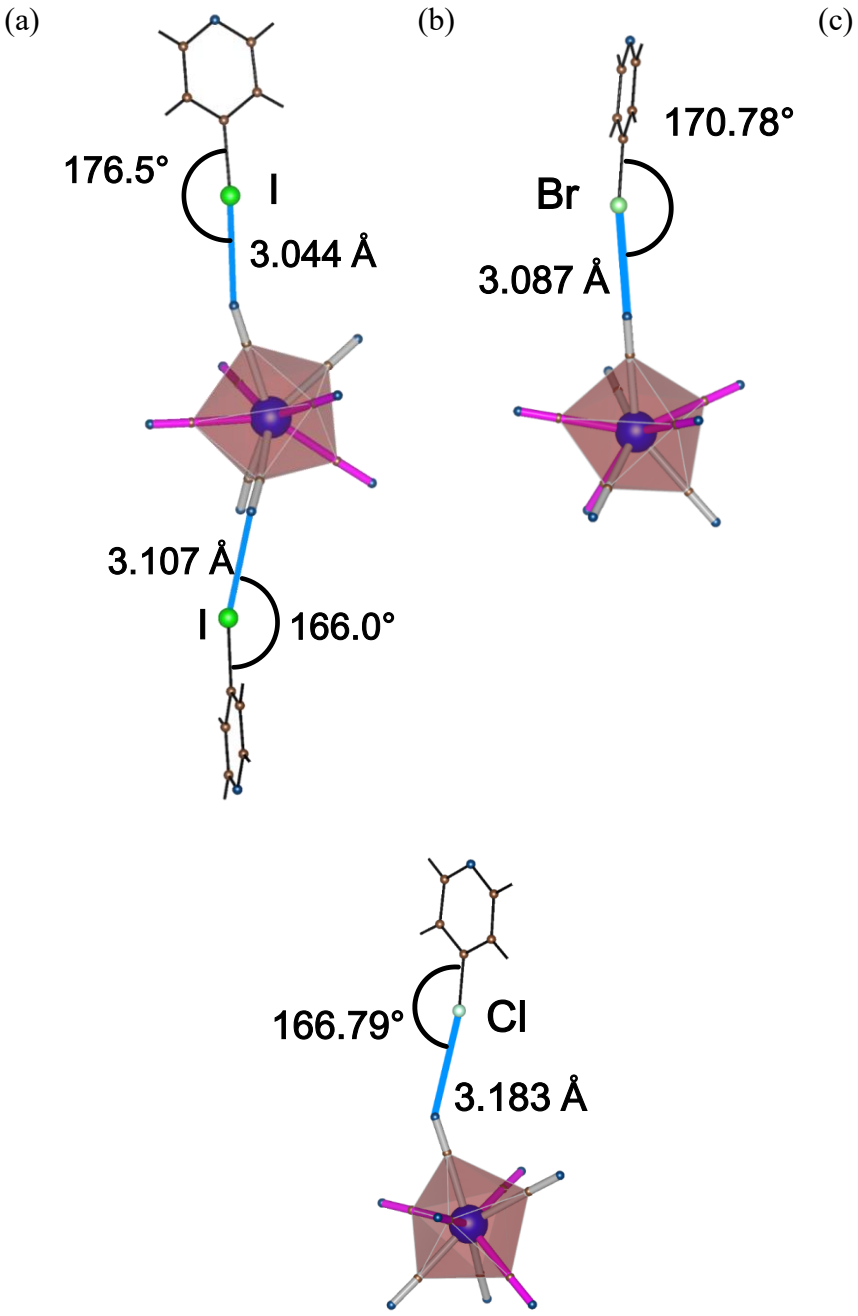

Figure 2-7. Detailed view of the halogen bonding of (a) **MnNbIpy(+)**, (b) **MnNbBrpy(+)**, and **MnNbClpy** at 90 K.

Adapted from Ref. [151] with permission from the Royal Society of Chemistry.

Modified and reprinted with permission from T. Ohno, S. Chorazy, K. Imoto, S. Ohkoshi, *Cryst. Growth Des.*, 2016, **16**, 4119. Copyright 2016 American Chemical Society.

(a)

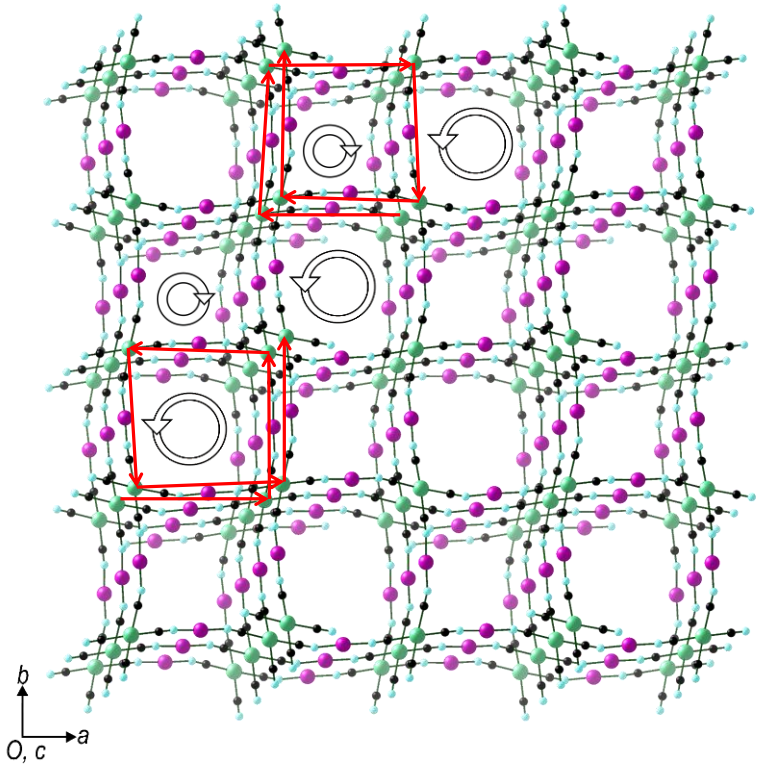

(b)

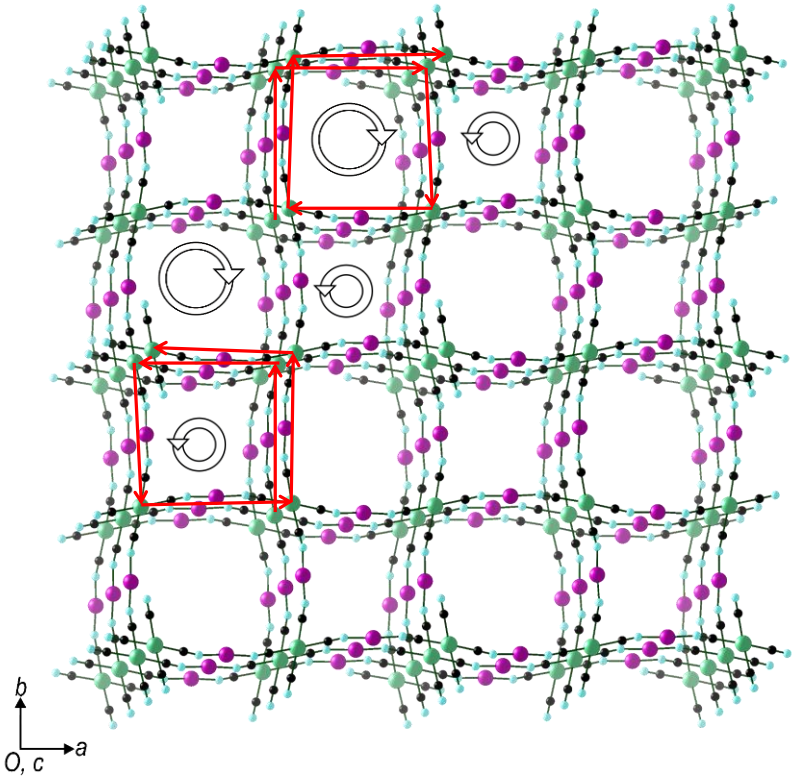

(c)

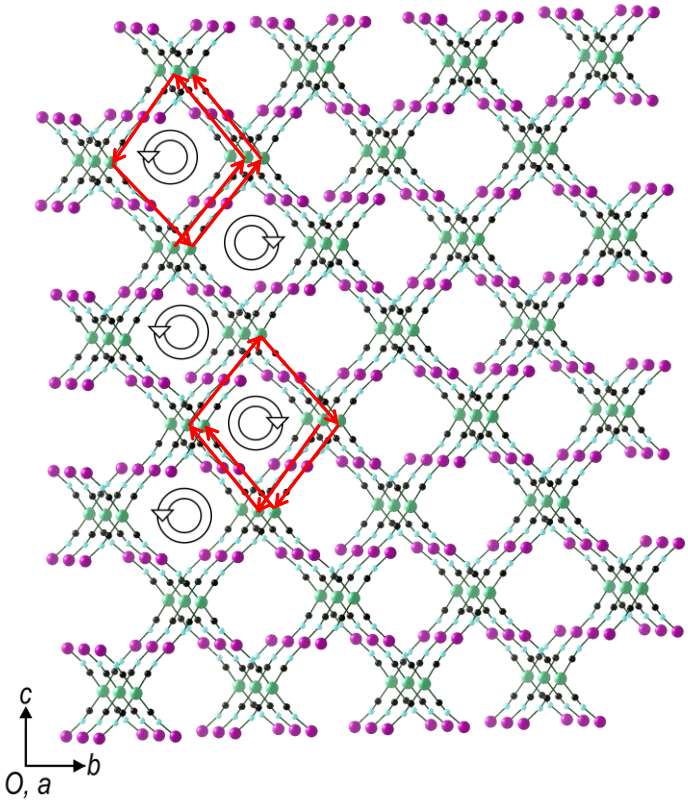

Figure 2-8. Structural views of 3D coordination networks without 4-halopyridine and terminal cyanido ligands and schematic views of helical structure for (a) **MnNbIpy**, (b) **MnNbBrpy**, and (c) **MnNbClpy**.

Adapted from Ref. [151] with permission from the Royal Society of Chemistry.

Modified and reprinted with permission from T. Ohno, S. Chorazy, K. Imoto, S. Ohkoshi, *Cryst. Growth Des.*, 2016, **16**, 4119. Copyright 2016 American Chemical Society.

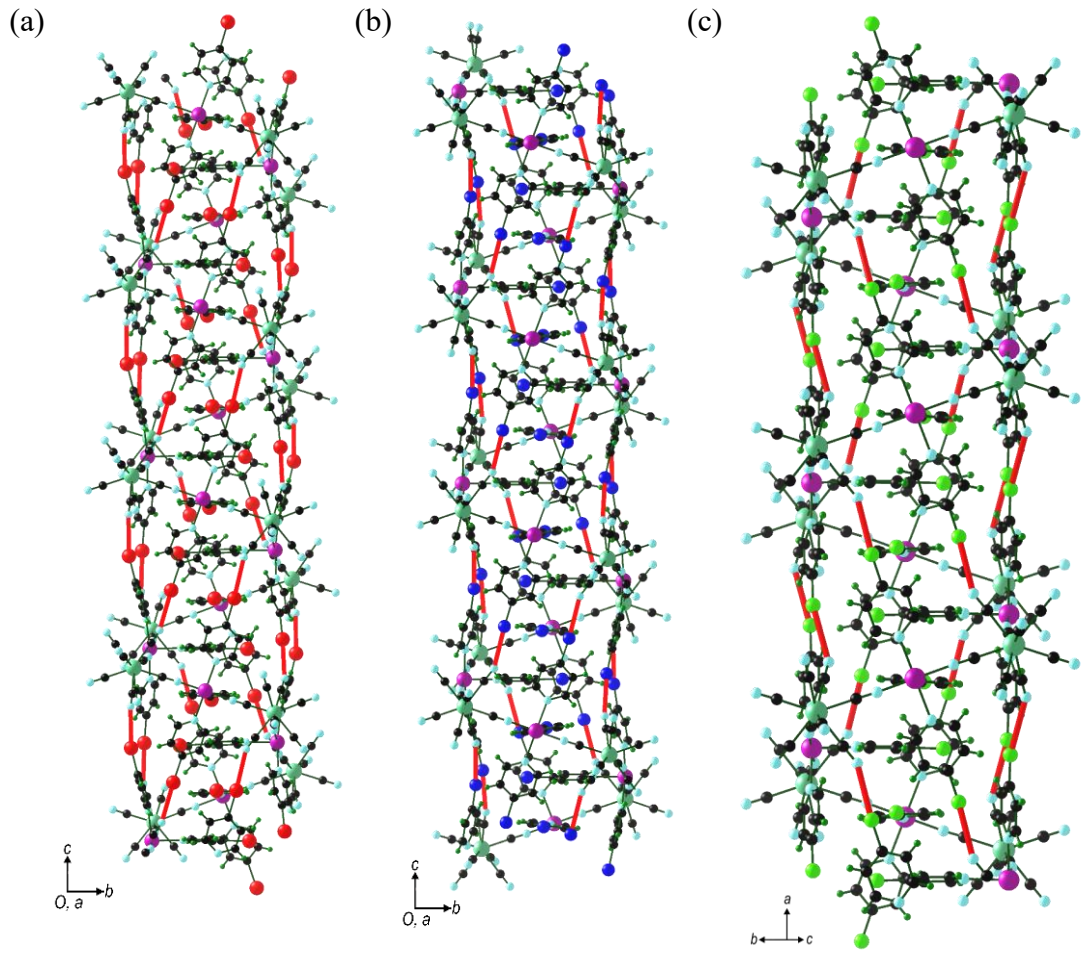

Figure 2-9. Details of helical structure and halogen bonding. (a) **MnNbIpy**, (b) **MnNbBrpy**, and (c) **MnNbClpy**.

Adapted from Ref. [151] with permission from the Royal Society of Chemistry.

Modified and reprinted with permission from T. Ohno, S. Chorazy, K. Imoto, S. Ohkoshi, *Cryst. Growth Des.*, 2016, **16**, 4119. Copyright 2016 American Chemical Society.

(a)

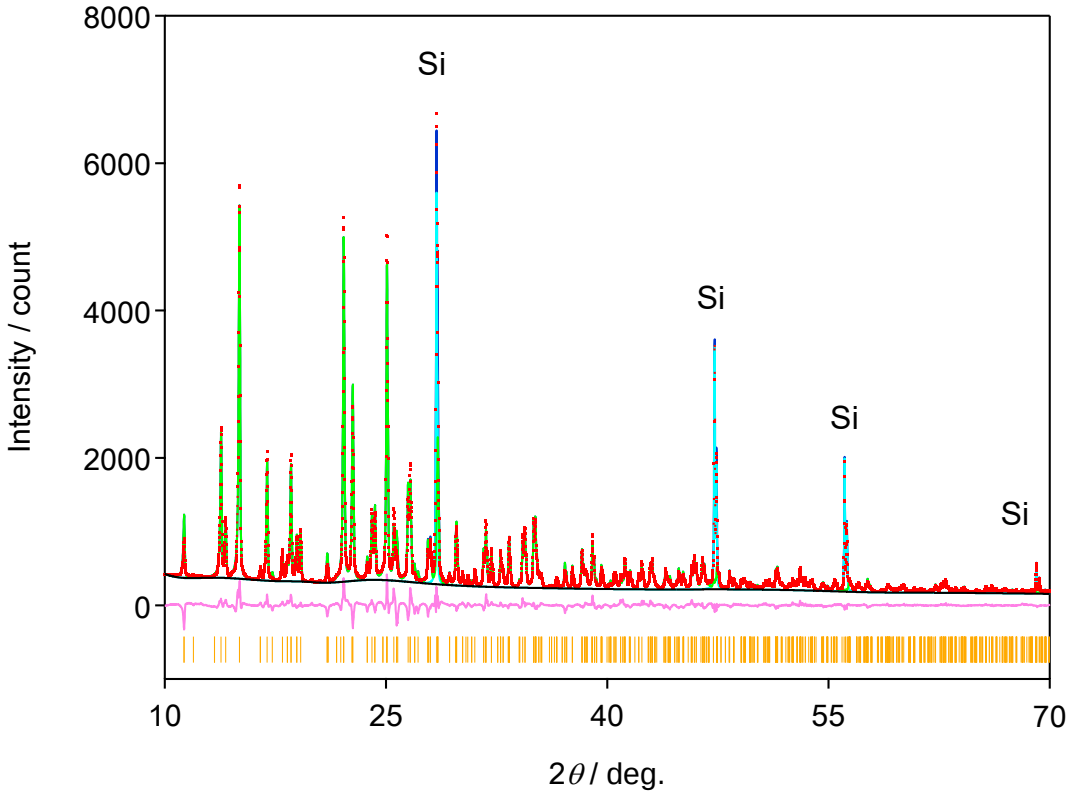
8000
6000
4000
2000
0
Intensity / count
Si
Si
Si
Si
10
25
40
55
70
2θ / deg.

(b)

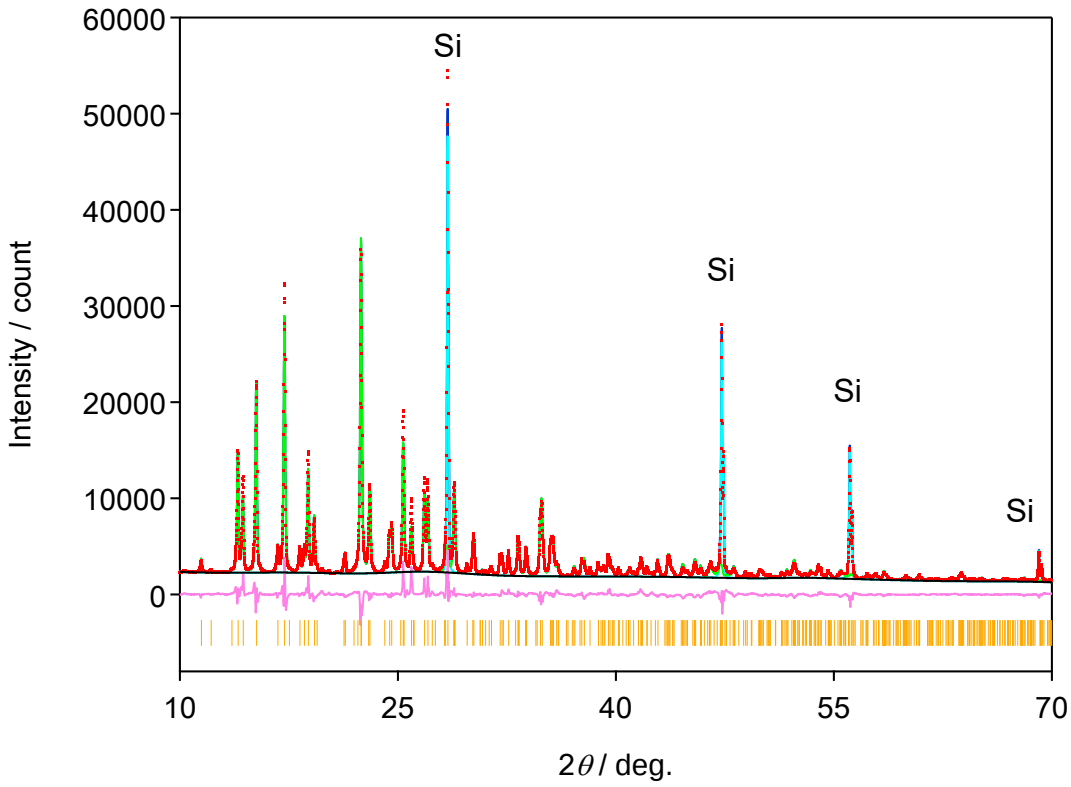
60000
50000
40000
30000
20000
10000
0
Intensity / count
Si
Si
Si
Si
10
25
40
55
70
2θ / deg.

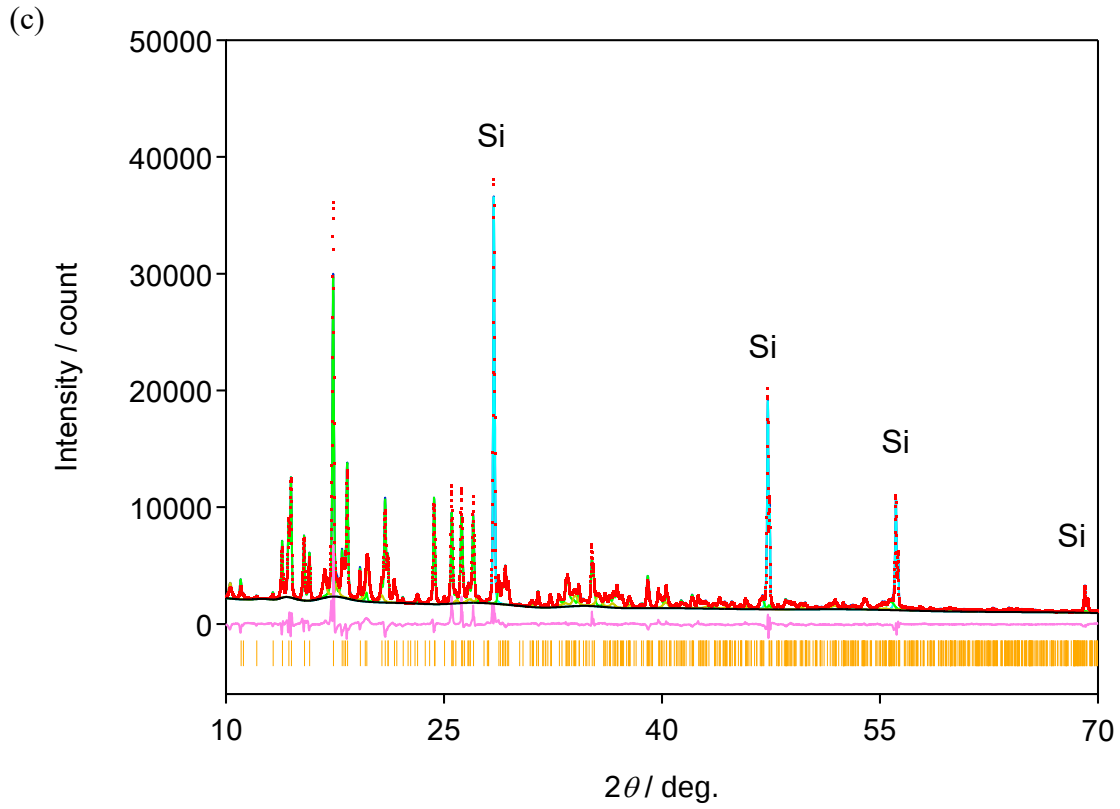

Figure 2-10. PXRD patterns and Rietveld analysis of (a) **MnNbIpy**, (b) **MnNbBrpy**, and (c) **MnNbClpy**. Red dots, blue lines, light green lines, cyan lines, yellow lines, black lines, orange bars, and pink lines show the observed patterns, the calculated patterns, the pattern of the compounds, the pattern of Si angle standard, the pattern of impurity, the calculated background, the calculated positions of Bragg reflections, and the difference of observed and calculated ones, respectively.

Adapted from Ref. [151] with permission from the Royal Society of Chemistry.

Modified and reprinted with permission from T. Ohno, S. Chorazy, K. Imoto, S. Ohkoshi, *Cryst. Growth Des.*, 2016, **16**, 4119. Copyright 2016 American Chemical Society.

(a)

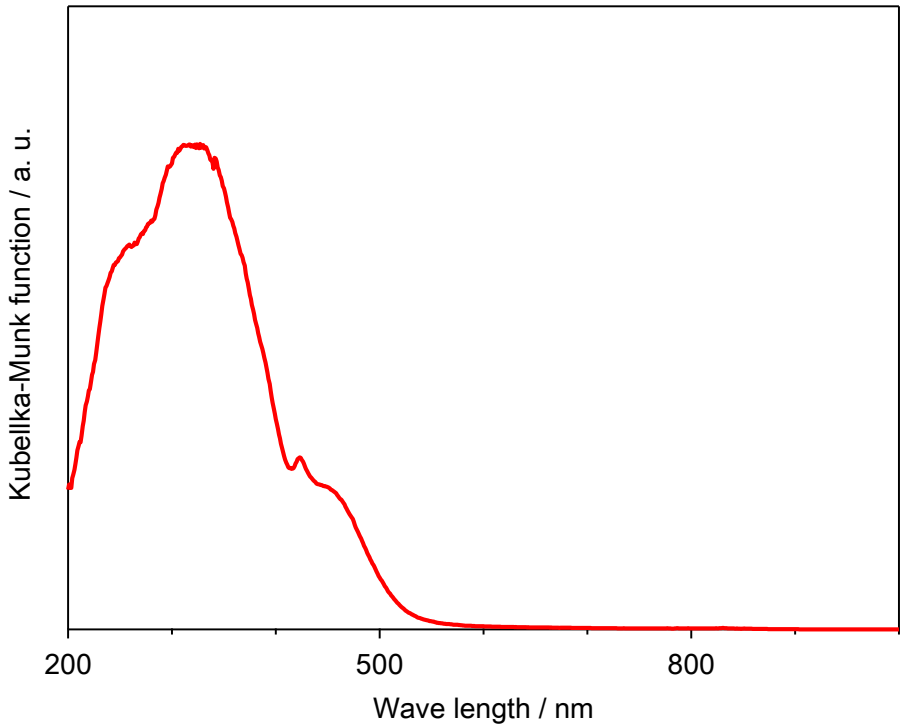
Kubellka-Munk function / a. u.
200
500
800
Wave length / nm

(b)

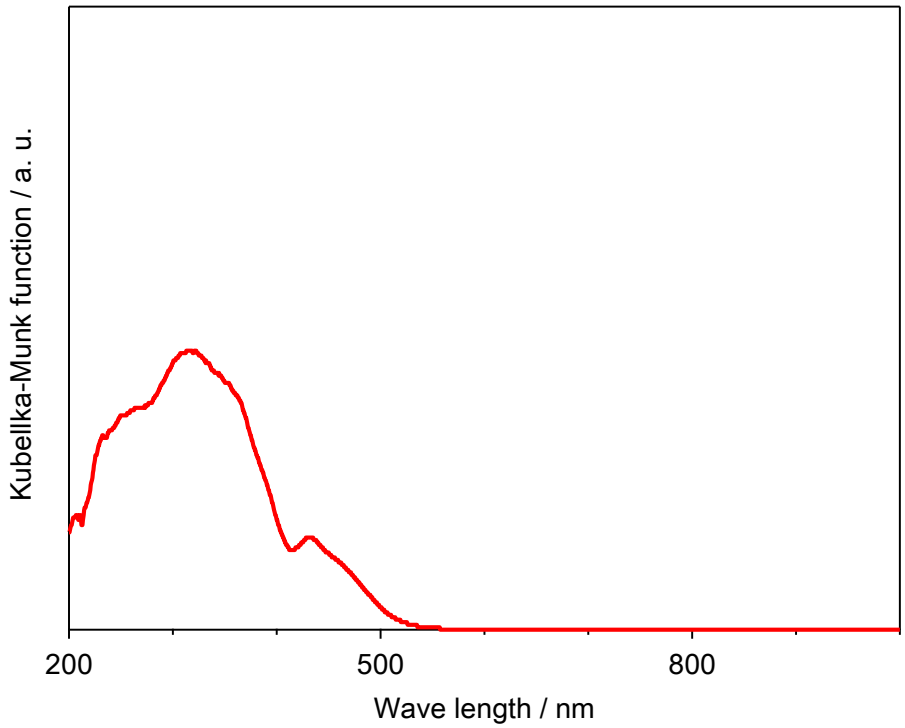
Kubellka-Munk function / a. u.
200
500
800
Wave length / nm

(c)

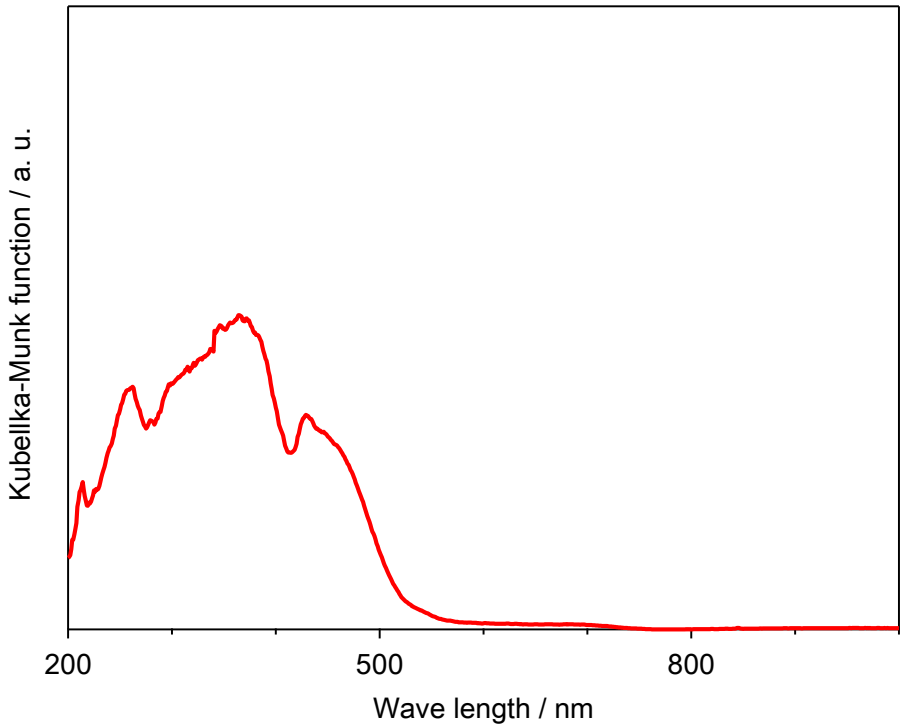

Figure 2-11. UV-Vis reflectance spectra of (a) **MnNbIpy**, (b) **MnNbBrpy**, and (c) **MnNbClpy**.

Adapted from Ref. [151] with permission from the Royal Society of Chemistry.

Modified and reprinted with permission from T. Ohno, S. Chorazy, K. Imoto, S. Ohkoshi, *Cryst. Growth Des.*, 2016, **16**, 4119. Copyright 2016 American Chemical Society.

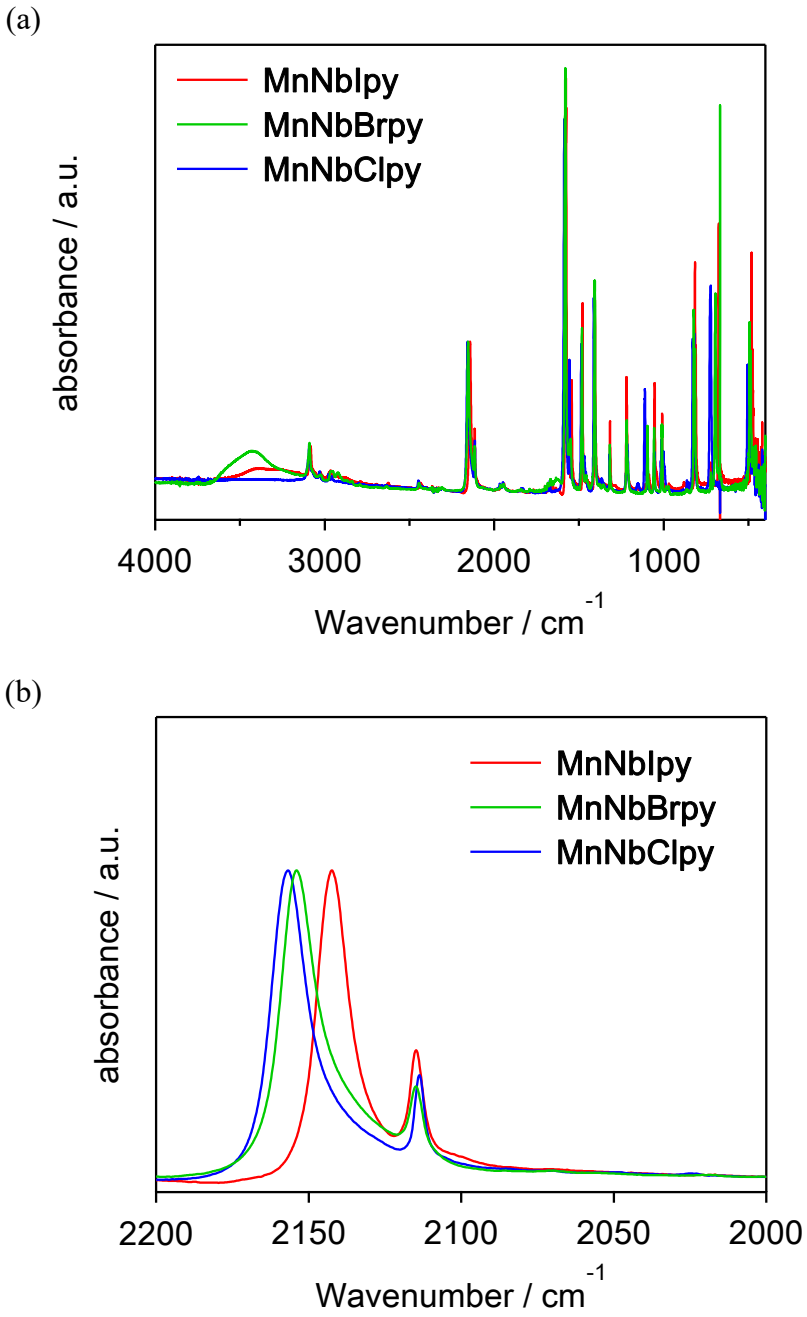

Figure 2-12. IR absorption spectra of (a) overall view, and (b) enlarged view of CN stretching region.

Adapted from Ref. [151] with permission from the Royal Society of Chemistry.

Modified and reprinted with permission from T. Ohno, S. Chorazy, K. Imoto, S. Ohkoshi, *Cryst. Growth Des.*, 2016, **16**, 4119. Copyright 2016 American Chemical Society.

Chapter 3: Magnetic Properties of Mn^{II}–Nb^{IV} Cyanido Bridged Bimetal Assemblies

3.1 Introduction

In chapter 2, Mn–Nb–4-halopyridine complexes with chiral 3-D network structures have been introduced. The results of spectroscopic studies and elemental analyses confirmed the chemical formulae of $[Mn(4\text{-halopyridine})]_2[Nb(CN)_8]\cdot zH_2O$. Such 3-D cyanido-bridged Mn–Nb assemblies have a possibility to show ferromagnetism. Herein, magnetic properties of **MnNbIpy**, **MnNbBrpy**, and **MnNbClpy** are discussed based on results of magnetic measurements.

3.2 Experimental Details

Magnetic property measurements were conducted by using Quantum Design magnetic properties measurement system (MPMS) equipped with superconducting quantum interference device magnetometers (SQUID). Measurement samples were prepared from the powder samples of **MnNbIpy**, **MnNbBrpy**, and **MnNbClpy**. The powder samples were put into the capsules and then glass cottons were introduced to the capsules for the powder samples not to move. The capsules are hanged on the middle of plastic straws and they are used to the measurements.

The magnetizations were measured on the 1 $K\cdot min^{-1}$ rate on external magnetic field (H_{ext}) of 1000 Oe from 300 K to 2 K and then from 2 K to 300 K. After decreasing the temperature to 2 K with no external magnetic field the zero-field-cooled magnetization (zFCM) curves were measured on the 1 $K\cdot min^{-1}$ rate from 2 K to 60 K with the H_{ext} value of 10 Oe. The field cooled magnetization (FCM) curves were measured on the 1 $K\cdot min^{-1}$ rate from 60 K to 2 K with the H_{ext} value of 10 Oe. After the FCM measurements, the external magnetic fields were set to 0 Oe and then the remnant magnetization curves (RM) were measured on the 1 $K\cdot min^{-1}$ rate from 2 K to 60 K. The magnetization (M) vs H_{ext} plots (M–H plots) measurements were conducted

at 2 K by changing the H_{ext} value from 0 Oe to 50000 Oe, from 50000 Oe to −50000 Oe, and then from −50000 Oe to 50000 Oe. The diamagnetic contribution from compounds are estimated by Pascal's constant and then subtracted from experimental data.

3.3 Result and Disucussion

3.3.1 Magnetization of MnNbIpy

The plot of the product ($\chi_M T$) of the magnetic susceptibility (χ_M) and the temperature (T) vs the temperature (T) under H_{ext} of 1000 Oe ($\chi_M T$–T plot) are shown in Figure 3-1a. The $\chi_M T$ value is 8.7 $cm^3 \cdot mol^{-1} \cdot K$ at 300 K, and increases gradually with decreasing temperature. Under 100 K, the $\chi_M T$ value shows abrupt increase to reaching the maximum of 503 $cm^3 \cdot mol^{-1} \cdot K$ at 17 K, and then drops to 92 $cm^3 \cdot mol^{-1} \cdot K$ at 2 K. The $\chi_M T$ value at 300 K is corresponding to the calculated spin only value of 9.1 $cm^3 \cdot mol^{-1} \cdot K$, which is estimated considering the non-interacting $\{Mn^{II}_{HS\ 2}Nb^{IV}_{1}\}$ unit (g_{Mn} = 2.0, S_{Mn} = 5/2, g_{Nb} = 2.0, and S_{Nb} = 1/2). An antiferromagnetic interaction between Mn^{II}_{HS} and Nb^{IV}, which will be discussed later, is probably a reason for the lower observed value of $\chi_M T$ compared to the calculated spin-only $\chi_M T$ value, and the overall behavior of the $\chi_M T$–T plot is typical to ferrimagnet.

The FCM, the RM, and the zFCM curves are shown in Figure 3-2. The drastic changes on FCM and zFCM plots at 22 K indicate **MnNbIpy** shows long range long range magnetic ordering under the Curie temperature (T_C) of 22 K. The magnetization (M) vs external magnetic field (H_{ext}) plot at 2 K (M–H plot, Figure 3-1b) shows the abrupt increase of the magnetization and the saturation around the H_{ext} = 3000 Oe. The saturation magnetization (M_S) value is 9.0 μ_B. The M–H plot has almost no magnetic coercive field (H_c). Considering that the calculated M_S values for the $\{Mn^{II}_{HS\ 2}Nb^{IV}_{1}\}$ unit (g_{Mn} = 2.0, S_{Mn} = 5/2, g_{Nb} = 2.0, and S_{Nb} = 1/2) are 9.0 μ_B (assuming ferrimagnetic ordering) or 11.0 μ_B (assuming ferromagnetic ordering), **MnNbIpy** is a ferrimagnet, where the magnetic moments of Mn^{2+} and Nb^{4+} ions order antiparallelly under the T_C.

The average value of the superexchange interaction between Nb^{IV} and Mn^{II}_{HS} can be estimated by employing mean field theory.[5,6,134] Assuming that the superexchange interaction of metal site *i* and *j* (J_{ij}) are represented as the Hamiltonian equation $H = -J_{ij}\,\hat{S}_i\hat{S}_j$ ($\hat{S}_i$ and $\hat{S}_j$ stand for the spin values of metal sites, *i* and *j*, respectively), the T_C is calculated as follows:

$$T_C = \frac{|J_{MnNb}|\sqrt{S_{Mn}(S_{Mn}+1)S_{Nb}(S_{Nb}+1)Z_{Mn}Z_{Nb}}}{3k_B} \quad (3\text{-}1)$$

where Z_i (i = Mn, Nb) are numbers of nearest neighbor magnetic ions of ion *i*, S_i (i = Mn, Nb) are spin quantum numbers of ion *i*, and k_B is the Boltzmann constant (0.695 $cm^{-1}\cdot K^{-1}$). With substituting the parameters of this compound (T_C = 22 K, Z_{Mn} = 2, Z_{Nb} = 4, S_{Mn} = 5/2, S_{Nb} = 1/2), the resulted value, J_{MnNb} = −6.4 cm^{-1}, is obtained (minus sign from antiferromagnetic interaction), which is comparable with values from compounds based on octahedral Mn^{II}_{HS} and square antiprism Nb^{IV} ions (Table 3-1).

Compared to the magnetisms of **MnNbBrpy** and **MnNbClpy** (the T_C values are 28 K) which will be discussed later, **MnNbIpy** shows relatively low T_C (22 K). The superexchange interaction between Mn^{II}_{HS} and $[Nb^{IV}(CN)_8]$ are affected by geometry of $[Nb^{IV}(CN)_8]$.[22,136,147–149] However, these three compounds show the same coordination geometries (distorted square antiprism) of $[Nb^{IV}(CN)_8]$. **MnNbIpy** shows longer distance and weaker bonding between CN and Mn (the Mn–N(CN) distances are 2.168(15) and 2.192(13) Å in **MnNbIpy(+)**, 2.125(4) in **MnNbBrpy(+)**, 2.115(3) Å in **MnNbClpy** at room temperature) and this should be the reason of relatively weaker magnetic superexchange interaction of **MnNbIpy**. This difference in the CN–Mn bond is also depicted in IR spectra section.

3.3.2 Magnetization of MnNbBrpy

The magnetic properties of **MnNbBrpy** are shown in Figure 3-3 and 3-4. The $\chi_M T$–T plot under H_{ext} of 1000 Oe depicts that the $\chi_M T$ value at 300 K is 8.5 $cm^3\cdot mol^{-1}\cdot K$, increases with decreasing the temperature to reach the maximum of 639 $cm^3\cdot mol^{-1}\cdot K$ at 21 K, and

decreases to 97 $cm^3 \cdot mol^{-1} \cdot K$ at 2 K. This behavior indicates **MnNbBrpy** has the $\{Mn^{II}_{HS\,2}Nb^{IV}_{1}\}$ unit and shows long range magnetic ordering at low temperature. The FCM, zFCM, and RM curves (Figure 3-4) reveal the long range magnetic ordering with the T_C value of 28 K. The *M–H* plot at 2 K (Figure 3-3a) shows that the M_S value is 9.1 μ_B and the H_c value is less than 100 Oe and this M_S value reveals that **MnNbBrpy** is ferrimagnet. The superexchange interaction value calculated by using eq 3-1 assuming mean field method is –8.1 cm^{-1}. This value is comparable with the values from compounds based on octahedral Mn^{II}_{HS} and square antiprism Nb^{IV} ions (Table 3-1).

3.3.3 Magnetization of MnNbClpy

The magnetic properties of **MnNbClpy** are shown in Figure 3-5 and 3-6. The $\chi_M T$–*T* plot *(H_{ext}* = 1000 Oe) shows that the $\chi_M T$ value at 300 K is 8.6 $cm^3 \cdot mol^{-1} \cdot K$, increases with decreasing the temperature to reach the maximum of 678 $cm^3 \cdot mol^{-1} \cdot K$ at 22 K, and decreases to 92 $cm^3 \cdot mol^{-1} \cdot K$ at 2 K. This behavior indicates **MnNbClpy** has the $\{Mn^{II}_{HS\,2}Nb^{IV}_{1}\}$ unit and shows long range magnetic ordering on low temperature. The FCM, zFCM, and RM curves (Figure 3-6) reveal the long range magnetic ordering with the T_C value of 28 K. The *M–H* plot at 2 K (Figure 3-5b) shows that the M_S value is 9.2 μ_B and that the H_c value is less than 100 Oe. This M_S value reveals that **MnNbClpy** is ferrimagnet. The superexchange interaction value calculated by using eq 3-1 assuming mean field method is $-8.1\ cm^{-1}$. This value is comparable with the values from compounds based on octahedral Mn^{II}_{HS} and square antiprism Nb^{IV} ions (Table 3-1).

3.4 Conclusion

In summary, **MnNbIpy**, **MnNbBrpy**, and **MnNbClpy** show ferrimagnetism where magnetic moments of Mn^{II} ions and Nb^{IV} ions are ordered antiparallelly with the T_C values of 22 K, 28 K, and 28 K, respectively. **MnNbIpy** and **MnNbBrpy** have chiral structure, and therefore, these compounds are proved to be chiral magnets which are expected to show non-linear optical and non-linear magneto-optical effects.

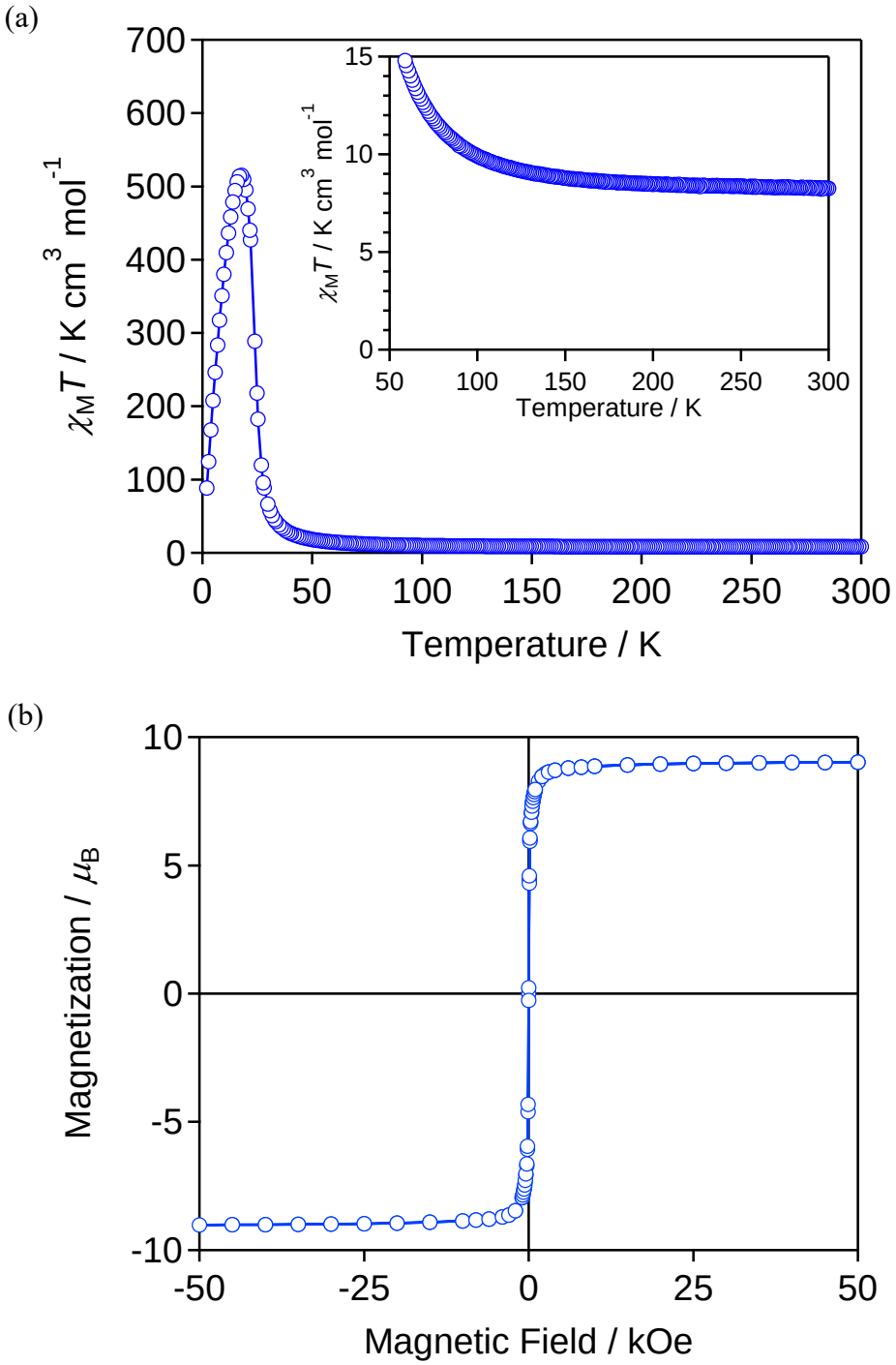

Figure 3-1. Magnetic property measurements of **MnNbIpy**. (a) The $\chi_M T$–T Plot at H_{ex} of 1000 Oe, (inset) enlarged view. (b) The M–H Plot at 2 K.

Adapted from Ref. [151] with permission from the Royal Society of Chemistry.

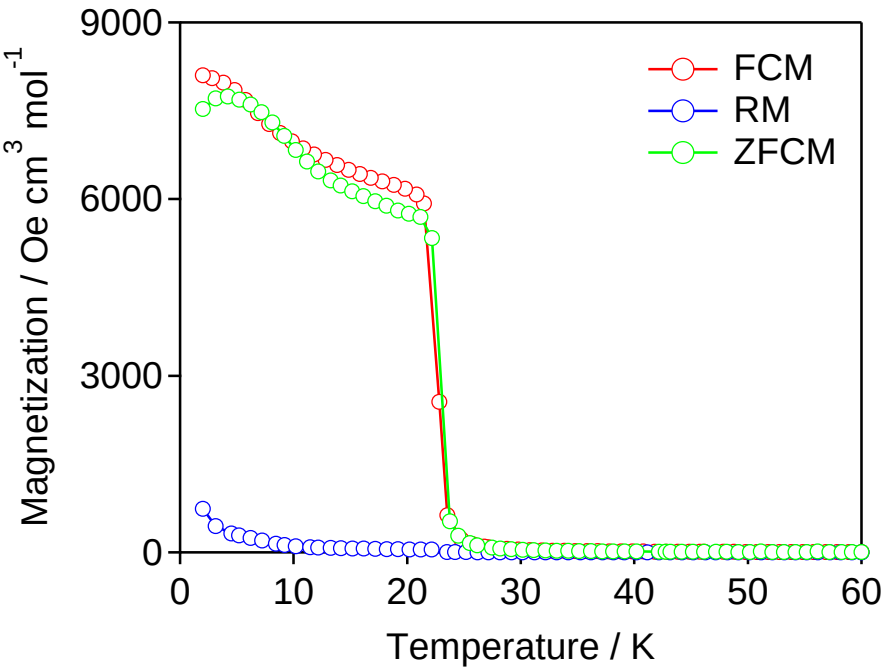

Figure 3-2. Magnetic property measurements of **MnNbIpy**, the FCM curve at H_{ex} of 20 Oe (red solid line), the remnant magnetization curve (blue line), and zero-field FCM curve at H_{ex} of 20 Oe (green).

Adapted from Ref. [151] with permission from the Royal Society of Chemistry.

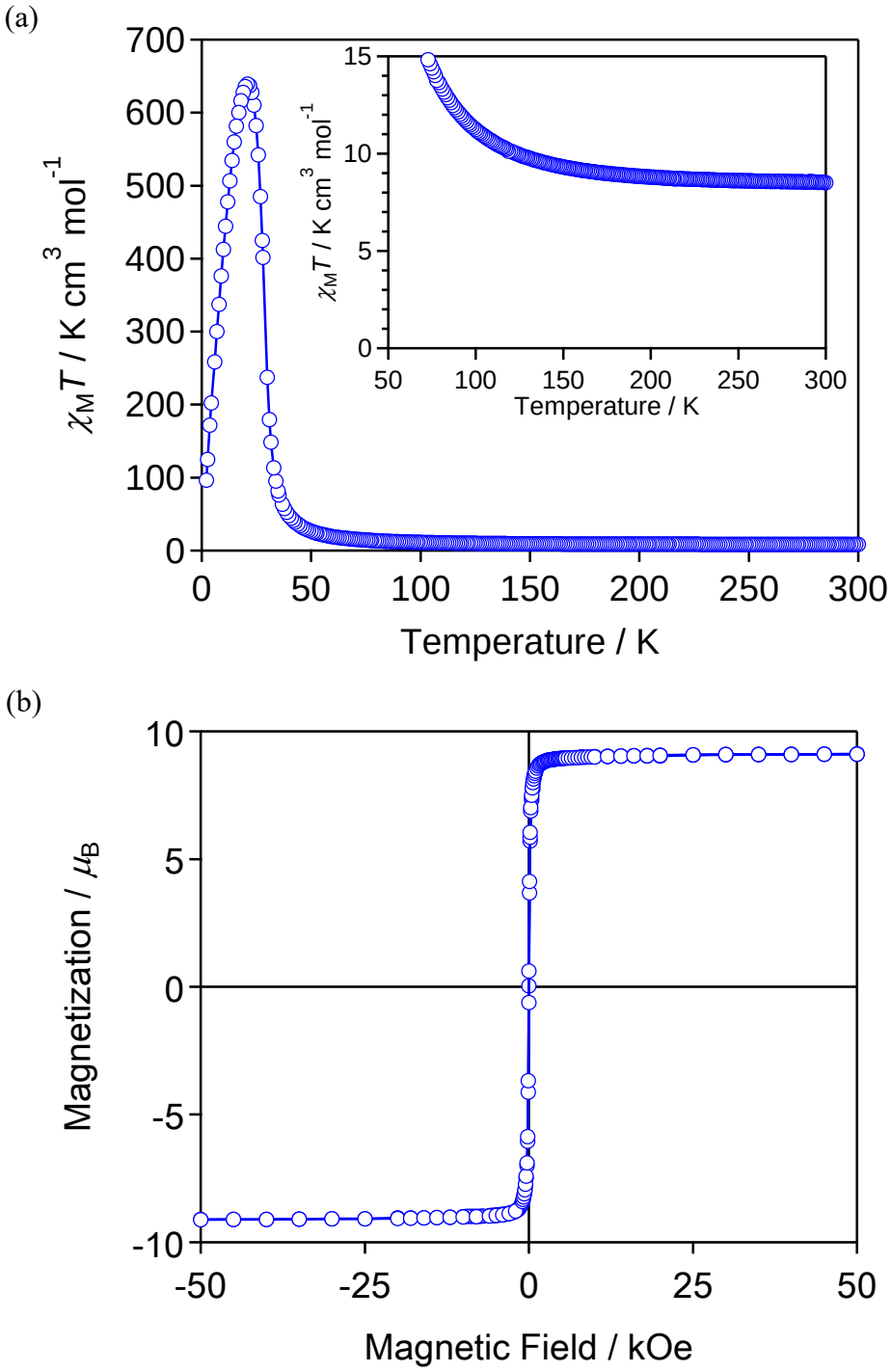

Figure 3-3. Magnetic property measurements of **MnNbBrpy**. (a) The $\chi_M T$–T Plot at H_{ex} of 1000 Oe, (inset) enlarged view. (b) The M–H Plot at 2 K.

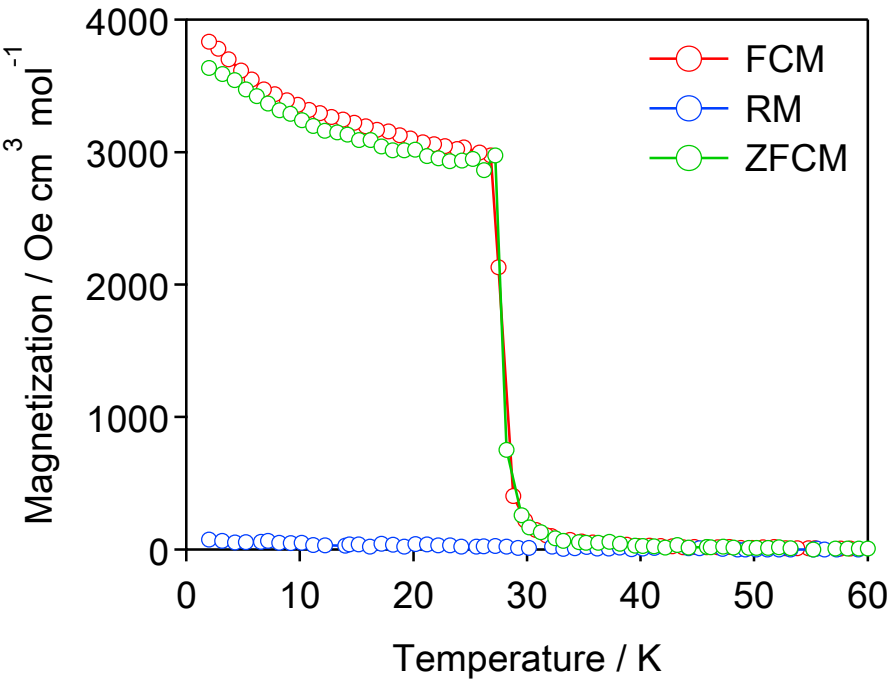

Figure 3-4. Magnetic property measurements of **MnNbBrpy**, the FCM curve at H_{ex} of 20 Oe (red solid line), the remnant magnetization curve (blue line), and zero-field FCM curve at H_{ex} of 20 Oe (green).

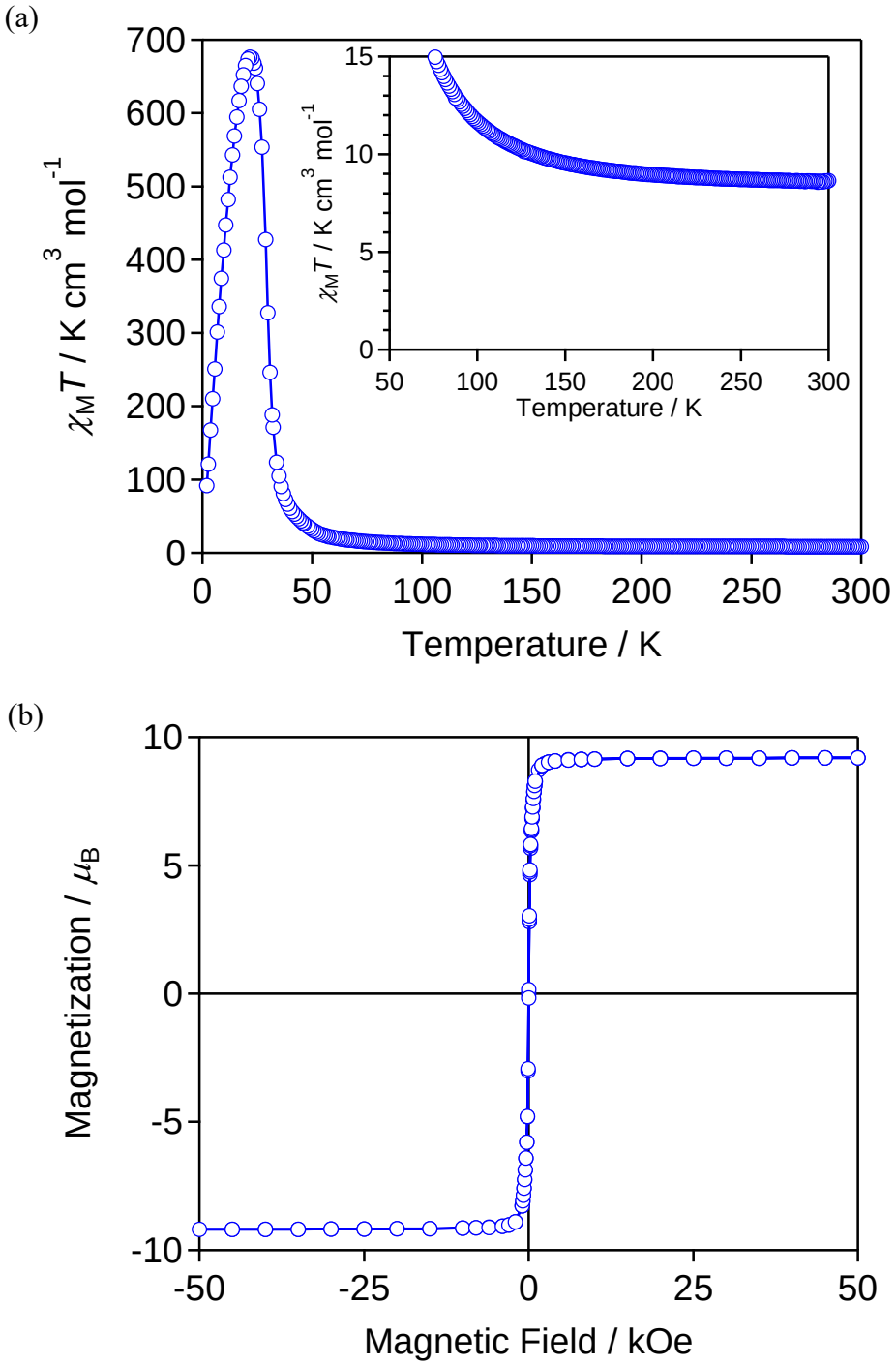

Figure 3-5. Magnetic property measurements of **MnNbClpy**. (a) The $\chi_M T$–T Plot at H_{ex} of 1000 Oe, (inset) enlarged view. (b) The M–H Plot at 2 K.

Adapted from Ref. [151] with permission from the Royal Society of Chemistry.

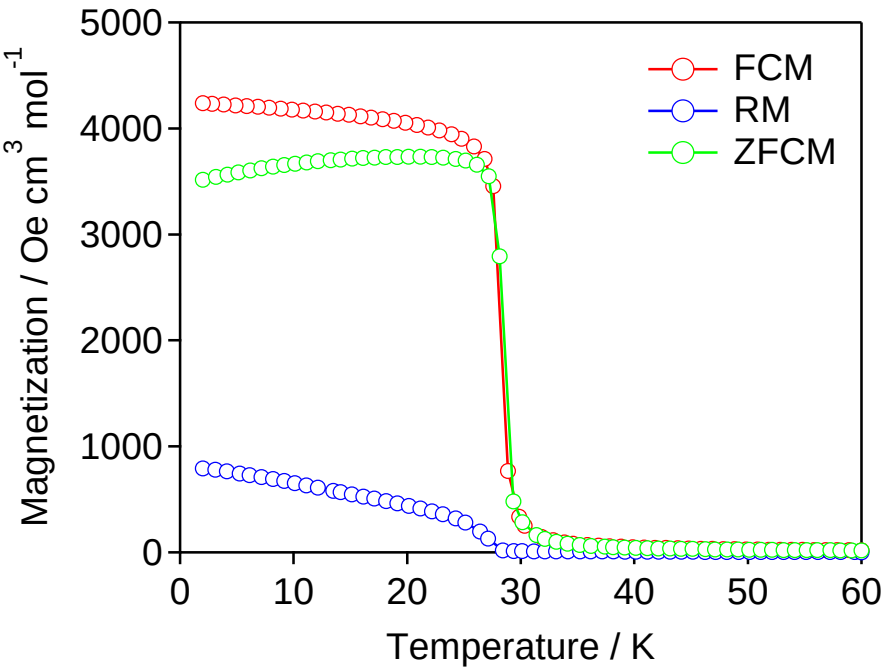

Figure 3-6. Magnetic property measurements of **MnNbClpy**, the FCM curve at H_{ex} of 20 Oe (red solid line), the remnant magnetization curve (blue line), and zero-field FCM curve at H_{ex} of 20 Oe (green).

Adapted from Ref. [151] with permission from the Royal Society of Chemistry.

Table 3-1. Comparison of Magnetic Properties of Magnets with Other Reported $[Nb(CN)_8]$-Based Molecule-Based Magnets.

Compound	Type of Cyanido-Bridged Network	Chirality	Type of Magnetic Ordering	Critical Temperature	Superexchange Interaction*	ref.
$[Ni^{II}(4\text{-bromopyridine})_4]_2[Nb^{IV}(CN)_8]\cdot 2H_2O$	3D	no	ferromagnetism	17 K	9.6 cm^{-1}	[150]
$\{[Ni^{II}(pyrazole)_4]_2[Nb^{IV}(CN)_8]\}\cdot 4H_2O$	3D	no	ferromagnetism	13 K	8.1 cm^{-1}	[135]
$\{[Ni^{II}(cyclam)]_2[Nb^{IV}(CN)_8]\}\cdot 3.5H_2O$ cyclam = 1,4,8,11-tetraazacyclotetradecane	2D	no	ferromagnetism	11.8 K	–	[153]
$[Mn^{II}(4\text{-chloropyridine})_4]_2[Nb^{IV}(CN)_8]\cdot 0.5H_2O$	3D	no	ferrimagnetism	28 K	−8.1 cm^{-1}	[150] [151]
$[Mn^{II}(4\text{-bromopyridine})_4]_2[Nb^{IV}(CN)_8]\cdot 0.5H_2O$	3D	yes	ferrimagnetism	28 K	−8.1 cm^{-1}	[151]
$[Mn^{II}(4\text{-iodopyridine})_4]_2[Nb^{IV}(CN)_8]$	3D	yes	ferrimagnetism	22 K	−6.4 cm^{-1}	[151]
$\{[Mn^{II}(R\text{-}/S\text{-mpm})_2]_2[Nb^{IV}(CN)_8]\}\cdot 4H_2O$ mpm = (*R*)-/(*S*)-α-methyl-2-pyridine-methanol	2D	yes**	ferrimagnetism	23.5 K	–	[83]
$\{[Mn^{II}(pyrazole)_4]_2[Nb^{IV}(CN)_8]\}\cdot 4H_2O$	3D	no	ferrimagnetism	24 K	−6.8 cm^{-1}	[135]
$\{Mn^{II}_2(5\text{-aminopyrimidine})_2[Nb^{IV}(CN)_8]\}\cdot 5H_2O$	3D	no	ferrimagnetism	32 K	−6.1 cm^{-1}	[136]
$\{Mn^{II}_2(5\text{-methylpyrimidine})_2[Nb^{IV}(CN)_8]\}\cdot 4H_2O$	3D	no	ferrimagnetism	34 K	−6.5 cm^{-1}	[136]
$\{Mn^{II}_5(3\text{-hydroxypyridine})_{12}[Nb^{IV}(CN)_8]_2\}\cdot 6H_2O$	2D	no	ferrimagnetism	16 K	−4.1 cm^{-1}	[137]
$\{[Mn^{II}_3(HCOO)_2(H_2O)_4][Mn^{II}(H_2O)_3(HCONH_2)]_2$ $[Nb^{IV}(CN)_8]_2\}\cdot 4HCONH_2\cdot 2H_2O$	2D	no	ferrimagnetism	17.8 K	–	[138]
$\{[Mn^{II}(H_2O)_2][Mn^{II}(pyrazine)(H_2O)_2][Nb^{IV}(CN)_8]\cdot 4H_2O$	3D	yes**	ferrimagnetism	48 K	–	[86]
α-$\{[Mn^{II}(H_2O)(urea)_2]_2[Nb^{IV}(CN)_8]\}$	3D	yes**	ferrimagnetism	43 K	−10.9 cm^{-1}	[87]
β-$\{[Mn^{II}(H_2O)(urea)_2]_2[Nb^{IV}(CN)_8]\}$	3D	no	ferrimagnetism	42 K	−10.2 cm^{-1}	[87]
$\{[Mn^{II}_2(4,4'\text{-bpdo})(H_2O)_4][Nb^{IV}(CN)_8]\}\cdot 6H_2O$	2D	yes**	antiferromagnetism with spin-flop	15 K	–	[139]
$\{[Mn^{II}_3(4\text{-aminopyridine})_{10}(4\text{-aminopyridinium})_2]$ $[Nb^{IV}(CN)_8]_2\}\cdot 12H_2O$	2D	no	antiferromagnetism with spin-flip	9 K	–	[82]
$\{[Mn^{II}(pyridazine)(H_2O)_2][Mn(H_2O)_2][Nb^{IV}(CN)_8]\}\cdot 2H_2O$	3D	no	ferrimagnetism	43 K/68 K (deh) 100 K (anh)	−9.2 cm^{-1}/ −12.4 cm^{-1} −17.8 cm^{-1}	[140]
$\{[Mn^{II}(imidazole)_2(H_2O)_4][Nb^{IV}(CN)_8]\}\cdot 4H_2O$	3D	no	ferrimagnetism	25 K 62 K (deh)	–	[141]
$\{[Mn^{II}(pyrazine)_2(H_2O)_4][Nb^{IV}(CN)_8]\}\cdot pyrazine\cdot 3H_2O$	3D	no	ferrimagnetism	27 K	–	[142]
$\{[Mn^{II}(pyrazine\text{-}N,N'\text{-dioxide})(H_2O)_4][Nb^{IV}(CN)_8]\}\cdot 5H_2O$	3D	no	ferrimagnetism	37 K	–	[142]
$\{[Mn^{II}(2,2'\text{-bipyrimidine})(H_2O)_2][Nb^{IV}(CN)_8]\}\cdot 5H_2O$	3D	no	ferrimagnetism	50 K	–	[142]

Table 3-1. Comparison of Magnetic Properties of Magnets with Other Reported $[Nb(CN)_8]$-Based Molecule-Based Magnets (Continued).

Compound	Type of Cyanido-Bridged Network	Chirality	Type of Magnetic Ordering	Critical Temperature	Superexchange Interaction*	ref.
$\{[Mn^{II}(H_2O)_2]_2[Nb^{IV}(CN)_8]\}\cdot 4H_2O$	3D	no	ferrimagnetism	47 K	–	[129]
$\{[Mn^{II}(tmphen)_2]_4[Nb^{IV}(CN)_8]_2\}\cdot solv$	0D	yes	paramagnetism	–	$-9.4\ cm^{-1}$	[143]
$(NH_4)[(H_2O)Mn^{II}\text{-}(\mu\text{-}N_3)\text{-}Mn^{II}(H_2O)][Nb^{IV}(CN)_8]\cdot 3H_2O$	3D	no	ferrimagnetism	30 K	–	[144,145]
$(NH_4)[(H_2O)Mn^{II}\text{-}(\mu\text{-}HCOO)\text{-}Mn^{II}(H_2O)][Nb^{IV}(CN)_8]\cdot 3H_2O$	3D	no	ferrimagnetism	44 K	–	[145]
$(NH_4)[(H_2O)Mn^{II}\text{-}(\mu\text{-}CN)\text{-}Mn^{II}(H_2O)][Nb^{IV}(CN)_8]\cdot 3H_2O$	3D	no	ferrimagnetism	40 K	–	[145]
$\{[Co^{II}(4\text{-pyridinealdoxime})_4]_2[Nb^{IV}(CN)_8]\}\cdot 5H_2O$	3D	no	ferromagnetism	18 K	$17.8\ cm^{-1}$	[136]
$\{[Co^{II}(pyrazole)_4]_2[Nb^{IV}(CN)_8]\}\cdot 4H_2O$	3D	no	ferromagnetism	6 K	$3.5\ cm^{-1}$	[135]
$\{[Co^{II}(tmphen)_2]_4[Nb^{IV}(CN)_8]_2\}\cdot solv$	0D	yes	paramagnetism	–	–	[143]
$\{Fe^{II}_2(3\text{-}OAcpy)_5(3\text{-}OHpy)_3[Nb^{IV}(CN)_8]\}\cdot H_2O$	3D	no	paramagnetism	–	–	[76]
$\{[Fe^{II}(tmphen)_2]_4[Nb^{IV}(CN)_8]_2\}\cdot solv$	0D	yes	paramagnetism	–	–	[143]
$\{[Fe^{II}(pyrazole)_4]_2[Nb^{IV}(CN)_8]\}\cdot 4H_2O$	3D	no	ferrimagnetism	8 K	$-3.1\ cm^{-1}$	[135]
$\{[Fe^{II}(H_2O)_2]_2[Nb^{IV}(CN)_8]\}\cdot 4H_2O$	3D	no	ferromagnetism	43 K	$8.1\ cm^{-1}$	[146]

*) The en dashes mean that there is no mention to the value of the superexchange interaction in the reference papers.

**) The 3D Mn-pyrazine-Nb,[86] Mn-urea-Nb,[87] and Mn-4,4'-bpdo-Nb[138] networks reveal the chiral space groups but only one of two enantiomorphic forms were obtained. The only example of Mn-Nb chiral network with two structurally characterized enantiomers is 2D Mn-mpm-Nb coordination polymer obtained using chiral (R)- or (S)-mpm ligands.[83]

Chapter 4: Second Harmonic Generation of Mn^{II}–Nb^{IV} Cyanido Bridged Bimetal Assemblies

4.1 Introduction

As shown in chapter 2 and chapter 3, **MnNbIpy** and **MnNbBrpy** are chiral ferrimagnets with the T_C values of 22 K and 28 K, respectively. **MnNbIpy** and **MnNbBrpy** lack inversion symmetry and therefore will show second harmonic generation. In this chapter, SHG measurements for powder samples of **MnNbIpy** and **MnNbBrpy** are introduced. The SH susceptibility tensors for **MnNbIpy** and **MnNbBrpy** are analyzed based on their point groups provided from the single-crystal structural analyses.

4.2 Experimental Details

A 775 nm laser light, derived from a frequency doubled Ti:sapphire laser (Clark-MXR CPA-2001, 1 kHz repeating frequency, 150 fs peak width, 150 mW laser power), was used to the experiment. The laser, which passed through neutral density (ND) filters, color glass filters, and long pass filters, was focused using a lens and irradiated to a sample (Figure 4-1). The reflected light was passed through blue filters and IR cut filters, and focused using an another lens into a photomultiplier tube (Hamamatsu R329-02) equipped with a band pass filter. There were two shutters to control the measurement times. One was between the ND filters and the other was in the front of the photomultiplier tube. The measurements were repeated with the shutter open time of 1 sec and the shutter close time of 2 sec. The power of irradiated light were reduced less than 1.5% of the laser light by the ND filters for the PMT counts not to exceed 200 counts per measurement. The power of the 775 nm irradiated light was altered by changing the ND filters. The observation wavelength is altered by changing the band pass filter.

The wavelength of the observed lights was determined with changing the bandpass filters, and the dependence of the power of the irradiated light was observed with changing the amount of the ND filters.

For the SHG measurement, powder samples of **MnNbIpy** and **MnNbBrpy** were placed between glass plates. Potassium dihydrogen phosphate (KDP) was used as a reference sample for SH intensity.

4.3 Result

When the fundamental light irradiated to the sample at room temperature, the 388 nm light was observed using the 388 nm bandpass filter, while with 405 nm or 365 nm bandpass filters, no light is detected (Figure 4-2, Right). Thus, the output lights is monochromatic at 388 nm. The laser power dependence measurement revealed that the output light intensity depends on the power of the fundamental light (Figure 4-3, Left). The results show that the intensity of the observed light correspond well to the quadratic function of the power of the irradiated 775 nm lights. These characteristics conclude that the observed lights are second harmonic generation light from the powder samples.

The observed SH intensity of **MnNbIpy** was 0.095% of the KDP sample and that of **MnNbBrpy** was 0.008% of the KDP sample. **MnNbIpy** shows stronger SH intensity than **MnNbBrpy**.

4.4 Discussion

The space group of **MnNbIpy** is $I4_1$, which belongs to a point group 4. In the point group 4, the SH susceptibility tensor $\chi^{(2)}$ is described below.

$$\chi^{(2)} = \begin{pmatrix} 0 & 0 & 0 & \chi_{14} & \chi_{15} & 0 \\ 0 & 0 & 0 & \chi_{15} & -\chi_{14} & 0 \\ \chi_{31} & \chi_{31} & \chi_{33} & 0 & 0 & 0 \end{pmatrix} \quad (4\text{-}1)$$

As shown above, the $\chi^{(2)}$ of **MnNbIpy** has four independent elements. Similarly, the space group of **MnNbBrpy** is $I4_122$, which belongs to a point group 422, and then the SH susceptibility tensor $\chi^{(2)}$ is described below.

$$\chi^{(2)} = \begin{pmatrix} 0 & 0 & 0 & \chi_{14} & 0 & 0 \\ 0 & 0 & 0 & 0 & -\chi_{14} & 0 \\ 0 & 0 & 0 & 0 & 0 & 0 \end{pmatrix} \quad (4\text{-}2)$$

As shown above, the $\chi^{(2)}$ of **MnNbBrpy** has one independent elements. These tensor analyses confirm that **MnNbIpy** and **MnNbBrpy** are SHG active.

From the results of the SHG measurement of powder samples, we cannot determine the respective SH susceptibility tensors. However, the difference between the SH susceptibility tensors of 4 and 422 point groups should affect the SH light intensity of **MnNbIpy** and **MnNbBrpy** as shown in the results of the SHG measurements.

4.5 Conclusion

The SHG of **MnNbIpy** and **MnNbBrpy** with non-centrosymmetric structures have been observed by using the incident light of the 775 nm laser. Additionally, the tensor analyses confirm that **MnNbIpy** and **MnNbBrpy** are SHG active. Although the SH susceptibility tensors cannot be determined from the powder sample measurements, the difference of the point group between 4 and 422 should provide the difference of the SH intensities. The difference in the crystal structures of **MnNbIpy** and **MnNbBrpy** probably depends on the strength of the halogen bonds inducing the structural distortion on the Mn coordination geometry. Thus, this result suggests that weak intermolecular interaction like halogen bondings is useful for controlling crystal structure and crystal symmetry as well as SHG properties.

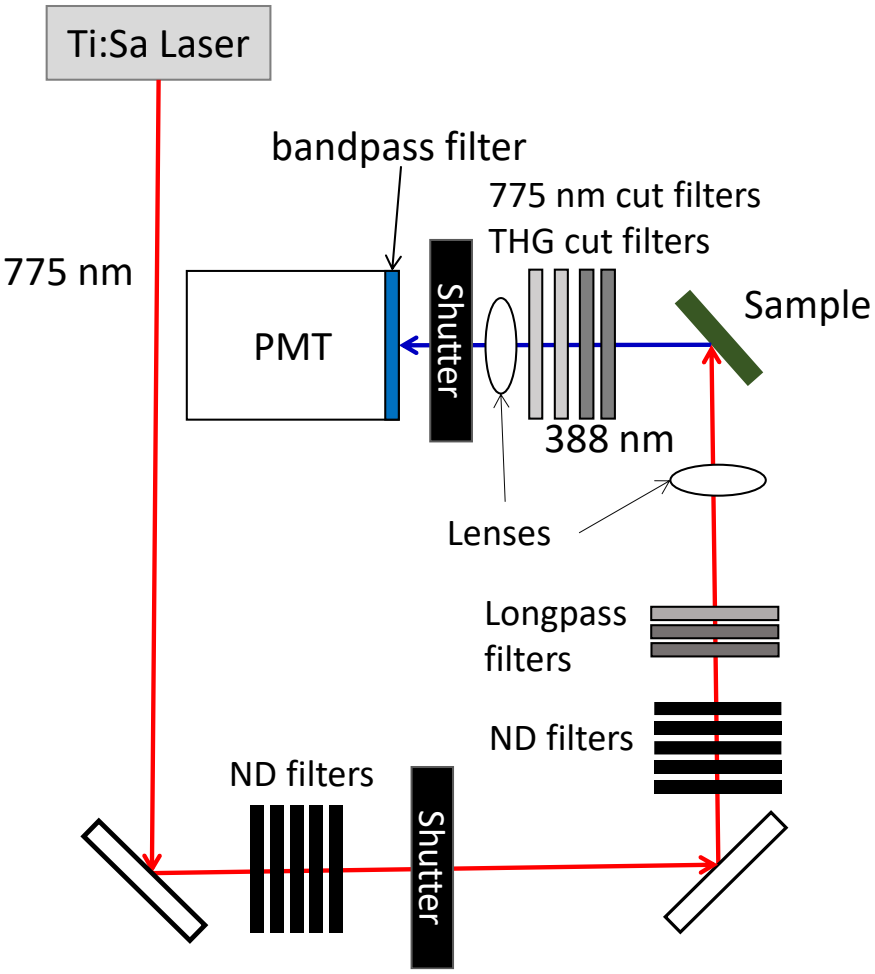

Figure 4-1. A schematic view of experimental setup.

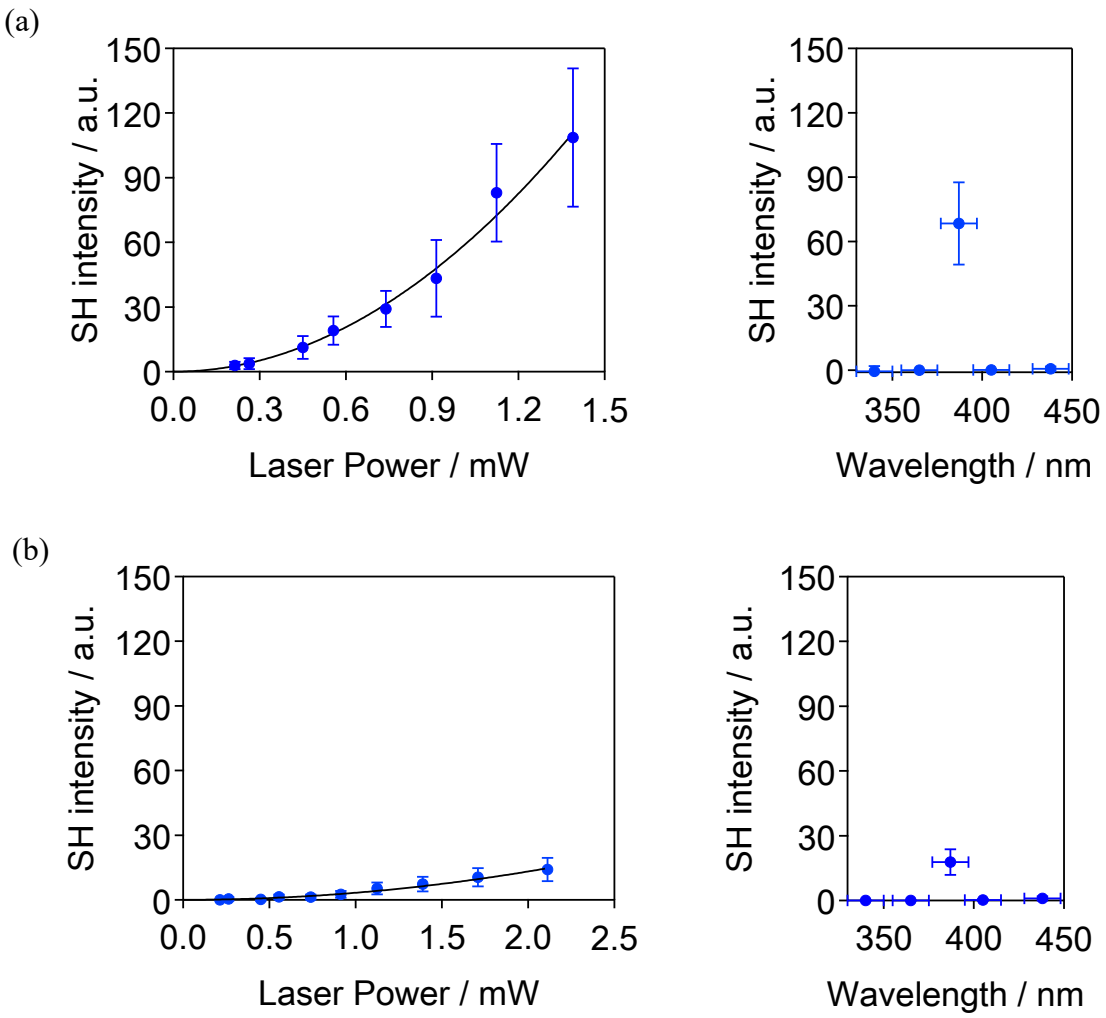

Figure 4-2. (Right) the SH light intensity vs the irradiated light intensity plots where black solid lines represent quadratic function fittings and (left) the wavelength of the SH light. The horizontal error bars means FWMH of bandpass filters. (a) **MnNbIpy** and (b) **MnNbBrpy**.

Adapted from Ref. [151] with permission from the Royal Society of Chemistry.

Chapter 5: Conclusion

In summary, I studied syntheses, crystal structures, magnetic properties, and nonlinear optical properties of the chiral magnets and the achiral magnet based on cyanido-bridged metal assemblies.

In chapter 2, I reported the syntheses and crystal structures of $[Mn(4\text{-iodopyridine})_4]_2[Nb(CN)_8]$ (**MnNbIpy**), $[Mn(4\text{-bromopyridine})_4]_2[Nb(CN)_8]\cdot 0.5H_2O$ (**MnNbBrpy**), and $[Mn(4\text{-chloropyridine})_4]_2[Nb(CN)_8]\cdot 0.5H_2O$ (**MnNbClpy**). **MnNbIpy** and **MnNbBrpy** have the chiral structures with the space groups $I4_1$ and $I4_122$, respectively. However, **MnNbClpy** shows an achiral structure with the space group *Fddd*. These compounds have the similar 3D coordination networks. There are halogen bondings between 4-halopyridine and terminal cyanido ligands. In **MnNbIpy** and **MnNbBrpy**, the coordination geometries around the Mn^{2+} ions are distorted by the halogen bonding, forming the two types of the helical structures that lead to the chiral structures.

In chapter 3, I discussed the magnetic properties of the powder samples. These compounds have the $\{Mn^{II}_{HS\,2}Nb^{IV}_1\}$ unit per chemical formula as paramagnetic metal centers. They show ferromagnetism with the curie temperature of 22 K, 28 K, and 28 K, for **MnNbIpy**, **MnNbBrpy**, and **MnNbClpy**, respectively, and they show ferrimagnetic ordering where magnetic moments of the Mn^{2+} ions and Nb^{4+} ions order antiparallelly.

In chapter 4, I reported second harmonic generation phenomena of **MnNbBrpy** and **MnNbIpy**. The observed lights are monochromatic on the wavelength half of that of the irradiated light and show quadratic dependence on the power of the irradiated light. The SHG light intensity of **MnNbIpy** are stronger than that of **MnNbBrpy** because **MnNbIpy** has lower symmetry.

I synthesized two chiral magnets from achiral building blocks. These compounds show halogen bondings and these halogen bondings should lead the chirality of them. These compounds show ferrimagnetism and SHG effects. The results suggest that weak interactions

like halogen bondings are worth considering as fine-tuning to make a chiral structure and then SHG property in molecule-based magnets.

References

[1] H. H. Wickman, A. M. Trozzolo, H. J. Williams, G. W. Hull, and F. R. Merritt, *Phys. Rev.*, 1967, **155**, 563.

[2] M. Kinoshita, P. Turek, M. Tamura, K. Nozawa, D. Shiomi, Y. Nakazawa, M. Ishikawa, M. Takahashi, K. Awaga, *Chem. Lett.*, 1991, **20**, 1225.

[3] G. N. Newton, M. Nihei, H. Oshio, *Eur. J. Inorg. Chem.*, 2011, 3031.

[4] T. Korzeniak, B. Nowicka, K. Stadnicka, W. Nitek, A. M. Majcher, B. Sieklucka, *Polyhedron*, 2013, **52**, 442.

[5] S. Ohkoshi, T. Iyoda A. Fujishima, K. Hashimoto, *Phys. Rev. B*, 1997, **56**, 11642.

[6] S. Ohkoshi, K. Hashimoto, *Phys. Rev. B*, 1999, **60**, 12820.

[7] A. N. Holden, B. T. Matthias, P. W. Anderson, H. W. Lewis, *Phys. Rev.*, 1956, **102**, 1463.

[8] A. Takahashi, H. Tanaka, D. Parajuli, T. Nakamura, K. Minami, Y. Sugiyama, Y. Hakuta, S.Ohkoshi, T. Kawamoto, *J. Am. Chem. Soc.*, 2016 **138**, 6376.

[9] A. Takahashi, A. Kitajima, D. Parajuli, Y. Hakuta, H. Tanaka, S. Ohkoshi, T. Kawamoto, *Chem. Eng. Res. Des.*, 2016, **109**, 513.

[10] A. Takahashi, N. Minami, H. Tanaka, K. Sue, K. Minami, D. Parajuli, K.-M. Lee, S. Ohkoshi, M. Kurihara, T. Kawamoto, *Green Chem.*, 2015, **17**, 4228.

[11] N. L. Torad, M. Hu, M. Imura, M. Naito, Y. Yamauchi, *J. Mater., Chem.*, 2012, **22**, 18261.

[12] B. Hua, B. Fugetsua, H. Yua, Y. Abe, *J. Hazard. Mater.*, 2012, **217-218**, 85.

[13] S. Vlasselaer, W. D'Olieslager, M. D'Hont, *J. Inorg. Nucl. Chem.*, 1976, **38**, 327.

[14] G. B. Barton, J. L. Hepworth, E. D. McClanahan Jr., R. L. Moore, H. van Tuyl, *Ind. Eng. Chem.*, 1958, **50**, 212.

[15] S. Ferlay, T. Mallah, R. Ouahès, P. Veillet, M. Verdaguer, *Nature*, 1995, **378**, 701.

[16] E. Dujardin, S. Ferlay, X. Phan, C. Desplanches, C. Cartier dit Moulin, P. Sainctavit, F. Baudelet, E. Dartyge, P. Veillet, M. Verdaguer, *J. Am. Chem. Soc.*, 1998, **120**, 11347.

[17] O. Hatlevik, W. E. Buschmann, J. Zhang, J. L. Manson, J. S. Miller, *Adv. Mater.*, 1999, **11**, 914.

[18] S. M. Holmes, G. S. Girolami, *J. Am. Chem. Soc.*, 1999, **121**, 5593.

[19] M. Mizuno, S. Ohkoshi, K. Hashimoto, *Adv. Mater.*, 2000, **12**, 1955.

[20] R. Garde, F. Villain, M. Verdaguer, *J. Am. Chem. Soc.*, 2002, **124**, 10531.

[21] E. Ruiz, A. Rodríguez-Fortea, S. Alvarez, M. Verdaguer, *Chem. Eur.-J.*, 2005, **11**, 2135.

[22] R. Garde, J. M. Herrera, F. Villain, M. Verdaguer, *Inorg. Chim. Acta*, 2008, **361**, 3597.

[23] K. Ikeda S. Ohkoshi, K. Hashimoto, *Chem. Phys. Lett.*, 2001, **349**, 371.

[24] K. Ikeda, S. Ohkoshi, K. Hashimoto, *J. Elect. Soc.*, 2002, **149**, E445.

[25] S. Ohkoshi, S. Saito, T. Matsuda, T. Nuida, H. Tokoro, *J. Phys. Chem. C*, 2008, **112**, 13095.

[26] A. Ould-Hamouda, A. Iazzolino, H. Tokoro, S. Ohkoshi, E. Freysz, *Eur. J. Inorg. Chem.*, 2018, **3-4**, 378.

[27] T. Nuida, T. Matsuda, H. Tokoro, S. Sakurai, K. Hashimoto, S. Ohkoshi, *J. Am. Chem. Soc.*, 2005, **127**, 11604.

[28] K. Ikeda, S. Ohkoshi, K. Hashimoto, *J. Appl. Phys.*, 2003, **93**, 1371.

[29] S. Ohkoshi, K. Ikeda, J. Shimura, K. Hashimoto, *Trans. Magn. Soc. Jpn.*, 2004, **4**, 266.

[30] S. Ohkoshi, Y. Abe, A. Fujishima, K. Hashimoto, *Phys. Rev. Lett.*, 1999, **82**, 6, 1285.

[31] S. Ohkoshi, H. Tokoro, T. Matsuda, H. Takahashi, H. Irie, K. Hashimoto, *Angew. Chem., Int. Ed.*, 2007, **46**, 3238.

[32] S. Ohkoshi, K. Arai, Y. Sato, K. Hashimoto, *Nat. Mater.*, 2004, **3**, 857.

[33] D. Aguila`, Y. Prado, E. S. Koumousi, C. Mathonière, R. Clérac, *Chem. Soc. Rev.*, 2006, **45**, 203.

[34] O. Sato, T. Iyoda, K. Hashimoto, *Science*, 1996, **272**, 704.

[35] H. Tokoro, S. Miyashita, K. Hashimoto, S. Ohkoshi, *Phys. Rev. B*, 2006, **73**, 172415.

[36] S. Ohkoshi, T. Matsuda, H. Tokoro, K. Hashimoto, *Chem. Mater.*, 2005, **17**, 81.

[37] H. Tokoro, S. Ohkoshi, T. Matsuda, K. Hashimoto, *Inorg. Chem.*, 2004, **43**, 5231.

[38] T. Yokoyama, H. Tokoro, S. Ohkoshi, K. Hashimoto, K. Okamoto, T. Ohta, *Phys. Rev. B*, 2002, **66**, 184111.

[39] Y. Morimoto, K. Kato, A. Kuriki, M. Takata, M. Sakata H. Tokro, S. Ohkoshi, K. Hashimoto, *J. Phys. Soc. Jpn.*, 2002, **9**, 2078.

[40] S. Ohkoshi, H. Tokoro, M. Utsunomiya, M. Mizuno, M. Abe, K. Hashimoto, *J. Phys. Chem. B*, 2002, **106**, 2423.

[41] W. Kosaka, K. Nomura, K. Hashimoto, S. Ohkoshi, *J. Am. Chem. Soc.*, 2005, **127**, 8590.

[42] S. Ohkoshi, K. Nakagawa, K. Tomono, K. Imoto, Y. Tsunobuchi, H. Tokoro, *J. Am. Chem. Soc.*, 2010, **132**, 6620.

[43] T. Matsuda, H. Tokoro, M. Shiro, K. Hashimoto, S. Ohkoshi, *Acta Cryst. E*, 2008, **64**, i11.

[44] G. Handzlik, M. Magottt, B. Sieklucka, D. Pinkowicz, *Eur. J. Inorg. Chem.*, 2016, **30**, 4872.

[45] B. Sieklucka, J. Szklarzewicz, T. J. Kemp, W. Errington, *Inorg. Chem.*, 2000, **39**, 5156.

[46] Z. J. Zhong, H. Seino, M. Gross, Y. Mizobe, M. Hidai, A. Fujishima, S. Ohkoshi, K. Hashimoto, *J. Am. Chem. Soc.*, 2000, **122**, 2952.

[47] J. Larionova, M. Gross, M. Pilkington, H. Andres, H. Stoeckli-Evans, H. U. Güdel, S. Decurtins, *Angew. Chem. Int. Ed.*, 2000, **39**, 1605.

[48] G. Rombaut, S. Golhen, L. Ouahab, C. Mathonière, O. Kahn, *J. Chem. Soc., Dalton Trans.*, 2000, 3609.

[49] D. Li, S. Gao, L. Zheng, K. Yuc, W. Tang, *New J. Chem.*, 2002, **26**, 1190.

[50] Y. Arimoto, S. Ohkoshi, Z. J. Zhong, H. Seino, Y. Mizobe, K. Hashimoto, *Chem. Lett.*, 2002, **31**, 832.

[51] F. Chang, H.-L. Sun, H.-Z. Kou, S. Gao, *Inorg. Chem. Commun.*, 2002, **5**, 660.

[52] R. Podgajny, T. Korzeniak, M. Bałanda, T. Wasiutyński, W. Errington, T. J. Kemp, N. W. Alcock, B. Sieklucka, *Chem. Commun.*, 2002, 1138.

[53] J. Lu, W. T. A. Harrison, A. J. Jacobson, *Angew. Chem., Int. Ed. Engl.*, 1995, **34**, 2557.

[54] M. Pilkington, S. Decurtins, *CHIMIA*, 2000, **54**, 593.

[55] E. Chelebaeva, J. Larionova, Y. Guari, R. A. Sá Ferreira, L. D. Carlos, F. A. Almeida Paz, A. Trifonov, C. Guerin, *Inorg. Chem.*, 2005, **47**, 775.

[56] E. Chelebaeva, J. Larionova, Y. Guari, R. A. S. Ferreira, L. D. Carlos, F. A. Almeida Paz, A. Trifonov, C. Guerin, *Inorg. Chem.*, 2006, **48**, 5983.

[57] S. Chorazy, K. Nakabayashi, S. Ohkoshi, B. Sieklucka, *Chem. Mater.*, 2014, **26**, 4072.

[58] S. Chorazy, K. Nakabayashi, M. Arczynski, R. Pełka, S. Ohkoshi, B. Sieklucka, *Chem. A Eur. J.*, 2014, **20**, 7144.

[59] S. Chorazy, M. Arczynski, K. Nakabayashi, B. Sieklucka, S. Ohkoshi, *Inorg. Chem.*, 2015, **54**, 4724.

[60] G. Rombaut, S. Golhen, L. Ouahab, C. Mathonière O. Kahn, *J. Chem. Soc., Dalton Trans.*, 2000, 3609.

[61] S. Ohkoshi, N. Machida, Y. Abe, Z. J. Zhong, K. Hashimoto, *Chem. Lett.*, 2001, 312.

[62] Y. Arimoto, S. Ohkoshi, Z. J. Zhong, H. Seino, Y. Mizobe, K. Hashimoto, *J. Am. Chem. Soc.*, 2005, **125**, 9240.

[63] N. Bridonneau, J. Long, J.-L. Cantin, J. von Bardeleben, S. Pillet, E.-E. Bendeif, D. Aravena, E. Ruiz V. Marvaud, *Chem. Commun.*, 2015, **51**, 8229.

[64] M. Magott, O. Stefańczyk, B. Sieklucka, D. Pinkowicz, *Angew. Chem. Int. Ed.*, 2017, **56**, 13283.

[65] B. Nowicka, M. Rams, K. Stadnicka, B. Sieklucka, *Inorg. Chem.*, 2017, **20**, 46, 8123.

[66] K. Nakabayashi, S. Chorazy, M. Komine, Y. Miyamoto, D. Takahashi, B. Sieklucka, S. Ohkoshi, *Cryst. Growth Des.*, 2017, **17**, 9, 4511.

[67] Y. Tsunobuchi, S. Kaneko, K. Nakabayashi, S. Ohkoshi, *Cryst. Growth Des.*, 2011, **11**, 5561.

[68] K. Nakabayashi, S. Chorazy, D. Takahashi, T. Kinoshita, B. Sieklucka, S. Ohkoshi, *Cryst. Growth Des.*, 2014, **14**, 6093.

[69] D. Visinescu, A. M. Madalan, M. Andruh, C. Duhayon, J.-P. Sutter, L. Ungur, W. Van den Heuvel, L. F. Chibotaru, *Chem, Eur. J.*, 2009, **15**, 11808.

[70] R.-M. Wei, F. Cao, J. Li, L. Yang, Y. Han, X.-L. Zhang, Z. Zhang, X.-Y. Wang, Y. Song, *Sci. Rep.*, 2016, **6**, 24372.

[71] Y. Song, P. Zhang, X.-M. Ren, X.-F. Shen, Y.-Z. Li, X.-Z. You, *J. Am. Chem. Soc.*, 2005, **127**, 3708.

[72] J.-P. Sutter, S. Dhers, R. Rajamani, S. Ramasesha, J.-P. Costes, C. Duhayon, L. Vendier, *Inorg. Chem.*, 2009, **48**, 5820.

[73] S. Chorazy, M. Rams, A. Hoczek, B. Czarnecki, B. Sieklucka, S. Ohkoshi, R. Podgajny, *Chem. Commun.*, 2016, **52**, 4772.

[74] B. Sieklucka, R. Podgajny, T. Korzeniak, B. Nowicka, D. Pinkowicz, M. Kozieł, *Eur. J. Inorg. Chem.*, 2011, 305.

[75] M. Arai, W. Kosaka, T. Matsuda, S. Ohkoshi, *Angew. Chem., Int. Ed.*, 2008, **47**, 6885.

[76] S. Kawabata, S. Chorazy, J. J. Zakrzewski, K. Imoto, T. Fujimoto, K. Nakabayashi, J. Stanek, B. Sieklucka, S. Ohkoshi, *Inorg. Chem.*, 2019, **58**, 6052.

[77] D. Pinkowicz, M. Rams, M. Misek, K. V. Kamenev, H. Tomkowiak, A. Katrusiak, B. Sieklucka, *J. Am. Chem. Soc.*, 2015, **137**, 8795.

[78] S. Ohkoshi, K. Imoto, Y. Tsunobuchi, S. Takano, H. Tokoro, *Nat. Chem.*, 2011, **3**, 564.

[79] K. Imoto, S. Ohkoshi, *Chem. Lett.*, 2015, **45**, 359.

[80] M. Arczynski, M. Rams, J. Stanek, M. Fitta, B. Sieklucka, K. R. Dunbar, D. Pinkowicz, *Inorg. Chem.*, 2017, **56**, 4021.

[81] K. Imoto, D. Takahashi, Y. Tsunobuchi, W. Kosaka, M. Arai, H. Tokoro, S. Ohkoshi, *Eur. J. Inorg. Chem.*, 2010, **26**, 4079.

[82] K. Imoto, K. Nakagawa, H. Miyahara, S. Ohkoshi, *Cryst. Growth Des.*, 2013, **13**, 4673.

[83] S. Chorazy, R. Podgaijny, W. Nitek, T. Fic, E. Görlich, M. Rams B. Sieklucka, *Chem. Commun.*, 2013, **49**, 6731.

[84] W. Kosaka, T. Nuida, K. Hashimoto, S. Ohkoshi, *Bull. Chem. Soc. Jpn.*, 2007, **80**, 960.

[85] W. Kosaka, K. Hashimoto, S. Ohkoshi, *Bull. Chem. Soc. Jpn.*, 2008, **81**, 992.

[86] Y. Tsunobuchi, W. Kosaka, T. Nuida, S. Ohkoshi, *CrystEngComm*, 2009, **11**, 2051.

[87] D. Pinkowicz, R. Podgajny, W. Nitek, M. Rams, A. M. Majcher, T. Nuida, S. Ohkoshi, B. Sieklucka, *Chem. Mater.*, 2011, **23**, 21.

[88] M. Pilkinton, S. Decurtins, *CHIMIA*, 2000, **54**, 593.

[89] R. Pradhan, C. Desplanches, P. Guionneau, J.-P. Sutter, *Inorg. Chem.*, 2003, **42**, 6607.

[90] S. Ohkoshi, S. Takano, K. Imoto, M. Yoshikiyo, A. Namai, H. Tokoro, *Nat. Photonics*, 2014, **8**, 65.

[91] G. L. J. A. Rikken, E. Raupach, *Nature*, 1997, **390**, 493.

[92] Y. Kitagawa, H. Segawa, K. Ishii, *Angew. Chem., Int. Ed.*, 2011, **50**, 9133.

[93] P. Kleindienst, G. H. Wagniere, *Chem. Phys. Lett.*, 1998, **288**, 89.

[94] N. G. Kalugin, P. Kleindienst, G. H. Wagniere, *Chem. Phys.*, 1999, **248**, 105.

[95] M. Vallet, R. Ghosh, A. Le Floch, T. Ruchon, F. Bretenaker, J.-Y.Thépot, *Phys. Rev. Lett.*, 2001, **87**, 183003.

[96] S. Chorazy, M. Reczyński, R. Podgajny, W. Nogaś, S. Buda, M. Rams, W. Nitek, B. Nowicka, J. Mlynarski, S. Ohkoshi, B. Sieklucka, *Cryst. Growth Des.*, 2015, **15**, 3573.

[97] L. Tian, C.-Y. Panga, F.-L. Zhang, L.-F. Qin, Z.-G. Gu, Z. Li, *Inorg. Chem. Commun.*, 2015, **53**, 55.

[98] S. Chorazy, R. Podgajny, W. Nitek, T. Fic, E. Go¨rlich, M. Rams, B. 64 Sieklucka, *Chem. Commun.*, 2013, **49**, 6731.

[99] S. Chorazy, K. Nakabayashi, K. Imoto, J. Mlynarski, B. Sieklucka, S. Ohkoshi, *J. Am. Chem. Soc.*, 2012, **134**, 16151.

[100] Y. Zheng, X.-J. Kong, L.-S. Long, R.-B. Huang, L.-S. Zheng, *Dalton Trans.*, 2011, **40**, 4035.

[101] L. Li, S. Nishihara, K. Inoue, M. Kurmoo, *Inorg. Chem.*, 2016, **55**, 3047.

[102] K. Inoue, H. Imai, P. S. Ghalsasi, K. Kikuchi, M. Ohba, H. Okawa, J. V. Yakhmi, *Angew. Chem., Int. Ed.*, 2001, **40**, 4242.

[103] Eugenio Coronado, C. J. Gómez-García, A. Nuez, F. M. Romero, J. C. Waerenborgh, *Chem. Mater.*, 2006, **18**, 2670.

[104] S. Chorazy, K. Nakabayashi, M. Arczynski, R. Pełka, S. Ohkoshi, B. Sieklucka, *Chem. Eur, J.*, 2014, **20**, 7144.

[105] C.-Q. Jiao, Z. Zhao, C. Ma, Z.-G. Sun, D.-P. Dong, Y.-Y. Zhu, J. Li, *Cryst. Growth Des.*, 2016, **16**, 5624.

[106] T. Shiga, K. Maruyama, G. N. Newton, R. Inglis, E. K. Brechin, H. Oshio, *Inorg. Chem.*, 2014, **53**, 4272.

[107] Y. W. Zhang, Z.-Q. Wang, O. Sato, R.-G. Xiong, *Cryst. Growth Des.*, 2009, **9**, 2050.

[108] D. Armentano, G. De Munno, F. Lloret, A. V. Palii, M. Julve, *Inorg. Chem.*, 2002, **41**, 2007.

[109] P. D. Maker, R. W. Terhune, *Phys. Rev.*, 1965, **137**, A801.

[110] J. F. Ward, G. H. C. *New, Phys. Rev.*, 1969, **185**, 57.

[111] N. Sarukura, K. Hata, T. Adachi, R. Nodomi, M. Watanabe, S. Watanabe, *Phys. Rev. A*, 1991, **43**, 1669.

[112] P. A. Franken, A. E. Hill, C. W. Peters, G. Weinreich, *Phys. Rev. Lett.*, 1961, **7**, 118.

[113] O.A. Aktsipetrov, O. V. Braginskii, D. A. Esikov, *Sov. J. Quantum Electron*, 1990, **20**, 259.

[114]J. Reif, J. C. Zink, C.-M. Schneider, J. Kirschner, *Phys. Rev. Lett.*, 1991, **67**, 2878.

[115] M. Fiebig and D. Frohlich, B. B. Krichevtsov, R. V. Pisarev, *Phys. Rev. Lett.*, 1994, **73**, 2127.

[116] J. Reif, C. Rau, E. Matthias, *Phys. Rev. Lett.*, 1993, **71**, 1931.

[117] D. Fröhlich, St. Leute, V. V. Pavlov, R. V. Pisarev,, *Phys. Rev. Lett.*, 1998, **81**, 3239.

[118] C. Train, T. Nuida, R. Gheorghe, M. Gruselle, S. Ohkoshi, *J. Am. Chem. Soc.*, 2009, **131**, 16838.

[119] G. Spierings, V. Koutsos, H. A. Wierenga, M. W. J. Prins, D. Abraham, Th. Rasing, *J. Magn. Magn. Mater.*, 1993, **121**, 109.

[120] M. Fiebig, D. Fröhlich, K. Kohn, St. Leute, Th. Lottermoser, V. V. Pavlov, R. V. Pisarev, *Phys. Rev. Lett.*, 2000, **84**, 5620.

[121] J. F. McGilp, L. Carroll, K. Fleischer, J. P. Cunniffe, S. Ryan, *J. Magn. Magn. Mater.*, 2010, **322**, 1488.

[122] Th. Rasing, *J. Magn. Magn. Mater.*, 1997, **175**, 35.

[123] P. M. Klernan, W. P. Griffith, *J. Chem. Soc.*, 1975, 2489.

[124] M. C. Burla, R. Caliandro, B. Carrozzini, G. L. Cascarano, C. Cuocci, C. Giacovazzo, M. Mallamo, A. Mazzone, G. Polidori, *J. Appl. Cryst.*, 2015, **48**, 306.

[125] G. M. Sheldrick, *Acta Cryst.*, 2008, **A64**, 112.

[126] L. J. Farrugia, *J. Appl. Cryst.*, 2012, **45**, 849.

[127] K. Momma, F. Izumi, *J. Appl. Cryst.*, 2011, **44**, 1272.

[128] Llunell, M.; Casanova, D.; Cirera, J.; Bofill, J.; Alemany, P.; Alvarez, S.; Pinsky, M.; Avnir, D. SHAPE v. 2.1. Program for the Calculation of Continuous Shape Measures of Polygonal and Polyhedral Molecular Fragments; University of Barcelona: Barcelona, Spain, 2013.

[129] J. M. Herrera, P. Franz, M. Pilkington, M. Biner, S. Decurtins, H. Stoeckli-Evans, A. Neels, R. Garde, Y. Dromzée, M. Julve, B. Sieclucka, K. Hashimoto, S. Ohkoshi, M. Verdaguer, *C. R. Chimie*, 2008, **11**, 1192.

[130] J. P. Wibaut, F. W. Broekman, *Recueil*, 1959, **78**, 593.

[131] W. Heitz, A. Rehder, N. Nießner, *Makromol. Chem., Rapid Commun.*, 1991, **12**, 637.

[132] W. J. Feast, J. Tsibouklis, *Polymer Int.*, 1994, **35**, 67.

[133] K. Nose, T. Iyoda, T. Sanji, *Polymer*, 2014, 3454.

[134] S. Ohkoshi, Y. Abe, A. Fujishima, K. Hashimoto, *Phys. Rev. Lett.*, 1999, **82**, 1285.

[135] D. Pinkowicz R. Pełka, O. Drath, W. Nitek, M. Bałanda, A. M. Majcher, G. Poneti, B. Sieklucka, *Inorg. Chem.*, 2010, **49**, 7565.

[136] K. Imoto, M. Takemura, K. Nakabayashi, Y. Miyamoto, K. Komori-Orisaku, S. Ohkoshi, *Inorg. Chim. Acta*, 2015, **425**, 92.

[137] D. Takahashi, K. Nakabayashi, S. Tanaka, S. Ohkoshi, *Inorg. Chem. Commun.*, 2013, **27**, 47.

[138] T. Korzeniak, D. Pinkowicz, W. Nitek, M. Bałanda, M. Fitta B. Sieklucka, *Dalton Trans.*, 2011, **40**, 12350.

[139] D. Pinkowicz, M. Rams, W. Nitek, B. Czarnecki, B. Sieklucka, *Chem. Commun.*, 2012, **48**, 8323.

[140] D. Pinkowicz, R. Podgajny, B. Gaweł, W. Nitek, W. Łasocha, M. Oszajca, M. Czapla, M. Makarewicz, M. Bałanda, B. Sieklucka, *Angew. Chem., Int. Ed.*, 2011, **50**, 3973.

[141] D. Pinkowicz, R. Podgajny, M. Bałanda, M. Makarewicz, B. Gaweł, W. Łasocha, B. Sieklucka, *Inorg. Chem.*, 2008, **47**, 9745.

[142] R. Podgajny, D. Pinkowicz, T. Korzeniak, W. Nitek, M. Rams, B. Sieklucka, *Inorg. Chem.*, 2007, **46**, 10416.

[143] M. Arczyński, M. Rams, J. Stanek, M. Fitta, B. Sieklucka K. R. Dunbar, D. Pinkowicz, *Inorg. Chem.*, 2017, **56**, 7, 4021.

[144] G. Handzlik, M. Kozieł, A. Olejniczak, B. Sieklucka, D. Pinkowicz, *Chemm. Commun.*, 2017, **70**, 53, 9753.

[145] G. Handzlik, B. Sieklucka, D. Pinkowicz, *Dalton Trans.*, 2018, **47**, 11888.

[146] D. Pinkowicz, R. Podgajny, R. Pełka, W. Nitek, M. Bałanda, M. Makarewicz, M. Czapla, J. Żukrowski, C. Kapusta, D. Zając, B. Sieklucka, *Dalton Trans.*, 2009, 7771.

[147] D. Visinescu, C. Desplanches, I. Imaz, V. Bahers, R. Pradhan, F. A. Villamena, P. Guionneau, J.-P. Sutter, *J. Am. Chem. Soc.*, 2006, **128**, 10202.

[148] R. Podgajny, D. Pinkowicz, T. Korzeniak, W. Nitek, M. Rams, B. Sieklucka, *Inorg. Chem.*, 2007, **46**, 10416.

[149] K. Nakagawa , K. Imoto, H. Miyahara, S. Ohkoshi, *Polyhedron*, 2013, **52**, 424.

[150] T. Ohno, S. Chorazy, K. Imoto, S. Ohkoshi, *Cryst. Growth Des.*, 2016, **16**, 4119.

[151] T. Ohno, K. Nakabayashi, K. Imoto, M. Komine, S. Chorazy, S. Ohkoshi, *CrystEngComm*, 2018, **20**, 7236.

[152] J. K. Burdett, R. Hoffmann, R. C. Fay, *Inorg. Chem.*, 1978, **17**, 9, 2553.

[153] B. Nowicka, M. Bałanda, M. Reczyński, A. M. Majcher, M. Kozieł, W. Nitek, W. Łasocha, B. Sieklucka, *Dalton Trans.*, 2013, **42**, 2616.

List of Papers Related to This Thesis

(1) “4-Bromopyridine-Induced Chirality in Magnetic M^{II}–$[Nb^{IV}(CN)_8]^{4-}$ (M = Zn, Mn, Ni) Coordination Networks”

T. Ohno, S. Chorazy, K. Imoto, S. Ohkoshi, *Cryst. Growth Des.*, 2016, **16**, 4119.

This paper corresponds to part of chap. 2 and 3.

(2) “Chiral cyanido-bridged Mn–Nb magnets including halogen-bonds”

T. Ohno, K. Nakabayashi, K. Imoto, M. Komine, S. Chorazy, S. Ohkoshi, *CrystEngComm*, 2018, **20**, 7236.

This paper corresponds to part of chap. 2-4.

Acknowledgement

First of all, my deepest appreciation goes to Professor Shin-ichi Ohkoshi. He is my supervisor. I have greatly benefited by the good research environment which he managed. Extensive discussions with him were invaluable to my research. I would like to express my gratitude to him again.

I owe a very important debt to Dr. Kenta Imoto, Dr. Koji Nakabayashi, and Dr. Szymon Chorazy because of their valuable advice and meaningful discussion. I would like to thank Dr. Hiroko Tokoro in Tsukuba University. I am indebted to Dr. Kosuke Nakagawa, Dr. Asuka Namai, and Dr. Marie Yoshikiyo. They are assistant professors of Ohkoshi Laboratory.

I am indebt to Dr. Aiko Kamitsubo for many elemental analyses of organic elements.

I want to thank all other members of Ohkoshi Laboratory, Dr. Masaya Komine, Mr. Shintaro Kawabata, Mr. Junhao Wang, Mr. Fangda Jia, Mr. Takefumi Kanno, Mr. Takuma Takeda, Mr. Seiya Tsukamoto, Mr. Satoru Honda, Ms. Rina Kinugawa, Mr. Yuya Shibata, Mr. Takaya Yoshida, Mr. Daisuke Abe, Mr. Yasuhiko Omori, Mr. Ryuichi Tonaka, Mr. Kunal Kumar, Mr. Masaki Adachi, Mr. Mitsuki Hosoda, Mr. Yusuke Ikeda, Mr. Shoma Shimizu, Mr. Tomohiro Tabata, Mr. Kazuki Takahashi, Ms. Jessica Macdougall, Mr. Qinyu Song Mr. Mr. Yue Xin, Mr Yuhei Futakawa, Mr. Kyohei Takeuchi, Mr. Ryo Makuta, Ms. Yuki Mineo, Mr. Yugo Nagane, and Mr. Yuki Toyosaki for their help in laboratory activities.

I am deeply grateful to Advanced Leading Graduate Course for Photon Science (ALPS) for its financial support. I am in debt to Professor Takeaki Ozawa as my secondary supervisor of ALPS.

Finally, I would like to thank my parents for their support, encouragement, and understanding through this study.

December 2019

Ohno Takuro